NATIONAL INSTITUTE FOR FUSION SCIENCE

Frontiers of Applied Pulse Power Technology

Edited by Weihua Jiang

(Received - Jan. 17, 2017)

NIFS-PROC-105

Aug. 28. 2017

Frontiers of Applied Pulse Power Technology

Edited by Weihua Jiang

January 7-8, 2014
National Institute for Fusion Science
Toki, Gifu, Japan

Abstract

The papers appeared in this volume of research report have been presented at the "Symposium on Frontiers of Applied Pulsed Power Technology" held by National Institute for Fusion Science. They report the present status and recent progress in experimental and theoretical studies on pulsed power technology and its applications.

Keywords: pulsed power, Particle beam, plasma, z-pinch, extreme ultraviolet, x-ray, high power microwave, material processing, pulsed discharge, high voltage, plasma focus.

PREFACE

The collaborative research symposium on "Frontiers of Applied Pulsed Power Technology" was held at National Institute for Fusion Science (NIFS), Toki, on Jan. 7-8, 2014. This symposium was attended by 47 researchers and students from universities, institute and industrial companies. At the symposium, 25 research papers were presented each of them was followed by fruitful discussions. This symposium has provided an excellent environment for information exchange between the researchers and has promoted collaborations between NIFS and universities.

During the symposium, LHD site tour was given by NIFS staffs especially for this symposium. The attendees have obtai ned an excepti onal opportunity to enjoy a close look at the LHD experimental facilities and listen to the in-depth explanations by the NIFS researchers.

I would like to express my sincere thanks to all of the symposium attendees, all of the paper authors, and the staffs of National Institute for Fusion Science.

Weihua Jiang
Extreme Energy-Density Research
Institute Nagaoka University of Technology

NIFS 2013 Coordinated Research (Symposium)
Project Title: Frontiers of Applied Pulsed Power Technology
Project ID: NIFSI3KKGHO18
NIFS Contact Person: Dr. Tetsuo Ozaki

List of participants

K. Adachi (Tokyo Institute of Technology)
H. Akiyama (Kumamoto University)
R. Ando (Kanazawa University)
T. Ando (Nihon University)
T. Furusato (Kumamoto University)
J. Hasegawa (Tokyo Institute of Technology)
R. Hayashi (Nagaoka University of Technology)
K. Horioka (Tokyo Institute of Technology)
E. Hotta (Tokyo Institute of Technology)
G. Imada (Niigata Institute of Technology)
H. Ito (University of Toyama)
S. Izumi (Nagaoka University of Technology)
W. Jiang (Nagaoka University of Technology)
T. Kakuta (Iwate University)
K. Kamada (Kanazawa University)
S. Kanamaru (Tokyo Institute of Technology)
A. Kano (Tokyo Institute of Technology)
K. Kato (Tokyo Institute of Technology)
K. Kawaguchi (Tokyo Institute of Technology)
T. Kawamura (Tokyo Institute of Technology)
T. Kikuchi (Nagaoka University of Technology)
T. Konishi (Iwate University)
Y. Machida (Nagaoka University of Technology)
R. Matsuda (Nagaoka University of Technology)
K. Mitsutake (Kumamoto University)
K. Miyata (University of Toyama)
T. Miyazaki (Nihon University)
R. Myodo (Niigata Institute of Technology)
T. Ogawa (Kanazawa University)
K. Ogura (Niigata University)
R. Ohya (Gunma University)
K. Okashima (University of Toyama)
T. Ozaki (NIFS)
Y. Park (Kanazawa University)
Y. Sakai (Tokyo Institute of Technology)
Y. Soga (Kanazawa University)

T. Sugai (Nagaoka University of Technology)

M. Sugimoto (University of Toyama)

K. Tahara (Niigata Institute of Technology)

K. Takaki (Iwate University)

K. Takasugi (Nihon University)

T. Tazima (NIFS)

A. Tezuka (Tokyo Institute of Technology)

A. Tokuchi (PPJ)

T. Uesaka (Kanazawa University)

N. Wantapon (Tokyo Institute of Technology)

K. Yonezawa (Tokyo Institute of Technology)

CONTENTS

Propagation mode and pressure measurement of underwater shock wave by large current short-pulse discharge

K. Miyata, and H. Ito

Dep. of Electrical and Electronic Engineering, University of Toyama,
3190 Gofuku, Toyama 930-8555, Japan

ABSTRACT

For application related to high energy density physics and various industrial fields, generation of the underwater shock wave with ultrahigh pressure and good controllability is required. Underwater shock waves were generated by using a high current short pulse discharge in a rod-rod electrode geometry produced by the pulsed power technology, which consists of a Marx generator and a pulse forming line. This paper reports the pressure measurement and observation of propagation of the underwater shock wave in distilled water. The temporal pressure waveforms of these underwater shock waves were measured by a PolyVinylidene DiFluoride (PVDF) pressure transducer. Underwater shock wave propagation in the given moment was observed by using laser shadowgraphic method with 2nd harmonic of Nd:YAG laser as a probe beam. When the output voltage of Marx generator was 150 kV and the discharge gap distance was 10 mm, the underwater shock wave with peak pressure of ~310 MPa and average propagation velocity of 1750 m/s was observed at 30 mm downstream from the electrode axis. In addition, pressures measured by the PVDF transducer were compared with analysis of the laser shadowgraphic results.

Keywords

Underwater shock wave, ultrahigh pressure, pulse power technology

1. Introduction

The subject of the generation of strong shock waves has already been of continuous interest for more than 100 years due to its important potential applications in basic and applied research related to equations of state, plasma and space physics. In a laboratory, there are several methods of shock wave generation, for instance, chemical explosions [1,2], laser irradiation of a target [3], and the Z-pinch approach [4]. One of the most widespread methods of a high-pressure shock wave generation is based on its generation by an electrical discharge in water which occurs between two electrodes. In the first phase, an application of a high-voltage pulse leads to an electrical breakdown between a pair of electrodes and a development of a growing streamer which subsequently connects both electrodes. In the second phase, further energy deposition into the formed spark leads to its explosive expansion in the radial direction and the generation of the shock wave in the surrounding liquid. Over the last two decades, applications of underwater shock waves have been extended to various practical applications, such as medicine, biological sciences, industrial, medical and environmental fields, because of the small compressibility of water and the relatively slight decay of a shock wave during its propagation.

A high shock wave pressure was realized due to an underwater electrical explosion of a conducting wire and/or quick release of high current at the high voltage electric power in water [5,6]. For example, Fedotov-Gefen *et al*. reported an extremely high pressure of 400 GPa by converging shock waves produced by an array of exploded wires [7]. However, this method of shock wave generation by an exploding wire method has the disadvantage that a

new wire need to be placed in the experimental setup after each shot. Therefore, this method is not suitable for various practical applications.

The control of strength and the pulse duration of the underwater shock wave are the most important factor for practical applications. In order to generate the underwater shock wave with high pressure and good controllability, we have developed the underwater shock wave system utilizing the pulse power machine which consists of a Marx generator and a pulse forming line. In this paper, we present the pressure measurement and experimental observation of propagation of the underwater shock wave in distilled water measured by a polyvinyliden-difluoride (PVD) pressure transducer and laser shadowgraphic method. In addition, underwater shock wave pressures measured by the PVDF pressure transducer were compared with analysis of the laser shadowgraphic results and we evaluated the dependence of the applied voltage amplitude on characteristics of underwater shock waves.

2. Experimental Setup

Figure 1 shows a schematic configuration of experimental system for studies on the underwater shock wave. The system consists of a Marx generator with the stored energy of 1.65 kJ, a pulse forming line (PFL) and a stainless-steel vessel with a pair of discharge electrode for the shock wave. The Marx generator is comprised of six-stage incorporating capacitors (C=220 nF) charged up to 50 kV, charging resistors (R=20 kΩ) and SF_6-filled field-distortion gap switches. The PFL consists of a pair of coaxial cylinders, i.e., an inner electrode of 114 mm length by 1250 mm outer diameter and an outer electrode of 210 mm inner diameter. The designed parameters of the PFL are capacitance per unit length of 7 nF, inductance per unit length of 121 nH, characteristic impedance of 4.2 Ω, and electrical length of 45 ns. The PFL is filled with the deionized water as a dielectric and charged positively by the low inductance Marx generator with maximum output voltage of 300 kV.

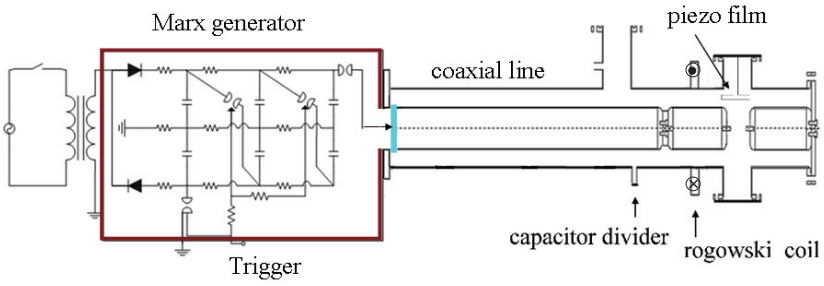

Fig.1 Experimental Setup

Underwater shock waves were generated by pulsed electrical discharge in distilled water (conductivity 1.5 μS/cm). Figure 2 shows a photo of the discharge electrode geometry for the underwater shock wave. The rod-rod electrode geometry was used as the discharge electrode in this experiment. The diameter of both stainless steel rod electrodes is 2 mm. The gap length between the rod electrodes was changed from 10 to 14 mm.

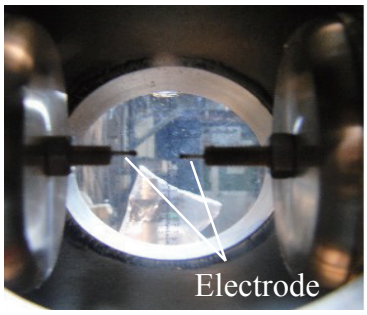

Fig.2 Photo of discharge electrode geometry for underwater shock wave

The voltage (V_{PFL}) applied to the electrode and the discharge current (I_d) through the electrodes were measured by the capacitive voltage divider and Rogowski coil, respectively. The values of applied voltage and discharge current were calculated by the ratio factor of the voltage divider (43000) and the coefficient of the Rogowski coil (87.7 kA/V), respectively. In addition, the polyvinyliden-difluoride (PVDF) pressure transducer with the coefficient of 90.2 MPa/V was used for measurement of the pressure of the underwater shock wave. The temporal signals from the

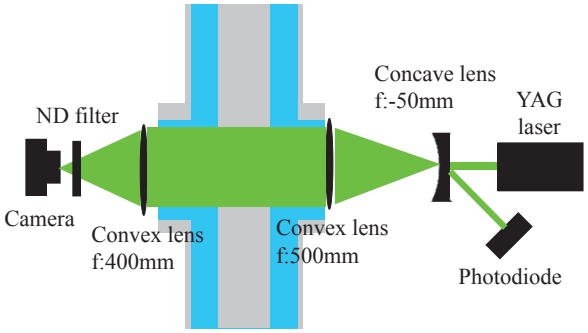

Fig. 3 Schematic diagram of the experimental setup of laser shadowgraph imaging.

measurement devices were recorded by an oscilloscope (TDS2024B, Tektronix).

The laser shadowgraphic method was used for experimental observations of propagation of the underwater shock wave. Figure 3 shows the schematic diagram of the experimental setup of laser shadowgraph imaging. The 2nd harmonic (wavelength 532 nm) of a Qswitched Nd:YAG laser with 5 ns pulse duration was used as the probe beam for shadowgraphs. This probe beam is expanded by two concave lenses with the focal length of -50 mm and 500 mm and illuminated the underwater shock wave. The illumination beams that pass through the underwater shock wave are collected onto a digital camera by the concave lens with the focal length of 400 mm. Several neutral density filters are located in front of the digital camera to block radiation by the discharge and to protect the camera.

The temporal variation of the shadowgraph image was obtained by changing the delay time between the trigger to Marx generator and the irradiation of the YAG laser pulse. The time delay between Marx generator and the YAG laser pulse was controlled by the delay generator. The actual time delay was measured by the time difference between the capacitive voltage divider and a photodiode located in an optical path. The laser shadowgraphic experiment was performed in a dark room. The camera shutter time was set to 1 second and the shutter is triggered manually just before firing the Marx generator and the probe laser.

3. Experimental Results

Figure 4(a) shows typical waveforms of applied voltage (V_{PFL}) and discharge current (I_d), where the Marx generator was operated at 150 kV and the discharge gap distance was d=10 mm. As seen in the Fig.4(a), the applied voltage reaches the peak value of 200 kV at 220 ns and after the peak drops suddenly. On the other hand, the discharge current rises sharply with a sudden drop of the applied voltage, which suggests a discharge (breakdown) in water. The discharge current reaches the peak value of 27 kA. Figure 4(b) shows a typical pressure waveform of the underwater shock wave measured by the PVDF pressure transducer placed at r=30 mm from the central axis of the discharge electrodes. Pressure measurements using the PVDF pressure transducer revealed that the underwater shock wave had a peak pressure of ~320 MPa with a half-width of ~ 2.5 μs. As shown in Fig.4(b), it takes about 18.4 μs for the underwater shock wave to reach the PVDF pressure transducer. Considering the time of flight delay, the average velocity of the shock wave is estimated to be 1630 m/s, which is faster than the acoustic velocity in

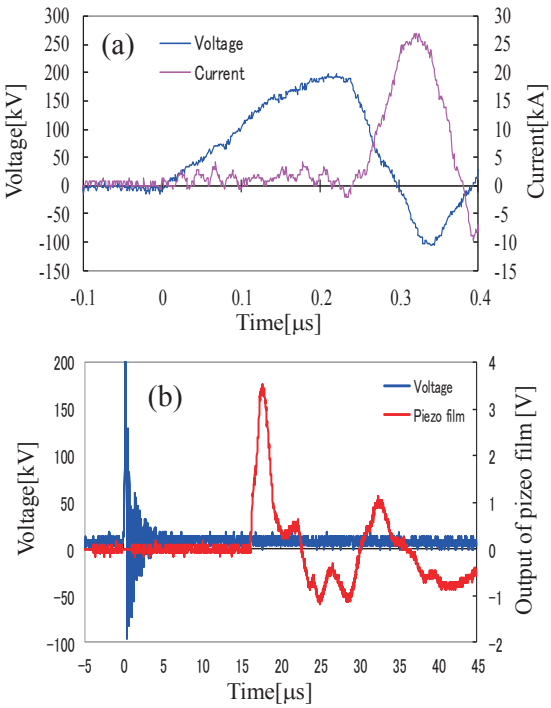

Fig. 4 Typical waveforms of applied voltage and discharge current (a) and pressure of underwater shock wave (b).

water (1500 m/s).

Figure 5 shows the dependence of the average velocity of underwater shock waves measured at each position from the electrode axis on the output voltage of Marx generator, where the output of Marx generator was set to be 150, 180 and 210 kV. The gap length between electrodes is adjusted so that the discharge can be initiated almost at the same time for each condition, i.e., the gap length was set to be 10, 12 and 14 mm, respectively. Data from up to 5 shots are taken to average shot-to-shot variations and each data point in Fig. 5 is an average of 5 shots. As seen in Fig. 5, when the output voltage of Marx generator is 210 kV, the average velocity of 1830 m/s was observed at 30 mm and the velocity decreases as the shock wave propagates away from the electrode axis. However, the average velocity measured at all positions is fast enough compared with the acoustic velocity in water. In case of other output voltages, the average velocity has the same tendency. These experimental results show that the underwater shock wave is generated by the pulsed electrical discharge. The average velocity tends to become faster with the increase of the output voltage, i.e., the deposited energy increases.

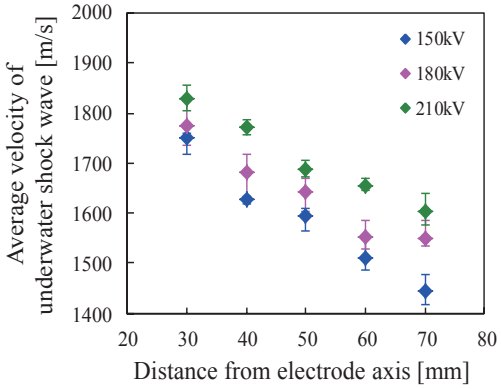

Fig.5 Dependence of average velocity of underwater shock wave measured on output voltage of Marx generator.

Figure 6 shows the pressure of the underwater shock wave measured at each position from the electrode axis by the PVDF pressure transducer as a function of the output voltage of Marx generator. The experimental parameters are the same as those set in Fig.5. The underwater shock wave with the maximum pressure of ~520 MPa is observed at 30 mm. The pressure decreases as the shock wave propagates away from the electrode axis and becomes higher with the increase of the output voltage. It was found from Fig. 6(b) that the pressure of the shock wave varies as 1/r at the measurement point (r) of 30~50 mm and as $1/r^2$ at r>50 mm. This result shows that the underwater shock wave propagates as a cylindrical wave mode in the vicinity of the electrode axis, but the propagation mode of the shock wave changes from a cylindrical wave to a spherical wave

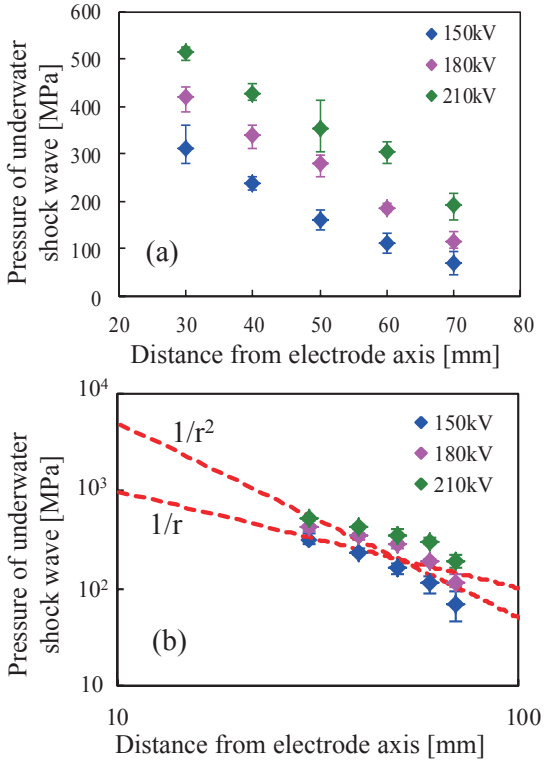

Fig.6 (a) Pressure of underwater shock wave as a function of output voltage of Marx generator and (b) log-log graph.

as it propagates away.

In order to evaluate the propagation of underwater shock wave in the vicinity of the electrode axis precisely, the laser shadowgraph was performed. Figure 7 shows the shadowgraphic images of underwater shock wave in the given moment, where the output voltage of Marx generator and the

discharge gap length were set to be 150 kV and 10 m, respectively. As seen in Fig.7, the underwater shock wave evolves as the cylindrical wave in the vicinity of the electrode axis. The wave front of the shock wave arrives at 15 mm in 9.8 μs after firing Marx generator. The velocity of the shock wave at each time can be estimated from the shadowgraph images. Figure 8 shows the velocity of underwater shock wave estimated from the shadowgraph images at each position. The underwater shock wave has the velocity of 1900 m/s at 5 mm from the axis. It is turned out from Fig.8 that the velocity is faster than the acoustic velocity in water and decreases as the shock wave evolves.

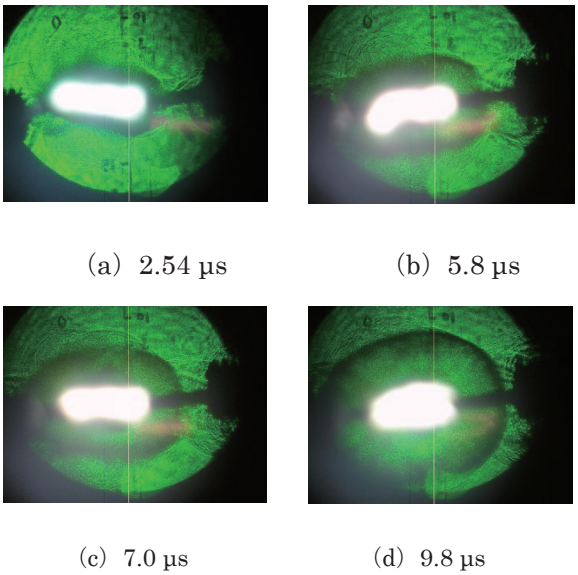

(a) 2.54 μs (b) 5.8 μs

(c) 7.0 μs (d) 9.8 μs

Fig.7 Shadowgraph images of underwater shock wave measured in each time.

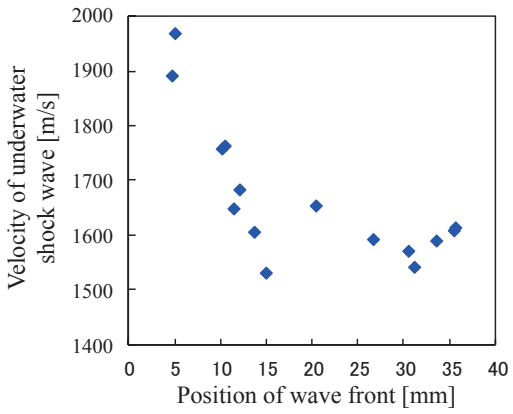

Fig.8 Underwater shock wave velocity calculated from shadowgraph images at each position.

Next, the underwater shock wave pressure was evaluated by using the following equation [8]

$$P = \rho_0 U_S (U_S - U) / S ,$$

where ρ_0, U_s and U are density the mass density of water (1000 kg/m^3), the acoustic velocity in water (1500 m/s) and the shock wave velocity, respectively and S=1.79. Figure 9 shows the pressure of underwater shock wave estimated from the above mentioned images at each position. As seen in Fig. 9, the underwater shock wave has the pressure of 500 MPa at 5 mm from the axis. The pressure of underwater shock wave decreases as the shock wave evolves. Compared with the results measured by PVDF pressure transducer, both results are in almost agreement.

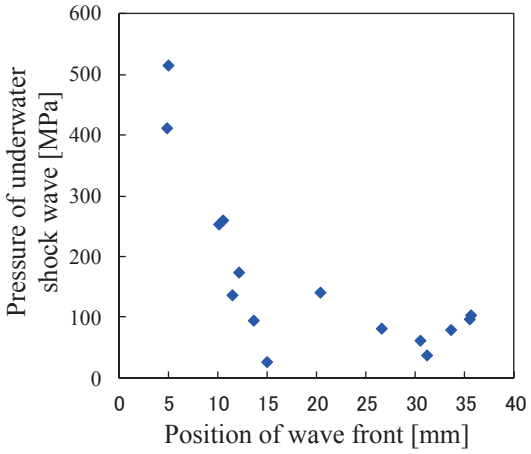

Fig.9 Underwater shock wave pressure at each position.

4. Conclusions

In order to generate the underwater shock wave with high pressure and good controllability, we investigated the characteristic of the underwater shock wave generated by means of the pulsed discharge in water by the pulse power machine which consists of the Marx generator and the pulse forming line. When the Marx generator was operated at 210 kV and the discharge gap length was set to be 14 mm, the underwater shock with peak pressure of about 520 MPa, average velocity of about 1830 m/s and half-width of 2.5 μs was measured by the PVDF pressure transducer placed at r=30 mm downstream

from the electrode axis. We found from the propagation characteristic that the propagation mode of underwater shock wave changes from the cylindrical wave to the spherical one.

References

[1] R.F. Flagg, I.I. Glass, "Explosive-driven, spherical implosion waves", Phys. Fluids **11**, pp.2282–2284 (1968).

[2] K. Terao, "Nuclear fusion reactor ignited by imploding detonation waves", *Proc. Int. 35th Intersociety Energy Conversion Engineering Conference and Exhibit (IECEC),* vol.2, pp. 915–924, Las Vegas, NV, USA (2000).

[3] G.H. Miller, E.I. Moses, C.R. Wuest, "The National ignition facility: enabling fusion ignition for the 21st century", Nucl. Fusion **44**, pp.S228–S238 (2004).

[4] R.J. Leeper et al., "Z pinch driven inertial confinement fusion target physics research at Sandia National Laboratories", Nucl. Fusion **39**, pp.1283–1294 (1999).

[5] E.A. Martin, "Experimental investigation of a high-energy density, high-pressure arc plasma", J. Appl. Phys. **31**, pp.255–267 (1960).

[6] T. Ya, *et al*., "Underwater electrical wire explosion," Plasma Sources Sci. Technol. 19, p.034020, (2010).

[7] A. Fedotov-Gefen, S. Efimov, L. Giburd, G. Bazalitsky, V. T. Gurovich, T. Ya, and E. Krasik, "Generation of a 400 GPa pressure in water using converging strong shock waves," Phys. Plasmas **18**, pp. 062701-1–062701-8 (2011).

[8] S.P. Marsh, "LASL Shock Hugoniot Data", University of California Press (1980).

Study on Shock Structure using Electro-magnetically Accelerated Counter-Streaming High-Speed Plasma

Koichiro Adachi, Tohru Kawamura, Jun Hasegawa, Mitsuo Nakajima, and Kazuhiko Horioka

Department of Energy Sciences, Interdisciplinary Graduate School of Science and Engineering, Tokyo Institute of Technology, Yokohama Japan 226-8502

ABSTRACT

We proposed a new scheme of plasma interaction experiments using a configuration of capillary pinch device, in which a pair of tapered capillaries produces a high-speed counter-streaming plasma flow. A controllable, high-speed Ar plasma with a drift velocity of ~20 km/s, an ion density 10^{13} cm^{-3}, an electron temperature ~1 eV, and a pulse length of more than microsecond was obtained sing the pinching plasma in the tapered capillary. Plasma interaction experiments were carried out at high-Mach number (M ~ 10) with counter-streaming configuration.

Keywords

Plasma shock wave, Pinch discharge, Pulse power, Collision-less shock, High-speed flow

1. Introduction

Phenomena induced by interaction of high-speed plasma flows are ubiquitous in space. High-speed plasma flows are involved in the escape of planet atmosphere [1], the formation of bow shocks in front of magnetosphere [2], particle acceleration in shock waves [3], and magnetic reconnections [4]. In particular, high energy particles accelerated in shock waves formed in supernova remnants are considered to be main sources of cosmic rays [5]. In the plasma shock waves, the kinetic energy of the plasma flow dissipates through generation of electric field and/or compression of magnetic field, even in collisionless conditions. The dissipation process in the collisionless plasma is considered to be depending strongly on the plasma parameters, which makes it difficult to investigate the process only by observations using telescopes and satellites. Therefore parametric study is needed to well understand the dissipation process of collisionless shocks.

As an approach to study the mechanism of collision-less shock formation, laboratory astrophysics has been attracting great attention since 1960s. In the past studies, several types of plasma sources were used for laboratory astrophysics experiments. They are laser ablation plasma sources [6], coaxial plasma guns [7], z-pinch de-vices [8], plasma focus devices [9, 10], and wire array discharge devices [11]. Recently, in the plasma interaction experiments with a counter-streaming configuration using high-intensity lasers [12] or plasma gun [13] and related PIC simulations [14, 15], have arisen much interest in the field of laboratory astrophysics. Interaction experiments using the counter-streaming configuration are useful for systematic study on collisionless shock waves over a wide range of parameters of plasma flows. However, these plasma sources are not so suitable to the parametric study because of their large stored energy and low capability of repetitive operation.

We proposed a new type of plasma source using tapered z-pinch discharge in a thin tapered capillary to investigate the complicated dissipation processes arising in interacting high-speed plasma flows [16]. The taper-pinched plasma (TPP) was radially compressed and axially accelerated by a sequentially pinching current sheet. A high-speed plasma with Mach number of 10 was successfully obtained using the thin tapered capillary filled with argon gas [17].

In the counter-streaming experiments using TPPs, the plasma velocity and the ion density in the interaction region are expected to be independently

controllable with high reproducibility. Advantages of the interaction experiment based on counter-streaming TPPs are summarized as follows:

- Repetitive, controllable, and well-defined plasma flows;
- Controllability of plasma parameters and magnetization level,
- Compact and flexible.

We evaluated the strength of interaction by comparing the ion-current and the optical signals from interacting high-speed plasmas with and without interaction.

The purpose of this study is to construct a table-top experimental apparatus based on the counter-streaming TPPs and reveal the potential as a device for investigating the formation process of plasma shock waves.

2. Scaling parameters

In general, adjustment of relevant scaling parameters is essential to reproduce a huge astrophysical phenomenon in a laboratory-scale device. Several scaling parameters must be considered at the same time to deal with complex phenomena [18]. Since scaling parameters are sensitive to plasma parameters, a controllable and well-defined plasma source is needed to perform the parametric study for the astrophysical phenomena.

Mach number is generally the most important parameter to characterize shock waves accompanying with high-speed plasma flows. In the present study, we focus on ion acoustic Mach number and mean free path for ion- ion collision as the scaling parameters.

The following ion acoustic Mach number M_i characterizes shock formation in unmagnetized plasma:

$$_i = \frac{U}{\sqrt{k_B T_e / m_i}} \quad (1)$$

where U is the plasma flow velocity, k_B is the Boltzmann constant, T_e is the electron temperature, and m_i is ion mass. Electrostatic shock waves in unmagnetized plasma are considered to be formed in a limited regime of M_i [19]. Shock waves in the astrophysical objects such as high-speed plasma flows interacting with planet magneto-sphere and supernova remnants, typically have the ion acoustic Mach numbers of the order of 10.

On the other hand, the mean free path for ion-ion collision λ_{ii} is given by:

$$\lambda_{ii} = \frac{2\pi\epsilon_0^2 m_i^2 v_i^4}{Z^4 e^4 n_i \ln\Lambda} \quad (2)$$

where ϵ_0 is the permittivity in vacuum, e is the elementary charge, Z is ionization degree, and $\ln\Lambda$ is the Coulomb logarithm. v_i and n_i are ion velocity and density respectively.

To achieve a collisionless condition, the plasma must satisfy the following requirement:

$$l \ll \lambda_{ii} \quad (3)$$

Here, l is the characteristic length of the plasma. The velocity, the density, and the temperature of high-Mach number and low-density plasma should be controlled independently to perform the parametric study.

3. Tapered pinch discharge device for laboratory astrophysical experiment

Figure 1 shows a schematic of a z-pinch discharge device using a tapered capillary. The capillary had a tapered wall with 10 mm in length. In the figure, the transmission lines were made of copper sheet that reduced the stray inductance. The main discharge circuit was axisymmetrically arranged as shown in Fig. 1. To reduce the circuit inductance, low inductance ceramic capacitors with 55 nF in total were installed for energy strage so as to surround a gap switch and the tapered capillary. They were charged typically to 10 kV. Then the stored energy in the capacitors was ~ 2.8 J. This circuit typically drives a peak current of ~10 kA with a period of 400

ns.

Operating parameters of our device are compared with those of plasma devices used in previous works in Fig. 2. As shown in the figure, our device can produce a high- speed plasma flow having equivalent Mach number even with a stored energy several orders of magnitude smaller than those for the conventional devices.

A differential pumping system and a dual-stage pre-ionization circuit were adopted to improve the reproducibility of the tapered z-pinch discharge. Figure 3 shows a schematic illustration of a stationary gas supply system and discharge circuits. The working gas was continuously supplied to the tapered capillary through an aperture (1 mm in diameter) on the cathode electrode and pumped by a turbo molecular pump through an aperture on the anode as shown in Fig. 3. The finite gas conductance of the anode aperture supported the pressure difference between the outside and the inside of the tapered capillary. Then the tapered capillary was filled quasi-statically by argon gas with a well-defined density. An ionization gauge and a Pirani gauge were used, respectively, to calibrate the pressures outside and inside the capillary in advance of the experiment. The pre-filled gas density in the tapered capillary was estimated from the calibration data.

To pre-ionize the argon gas weakly, a few kV of a DC voltage was applied between the electrodes before triggering the pulsed discharges. The DC pre-ionization was used to prevent the localization of the current path of pulsed pre-ionization discharge. A pulsed pre-ionizing current of the order of 10 A with a time duration of 400 μs was driven to form a uniform weakly-ionized plasma in the tapered

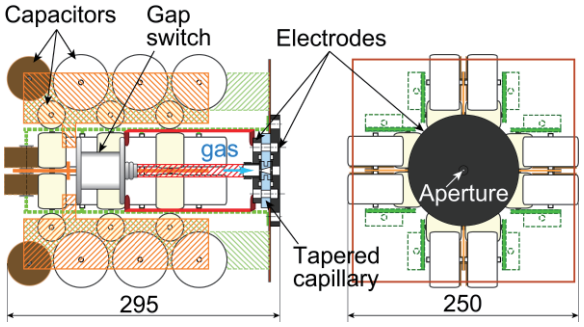

Fig. 1. A schematic of a z-pinch discharge device using a tapered capillary; the side view (left) and the front view (right).

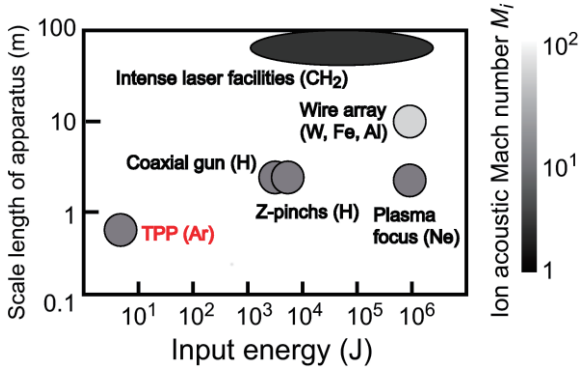

Fig. 2. Typical operating parameters of the taper pinched plasma and other plasma devices used in previous works. Ion species typically used in the devices are shown in parentheses [7–9, 11, 12].

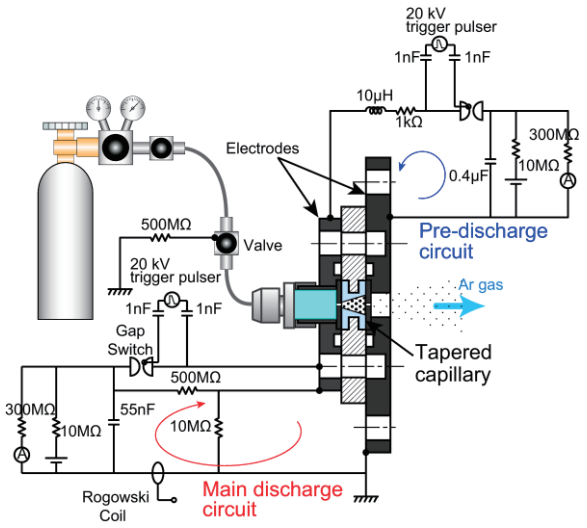

Fig. 3. A schematic of a differential pumping system and discharge circuits.

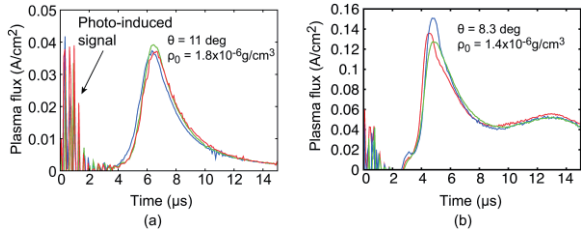

Fig. 4. Typical plasma flux waveforms at 200 mm from the capillary with a pre-filled gas density ρ of 1.4×10^{-6} g/cm^3 and a taper angle θ of 11° (a) and with a pre-filled gas density ρ_0 of 1.8×10^{-6}g/cm^3 and a taper angle θ of 8.3° (b), and a peak discharge current of 7 kA.

capillary ~ 40 μs before the main discharge started.

Figure 4(a) and (b) show typical plasma flux waveforms measured at 200 mm. The waveforms in the figure were overlaid for three operations. The jitter of the breakdown timing of TPPs was suppressed to the order of 100 ns. As shown in the figure, the shot-to-shot fluctuations of the peak arrival times and the amplitude of the peak plasma flux were within 20 %, which is enough to conduct interaction experiments. From these results, we confirmed that the tapered z-pinch discharge can be repetitively operated with high reproducibility thanks to the dual-stage pre-ionization scheme and the stationary supplied working gas by differential pumping.

The TPP was extracted into an interaction chamber through the small aperture on the anode electrode with drift velocity v_d. Because, the diffusion of magnetic field into the interaction chamber is expected to be prevented by the anode aperture, the TPP device can form an unmagnetized plasma flow more easily than conventional z-pinches, θ-pinches, and coaxial plasma guns. The fact may be supported by the following result in which the plasma flux waveform was compared with drift-Maxwellian distribution [20]. We regard that a point-like pinched plasma is produced in a tapered capillary expands freely into an interaction chamber.

As shown in Figs. 4 (a) and (b), the spatio-temporal scale of freely expanding plasma is centimeter-microsecond in the interaction chamber. It is advantageous for the counter-streaming plasma experiment because we can apply well-established plasma diagnostics. For example, the acoustic Mach number and the mean free path of high-speed plasma can be estimated from electron temperature, and average ion speed and density that are, respectively, measured with a Langmuir probe and a Faraday cup (FC).

The TPP parameters can be controlled independently by the discharge current, the pre-filled gas density, and the taper geometry [17]. The ion density can be also controlled by the flight distance of the plasma plume because the plasma is freely expanding. In the present study, we set the distance from the tapered capillary to the center of the interaction chamber to be 8 cm. The drift velocity of plasma and the ion density at the center of the chamber were estimated from the measurement by a FC. The FC made of brass with an effective diameter of 1 mm was placed coaxially with respect to the plasma drift direction to monitor the plasma flux. The bottom of the cup has a conical shape to collect the secondly electrons. The cup was biased to -100 V with respect to the plasma potential to suppress the co-moving electrons.

Results of the FC measurement are summarized in Fig. 5. The drift velocity of plasma v_d was estimated by the time of flight (TOF) of the plasma flux waveform, that is, by the arrival time and the distance of the FC from the capillary. Here, the arrival time of the plasma was defined by time interval between the first peak of discharge current and the peak of the plasma flux. For the drifting plasma, ion flux J_p is given by:

$$J_p = Zen_i v_i \tag{4}$$

By assuming $v_i = v_d$, ion density n_i at flux peak can be estimated. In Fig. 5, the solid line shows the plasma velocity and dotted line shows the ion density. As shown in the figure, the drift velocity of plasma and the ion density increase almost linearly with increasing the peak discharge current.

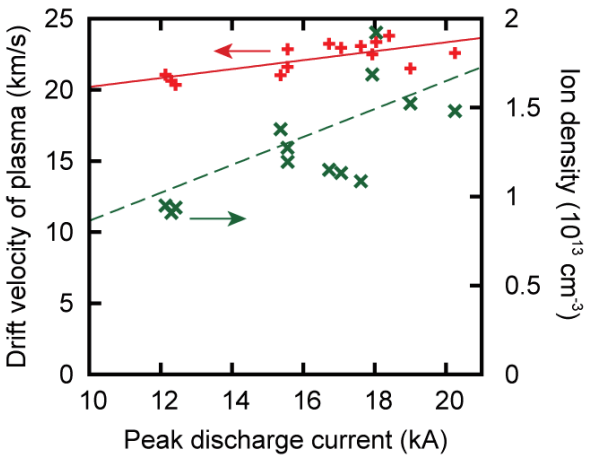

Fig. 5. Dependence of the drift velocity of plasma and the ion density on the peak discharge current.

4. Counter-streaming experiments with TPP devices

A. Experimental set-up

The experimental arrangement and the diagnostics for the interaction experiments are shown in Fig. 6. The images of the plasma were recorded by a fast framing camera (DRS HANLAND. Ltd., Imacon 468). The light emission from the plasma was measured by a time- resolved monochromater (Acton Research, Co., VM-504) with a phtomultiplier (Hamamatsu Photonics K.K., R2256HA), and a photodiode (Hamamatsu photonics K.K, Co., S1223-01). The spatial and temporal resolution of the photodiode observation were 3.6×3.6 mm^2 and 30 ns, respectively. Spatial and spectral resolutions of the monochromator were 1 mm and 6.3 nm, respectively.

The flux and the electron temperature of the plasma were measured using a Langmuir probe. The probe was made of cylindrical copper wire of 0.1 mm in diameter and 3 mm long and located at the center of the interaction chamber, 8 cm from the anode aperture. The probe was placed in the plasma flow so that its longitudinal direction became parallel to the flow direction. Thus, the spatial resolution of the probe measurement in the flow direction was 3 mm.

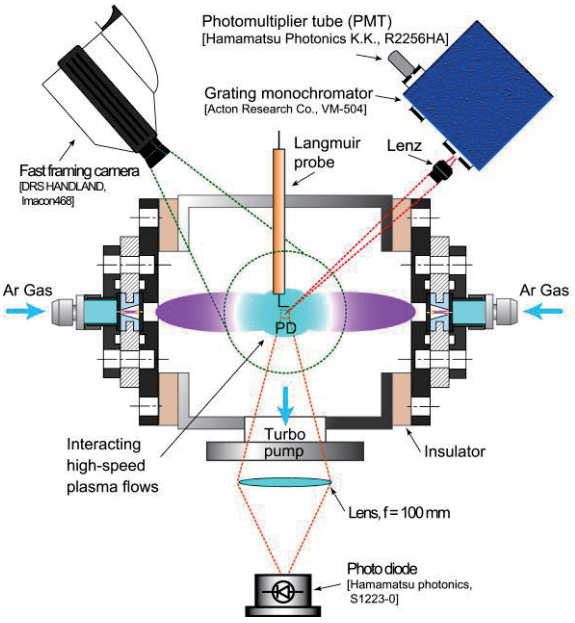

Fig. 6. A schematic of counter-streaming experiment with TPP devices.

B. Evaluation of plasma parameters

The measured V-I characteristics of the Langmuir probe are shown in Fig. 7. In the figure, solid and dashed lines show, respectively, the probe current in the single plasma flow and the counter-streaming plasma flows. We estimated the electron temperature T_e to be ~1 eV and ~2 eV for the single plasma flow and the counter-streaming plasma flows, respectively. We regarded that the electron temperature T_e is almost uniform in the plasma plume, in which electrons follow drifted Maxwellian distributed ions. The electron-ion mean free path is written by:

$$\lambda_{ei} = 4\pi\epsilon_0^2 m_e v_e^4 / (Z^2 e^2 n_i \ln\Lambda) \qquad (5)$$

where v_e is the thermal velocity of electrons.

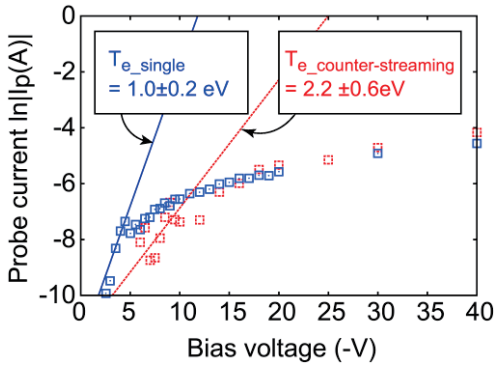

Fig. 7. Comparison of electron temperature estimated by probe signals in single plasma jet and counter-streaming flow for ρ_0 =0.8×10^{-6} g/cm^3 and the peak discharge current of 12.5 kA.

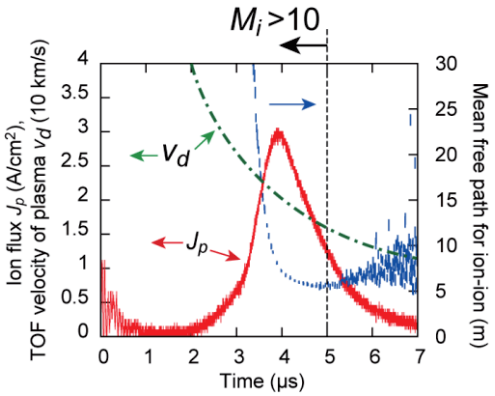

Fig. 8. Time evolution of the plasma flux (solid line), the TOF velocity (dash-dotted line), and the ion-ion mean free path (dotted line) for TPP with ρ_0 = 0.8×10^{-6} g/cm^3 and a peak discharge current of 12 kA.

The electron-ion mean free path was estimated to be ~1 cm in our experimental condition from Eq. (5). On the other hand, ion-ion mean free path λ_{ii} was estimated to be ~10 m by assuming the ion velocity v_i is equal to the drift velocity v_d = 24 km/s. In the typical experimental condition, λ_{ei} was comparable to and λ_{ii} was much longer than the size of the interaction chamber, indicating that the plasma flow was slightly collisional for electron-ion and collisionless for ions.

Figure 8 shows typical time-evolutions of plasma flux (solid line), TOF velocity (dash-dotted line), and ion-ion mean free path (dotted line) of the single plasma flow at the center of the chamber. These were estimated from the FC measurement. As shown in the figure, M_i of the TPP flow was in the order of 10 in a time duration of 2.5-5.5 μs in which the plasma velocity was 16-30 km/s. Ion acoustic Mach numbers typical in astrophysical phenomena were obtained by this device. The ion-ion mean free path was always much larger than the size of the interaction chamber. This result shows that the high-speed plasma flows can be merged in a condition in which ion- ion collisions were negligible.

5. Enhancement of light emission and deceleration of ion flow

Figure 9 shows typical framing images of the counter-streaming plasma, where PD in Fig. 9 denotes the observation area ($3.6\times3.6mm^2$) with the photodiode. Numbers 1, 2, and 3 in Fig. 9 and Fig. 10(a) show the gate timings of the fast framing camera. In this experiment, the exposure time was extended to 500 ns to adapt faint light emission from the plasma.

Plasma plumes moved from both sides of the image and merged at the center of vacuum chamber as shown in Fig. 9. The light emission from the plasmas decreased with time because the plasma expanded three-dimensionally in the interaction chamber.

Figures 10 compares two cases, with and without interaction between counter-streaming plasma flows. Note that in the case, without interaction, the waveforms were independently recorded by operating one of the TPP sources and summed later. Typical waveforms from the Langmuir probe are shown in Fig. 10 (a), (c), and (e). The photodiode signals are shown in Fig. 10 (b), (d), and (f). The dashed lines in the figures show the cases, with- out interaction and the solid lines show the cases, with interaction. The probe current in these figures denotes ion saturation current signals measured by the Langmuir probe at a bias voltage of -40V. The results given in Fig. 10 (a), (b); (c), (d); and (e), (f) were obtained at peak discharge currents of 10.5 kA, 12.5 kA, and 16.6 kA, respectively.

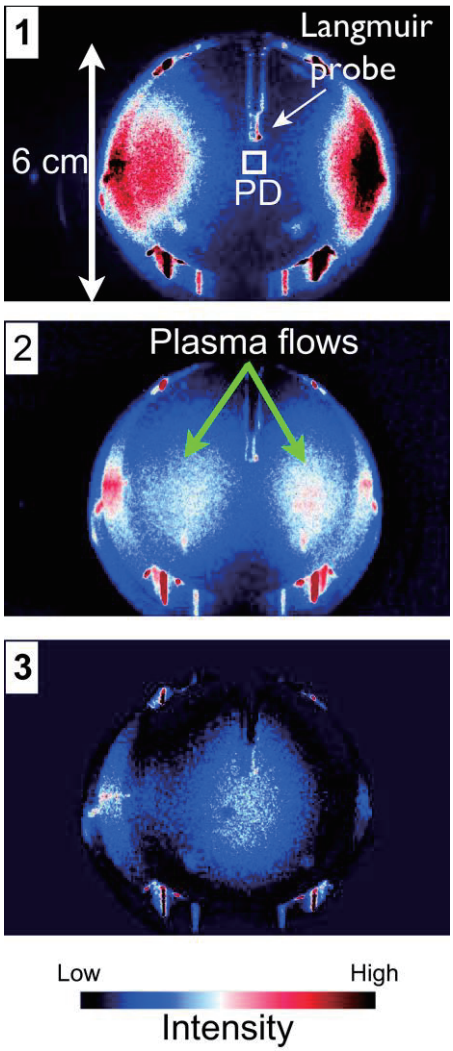

Fig. 9. Typical frame images of counter-streaming plasma. The images 1, 2, and 3 were taken 3μs, 3.5μs, and 4μs after the start of the pinch discharge, respectively.

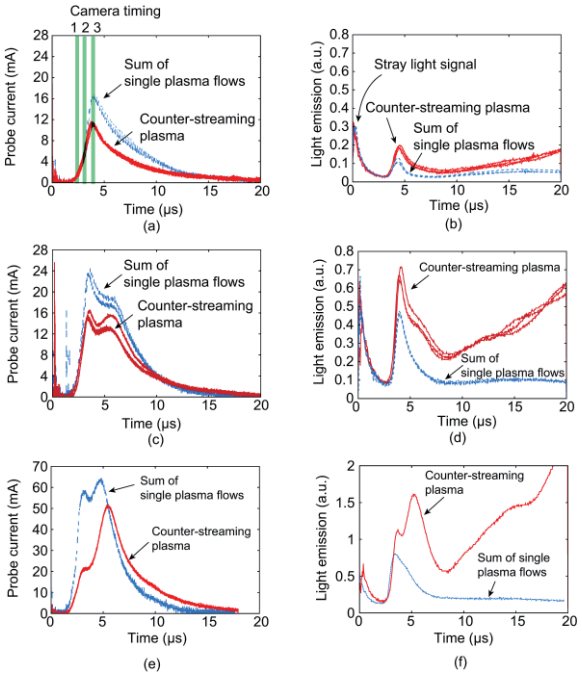

Fig. 10. Probe signals (a), (c), and (e), and light emissions (b), (d), and (f) from counter-streaming plasma with the pre-filled gas density ρ_0 of 0.8×10^{-6}g/cm^3 and peak discharge currents of 10.5 kA (a and b), 12.5 kA (c and d), and 16.6 kA (e and f), respectively.

Three signals were overlaid for the probe current and light emission signals in Figs. 10 (a), (b), (c), and (d). Rapidly fluctuating probe signals observed until 2 μs in Fig. 10(a), (c), and (e) are due to electro-magnetic noise from the pulsed discharges. In Fig. 10 (b), (d), and (f) we can see light signals even before the counter-streaming plasma arrived at the center of the chamber (< 2 μs). These signals were probably due to stray light from the pinching plasmas in the tapered capillaries.

The time when the probe signal reaches the maximum corresponds to the time when the counter-streaming plasma flows merged together at the center of the chamber as shown by the corresponding image in Fig. 9 (c). When we see Figs. 10 (b), (d), and (f), the light emissions from the interacting plasma are always higher than the sum of emissions from independently operated plasma flows. The enhancement of light emission from the interacting high-speed plasma flows indicates that the counter-streaming plasma flows affected each other.

In this experiment, the plasma moved with a mean kinetic energy of ~100 eV which is much larger than the ion temperature (~1 eV). In general, the probe current I_p observed in a drifting plasma can be written by:

$$J_p = eZn_iS_p\exp\left(-\frac{1}{2}\right)\sqrt{\frac{k_BT_e}{m_i}} + eZS_{p,eff}n_iv_d \qquad (6)$$

where $S_{p,eff}$ is the effective probe area normal to the drift velocity. The decrease of the probe current in the counter-streaming case indicates the deceleration of the ion flows.

Then, we performed a spectroscopic measurement to obtain information on atomic processes occurring in the interacting plasma flows. We selected a transition of argon ion $3p^4(^3P)4s$ - $3p^4(^3P)4p$ (487.99 nm). The existence of this transition in the light spectrum from the plasma means that electrons having kinetic energies higher than 19.7 eV, the excitation energy for the upper level of the transition, exist in the plasma. As shown in Fig. 11, the light emission due to this transition obviously increased for the counter-streaming plasmas compared with that for single plasma flows. This result strongly supports the acceleration of plasma electrons by the electrostatic potential formed in the interaction as mentioned above.

When we assume that electrons and ions collide frequently in the typical interaction time, the time evolution of the population of ions with energy levels relating to the light emission can be described by the Rate equation based on the Collisional-Radiative model. When the counter-streaming plasmas with the electron density and the population of ions at q, n, were merged in the center of the interaction chamber, the rate coefficient for excitation by electron impact C can be described in the interacting plasmas as follows:

$$\sum_{q<p} C_{q,p}n_e'n_q' = \sum_{q<p} C_{q,p}(2n_e)(2n_q) = 4\sum_{q<p} C_{q,p}n_en_q \qquad (7)$$

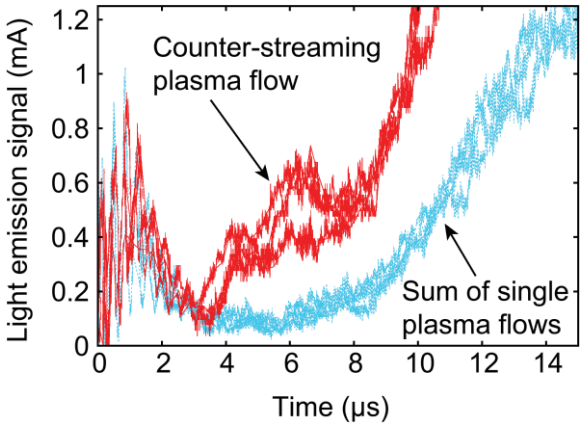

Fig. 11. Temporal line emission of ArII (488 nm) from counter-streaming flows and sum of independent plasma flows for ρ_0=0.8×10^{-6} g/cm^3 at peak discharge current of 12.5 kA.

where p and q are levels in an arbitrary ionization stage. n' and n' are, respectively, the electron density and the population of ions at q in the interacting plasmas. This means that the line emission from counter-streaming plasmas becomes four times larger than that from a single plasma flow if the single plasma flows are assumed to simply interpenetrate each other. However, the line emission shown in Fig. 11 revealed that the enhanced line emission became much larger than expected in the interpenetration case particularly after the plasma flux peak (> 4 μs). The enhancement of line emission from argon ions might prove the formation of electrostatic potential in the counter-streaming plasmas. All of the observations indicate the deceleration of ions in the interaction region of the collisionless plasma flows under high-Mach-number (M > 10).

V. CONCLUSIONS

We proposed a table-top pulsed power device for interaction experiments of high speed plasma flows. The device was composed of a pair of counter-facing tapered-capillaries and a compact pulsed power drivers with a 6-J energy strage level, which enabled us to make reproducible, repetitive, and well-defined interaction experiments. The plasmas were pinched and electro-magnetically accelerated in the thin tapered capillaries. After the acceleration, the pinched point-like plasmas drifted and expanded in a vacuum chamber, leading to the formation of collisionless counter-streaming plasma flows with drift-Maxwellian profiles.

The device also enables us to adopt conventional and well-developed plasma diagnostics thanks to moderate spatio-temporal scale of the plasma in the test section. Preliminary interaction experiments of counter-streaming high-Mach-number flows were carried out under the collisionless condition of ions with this device. All of the results indicated that high-speed argon flows may dissipate almost 20 % of their initial kinetic energy in the interacting region even without ion-ion collisions.

References

[1] E. Dubinin, M. Fraenz, A. Fedorov, R. Lundin, N. Ed- berg, F. Duru, and O. Vaisberg, *Space Sci. Rev*., **162**, 173 (2001).
[2] J.L. Phillips, S.J. Bame, W.C. Feldman, J.T. Gosling, C.M. Hammond, D.J. McComas, B.E. Goldstein, and M. Neugebauer, *Adv. Space. Res*., **16**, (9)85 (1995).
[3] R.D. Blandford and D. Eichler, *Phys. Rep*., **154**, 1 (1987).
[4] D. Biskamp, Phys. report, 237, 179 (1994).
[5] K. Koyama, R. Petre, E.V. Gotthelf, U. Hwang, M. Mat- suura, M. Ozaki, and S.S. Holt, *Nature*, **378**, 255 (1995).
[6] A.R. Bell, P. Choi, A.E. Dangor, O. Willi, D.A. Bassett, and C.J. Hooker, *Phys. Rev. A*, **38**, 1363 (1988).
[7] R. Rana, S.Minami, S.Takechi, A.I.Podgorny, and I.M.Podgorny, *Earth Planets Space*, **56**, 1005 (2004).
[8] J. W. M. Paul, L. S. Holmes, M. J. Parkinson, and J. Sheffield, *Nature*, **208**, 133 (1965).
[9] D.Mourenas, J.Vierne, F.Siemonet, V.I.Krauz, S.Nikulin, V.V.Mialton, and M. A. Karakin, *Phys. Plasmas*, **10**, 605 (2003).
[10] K. Kondo, M. Nakajima, T. Kawamura, and K. Horioka, *Rev. Sci. Instrum*., **77**, 036104 (2006).
[11] S.V.Lebedev, D.Ampleford, A.Ciardi, S.N.Bland, J.P.Chittenden, M.G. Haines, A.Frank, E.G.Blackman, and A. Cunningham, *Astrophys. J*., **616**, 988 (2004).
[12] J.S. Ross, S.H. Glenzer, P. Amendt, R. Berger, L. Di- vol, N.L. Kugland, O.L. Landen, C. Plechaty, B. Rem- ington, D. Ryutov, W. Rozmus, D.H. Froula, G. Fik- sel, C. Sorce, Y. Kuramitsu, T. Morita, Y. Sakawa, H. Takabe, R.P. Drake, M. Grosskopf, C. Kuranz, G. Gregori, J. Meineche, C.D. Murphy, M. Koenig, A. Pelka, A. Ravasio, T. Vinci, E. Liang, R.

Presura, A. Spitkovsky, F. Miniati, and H.-S. Park, *Phys. Plasmas*, **19**, 056501 (2012).
[13] S.C. Hsu, E.C. Merritt, T.J. Awe, S.J.E. Brockington amd J.S. Davis, C.S. Adams, A. Case, J.T. Cassibry, J.P Dunn, M.A. Gilmore, A.G. Lynn, S.J. Messer, and F.F. Witherspoon, *Phys. Plasmas*, **19**, 123514 (2012).
[14] C. Thoma, D.R. Welch, and S.C. Hsu, *Phys. Plasmas*, **20**, 082128 (2013).
[15] T.N. Kato and H. Takabe, *Phys. Plasmas*, **17**, 032114 (2010).
[16] K. Adachi, M. Nakajima, T. Kawamura, and K. Horioka, *Plasma and Fusion Research: Rapid Communications*, **6**, 1201019 (2011).
[17] K. Adachi, M. Nakajima, T. Kawamura, and K. Horioka, *IEEE Transaction on Plasma Science*, **40**, 3308 (2012).
[18] R.P. Drake, *Phys. Plasmas*, **7**, 4690 (2000).
[19] M.E. Dieckmann, H. Ahmed, G. Sarri, D. Doria, I. Kourakis, L. Romagnani, M. Pohl, and M. Borghesi, *Phys. Plasmas*, **20**, 0421111 (2013).
[20] K. Adachi, M Nakajima, T. Kawamura, and K. Horioka, *NIFS Proceeding*, NIFSNIFS-PROC-94, 114 (2013)

Development of a Single-Shot Charge State Analyzer for Laser Produced Plasmas

Satoru Kanamaru[a], Jun Hasegawa[a], Kazuhiko Horioka[a], Mitsuo Nakajima[a]

[a]Department of Energy Sciences, Interdisciplinary Graduate School of Science and Engineering, Tokyo Institute of Technology, Japan

ABSTRACT

This paper reports on the development of a single-shot charge state analyzer, which enables us to observe plasma ion flux waveforms for various charge states simultaneously by separating the ion flux for each charge state. The analyzer was carefully designed to suppress the space charge effect and eliminate electrons from the plasma with the help of numerical analyses such as a beam envelope calculation. From the beam spot observation using a MCP assembly, we confirmed that the plasma ion flux was separated into multi beams depending on the charge state of the ions.

Keywords

Heavy ion inertial fusion, Laser-produced plasma, Ion source, Charge state distribution

1. Introduction

The development of driver accelerators is the most important issue in the study of heavy ion fusion (HIF). In order to gain sufficient fusion output, HIF driver accelerators are required to supply high current heavy ion beams with 10 GeV and 100 kA in total and to irradiate them on a fuel target with a duration of typically 10 ns. Ion sources located in the uppermost stream of the HIF driver accelerators need to stably supply heavy ion beams with high current (~0.5 A) and low emittance (~1 mm-mrad) with a duration of about 20 μs when a driver design based on induction accelerators is adopted. A lot of studies on the ion source for the HIF driver accelerator have ever been conducted [1][2][3]. Kwan *et al*. proposed a merging multibeamlet scheme, which extracts a lot of small beamlets simultaneously and merges them at downstream [1]. They reviewed applicable plasma sources for this scheme. Compared with a conventional scheme, which extracts a large-aperture beam from a surface-ionization-type ion source, this scheme has some advantages; the device can be compact and variable plasma sources are applicable. Thus, the merging beamlet approach can be a promising candidate for the extractor of the HIF drivers.

Generally, an ion beam extracted from an ion source is governed by scaling laws, which are led from the space charge limit and the breakdown limit of extraction electrodes [2].

$$J_{CL} \propto d^{-5/4} \quad (1)$$

$$I_{CL} \propto d^{1/2} \quad (2)$$

J_{CL}, I_{CL}, and d are ion beam current density, ion beam current, and distance between extracting electrodes, respectively. From Eqs. (1) and (2), one can see that I_{CL} increases with d, but J_{CL} decreases with d. A conventional large-aperture beam extraction is based on Eq. (2). On the other side, a merging multibeamlet extraction is based on Eq. (1), in which a lot of small beamlets with high J_{CL} are extracted simultaneously and merged at downstream. To apply this scheme to the HIF ion source, the quantitative investigation of emittance enhancement at the merging section is needed.

Variable plasma sources are applicable to the merging multibeamlet extraction. Especially, since laser-produced plasma is characterized by high

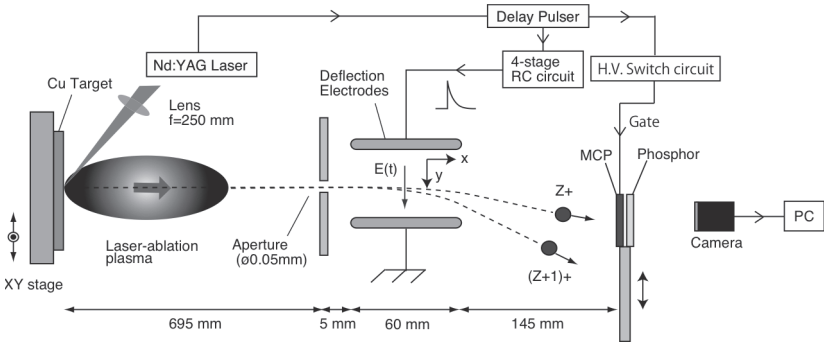

Fig. 1. A schematic diagram of the experimental equipment.

density and large drift velocity, it has the potential to supply a heavy ion beam with high current and low emittance. Barabash *et al*. [3] focused on these features of the laser-produced plasma. They produced low charge state ions by irradiating CO_2 laser onto a ^{207}Pb target and investigated the potential of the laser ion source as a HIF ion source. On the other hand, the laser-produced plasma has a difficulty in stable ion beam extraction due to the large fluctuation of ion flux and low purity of ion charge state. Thus, the feasibility of the laser ion source as a HIF ion source has not been clarified.

The goal of our study is to control the ion flux and the ion charge state of the laser-produced plasma by selecting the target material or applying external electromagnetic fields. In this paper, we report on the development of a single-shot charge state analyzer to observe the ion flux waveforms for various charge states simultaneously. The conventional electrostatic charge-state analyzers are not adaptable for low-reproducibility plasmas because these analyzers need repetitive measurements over several tens of laser shots to reconstruct one waveform. In contrast, the single-shot charge state analyzer can obtain the required information in one measurement. So this approach is suitable to the investigation of laser-produced plasma under variable conditions.

2. Experimental Setup

Figure 1 and Figure 2 show a schematic and a picture of the experimental equipment, respectively. The pressure in the vacuum chamber was kept at approximately 2×10^{-4} Pa by a turbo molecular pump.

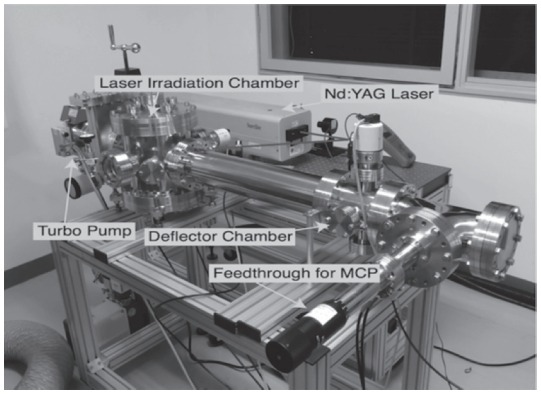

Fig. 2. Overall view of the experimental equipment.

A copper plate was used as a laser target. A plasma was produced by focusing fundamental wave of Nd:YAG laser (λ=1.06 μm) on the copper surface. The laser pulse energy was typically 380 mJ. The copper target was mounted on a two-axis motorized stage controlled remotely. The stage was moved in x-y directions parallel to the target surface plane each ~10 laser shots to ensure stable plasma generation. The produced plasma drifted with freely expanding and was investigated by the single-shot charge state analyzer located downstream.

The operating principle of the single shot charge state analyzer is as follows. The laser-produced plasma drifting in the chamber is collimated by a circular aperture (50 μm in diameter) located 695 mm downstream from the laser target. Ions in the plasma entering in the charge state analyzer is deflected by a temporally changing transverse electric field $E(t) \propto t^2$, where t denotes time. This electric field is induced by pulsed voltage applied to deflection electrodes that

are 60 mm wide and 50 mm long and located 5 mm downstream of the aperture. The laser pulse width is approximately 6 ns and it is negligibly shorter than the typical time of flight (>10 μs) of the plasma ions. Therefore we can consider that the plasma is produced at $t = 0$ instantaneously. Under this assumption, the velocity of ions entering the detector at each time is determined uniquely. Then, by temporally changing the deflection electric field in accordance with the ion velocity, ions trace fixed orbits that depend only on the charge state. Thus, ions with different charge states are separately recorded by ion detectors located 145 mm downstream from electrodes.

To analyze the charge state distribution based on the principle above, only ions must enter the analyzer, *i.e.* electrons must be eliminated from the plasma in advance. This is achieved with comparative ease by setting the aperture diameter to be less than Debye length. Its principle is as follows. A sheath is generated when a plasma plume approaches close to the aperture. Since the sheath electric field is bent by a fringe effect in the vicinity of the aperture, plasma electrons are easily accelerated toward the edge of the aperture due to their small mass and impact the aperture plate. On the other hand, plasma ions go straight and pass through the aperture due to their large momenta. As a result, electrons are mostly eliminated from the plasma and only ions enter the analyzer. The Debye length λ_D is described by:

$$\lambda_D = \sqrt{\frac{\varepsilon_0 k_B T_e}{ne^2}}, \tag{3}$$

where ε_0 is dielectric constant of vacuum, k_B is Boltzmann's constant, T_e is electron temperature, n is plasma density, and e is elementary charge. $k_B T_e$ is assumed to be 1 eV. By assuming that the plasma density is inversely proportional to the cube of drift distance, the relation between the distance from laser target and the Debye length is given as shown in Fig. 3.

According to Fig. 3, the Debye length becomes 50 μm at 0.4 m from the laser target. Thus, by locating the aperture with a diameter 50 μm more than 0.4 m downstream from target, the diameter of aperture becomes less than the Debye length and electrons are eliminated.

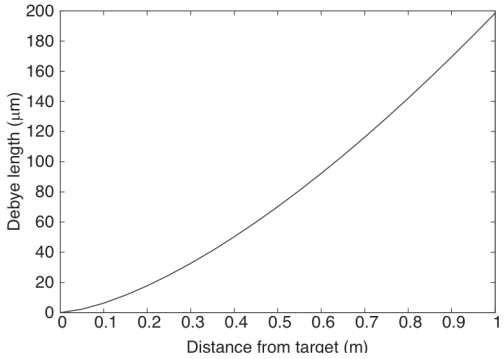

Fig. 3. Debye length in laser-produced plasma as a function of distance from laser target.

On the other hand, ions passing through the aperture repel one another because of their space charges, so the beam radius gradually increases. This effect needs to be suppressed because it directly influences the resolution of the analyzer. The space charge effect can be suppressed by decreasing the current density of ion flux, but ion flux measurement becomes difficult because of small current values. Regarding the location of the aperture as a parameter, the spread of the ion beam caused by the space charge effect is calculated from an envelope equation given below. In this calculation, the plasma ion current density is assumed to be inversely proportional to the cube of drift distance. The envelope equation used for a cylindrical ion beam is described by:

$$\frac{dR}{dz} = 2\sqrt{K}\sqrt{\ln\frac{R}{R_m}}, \tag{4}$$

$$K = \frac{eI_0}{2\pi\varepsilon_0 m_0(\beta\gamma c)^3}, \tag{5}$$

where R is the ion beam radius, z is the beam axis coordinate, R_m is the aperture radius, and I_0 is the ion current passing through the aperture. The ion beam radius 200 mm downstream from the aperture is plotted as a function of the location of the aperture in Fig. 4. The ion beam diameter must be a few millimeters from the requirement of the ion detector. From Fig. 3, one can see that the ion beam radius 200 mm downstream from the aperture becomes

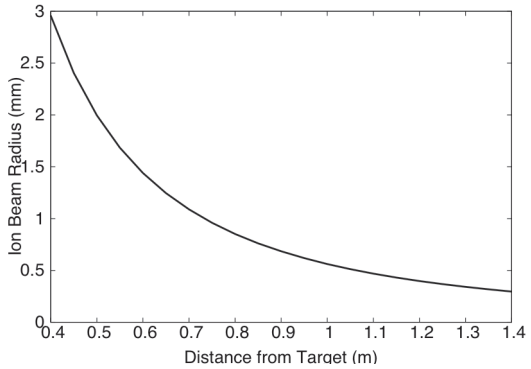

Fig. 4. Dependence of expected ion beam radius on distance from the laser target to the aperture.

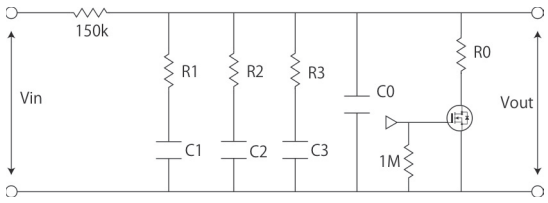

Fig. 5. A schematic of the 4-stage RC discharge circuit.

approximately 1 mm by locating the aperture at 0.7 m from laser target. Then, the aperture location was determined to be 695 mm from the laser target in our equipment.

The deflection electric field applied to the ions was given by a pair of plane parallel electrodes (width, length, and gap distance are 60 mm, 50 mm, and 20 mm, respectively). The field was induced by a voltage pulse $V(t) \propto t^2$, which was generated by a 4-stage RC discharge circuit shown in Fig. 5. The required values and the measured values of the circuit elements are summarized in Table 1. The output waveform from this circuit and the ideal waveform ($V(t) \propto t^2$) are compared in Fig. 6. A FET transistor (Toshiba 2SK2968) was used as a switch in the circuit, so the maximum charging voltage of the capacitors was 900 V. Figure 6 shows that there is a large discrepancy between the ideal and the experimental voltage waveforms before 5 μs. On the other hand, the both waveforms almost coincide from 5 μs to 11 μs. To use the ideal part of the waveform, the timing of voltage application was adjusted with respect to the laser irradiation by a delay and pulse

Table 1. Required and measured values of elements of the 4-stage RC circuit.

Resistor (Ω)	R0	R1	R2	R3
Required	300	1370	1810	4450
Measured	301	1368	1806	4500
Capacitor (pF)	C0	C1	C2	C3
Required	2522	298	666	1157
Measured	2530	330	650	1170

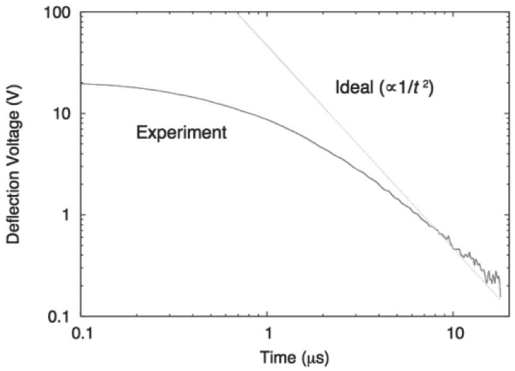

Fig. 6. An output voltage waveform of the 4-stage RC discharge circuit and an ideal deflection voltage waveform.

generator.

Faraday cups are considered to be suitable to ion detection because of the linearity of detection sensitivity. In the present study, to observe the behavior of the deflected ions, a MCP assembly with a high-speed phosphor screen was adopted. By applying a gate voltage from 1.2 kV to 1.6 kV with a pulse duration of approximately 15 μs, the position, the size, and the intensity of the deflected ion beams were observed.

The timing of the gate voltage was also adjusted with respect to the laser irradiation by the delay pulse. The light emission from the phosphor screen of the MCP was photographed by a digital camera with a 2-s exposure time and recorded by a PC.

3. Results and Discussion

3.1 Observation of ion beam expansion

The observed ion beam spot without deflection

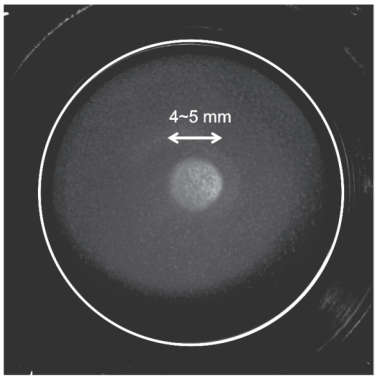

Fig. 7. The image of an ion beam spot without deflection electric field.

electric field is shown in Fig. 7. The MCP was located coaxially with respect to the entrance aperture of the analyzer. The effective area of the phosphor is indicated by a solid line in the figure and its diameter is 26 mm. The circular image on the phosphor center is the ion beam spot. From Fig. 7, we estimated that the beam diameter is approximately 5 mm.

The ion beam radius on the MCP surface is plotted in Fig. 8 (solid line), which was calculated by Eq. (4) based on actually observed ion beam current (dotted line). From the pulse width of the gate voltage applied on the MCP, the ion beam spot image observed in Fig. 7 corresponds to the integration of the beam spot from 0 μs to 8 μs in Fig. 8. As shown in Fig. 8, the maximum ion beam radius observed on MCP surface is approximately 5 mm. The observation result well agrees with the calculation result, which shows that the prediction of ion beam

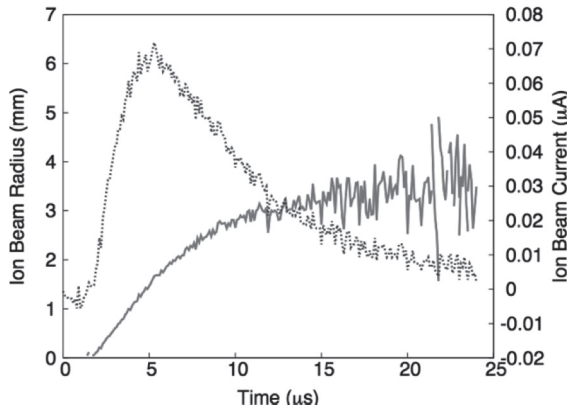

Fig. 8. Calculation results of ion beam radius on the MCP surface and ion beam current passing through the aperture.

spread caused by the space charge effect was almost correct. In addition, Eqs. (4) and (5) consider only ions (no electron), so we can guess that electrons were sufficiently eliminated at the entrance aperture of the analyzer.

3.2 Observation of deflected ion beam

The image of beam spots with charge separation is shown in Fig. 9. The deflection voltage attenuates with time from 400 V as shown in Fig. 6. The timings of the deflection voltage and gate voltage applications were set to be 0.5 μs and 7.0 μs after laser irradiation (plasma production), respectively. Since the pulse length of the MCP gate voltage is around 10 μs, the ions observed by the MCP have drift velocities between 1.3×10^5 m/s and 0.5×10^5 m/s. In addition, these ions enter the deflection electrode gap at approximately 5.0 μs to 14.0 μs after plasma production, so the observed ions experienced deflection electric field corresponding to t = 5.0 μs to 13.5 μs in Fig. 6. Furthermore, the center of MCP was shifted 15 mm toward the deflection direction. Six ion beam spots are seen in Fig. 9. We found that the ion flux was successfully separated for each charge state by the deflection electric field.

By assuming that copper ions from 1+ to 6+ were produced, ion orbits under an actual deflection electric field were calculated as shown in Fig. 10. The space charge effect was not considered in this calculation. Figure 10 shows that the separation of the ion orbits is not perfect and some of the beam spots overlap one another. This calculation almost

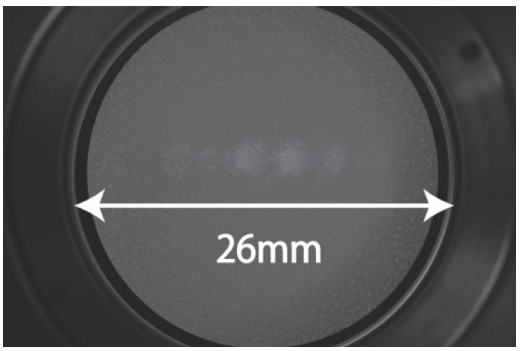

Fig. 9. Ion beam spot images observed on the phosphor screen.

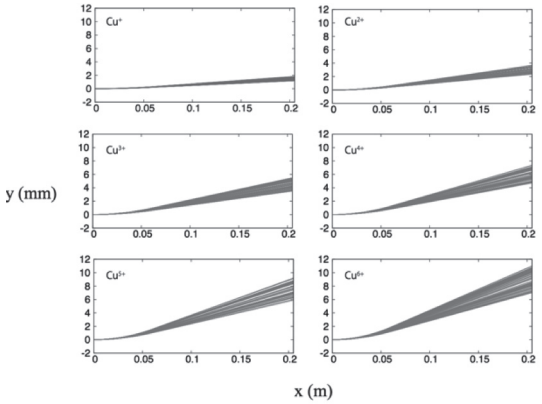

Fig. 10. Calculated ion orbits under an actual deflection electric field.

reproduces the observed result in Fig. 9, which shows that the analyzer worked almost as designed. On the other hand, it is very probable that ions were additionally deflected in the vicinity of the MCP since high voltage is applied to the MCP front surface in the present experimental setup. This may explain why the actual deflections were larger than predicted by the calculation.

To examine the performance of the charge-state analyzer, the unwanted beam deflection by the gate potential of the MCP front surface must be avoided. We are now developing a new gate circuit to solve this problem. Another issue is the improvement of the deflection waveform applied to the deflector. A more sophisticated driving circuit for the deflector will improve the resolution of the charge-state analyzer.

4. Conclusions

To investigate the influence of magnetic fields on the ion flux and charge state distribution of laser-produced plasmas, we developed a single-shot charge state analyzer and conducted preliminary experiments to check the analyzer performances. In these experiments, the elimination of the electrons is confirmed and the suppression of the ion beam spread is observed. We confirmed that the plasma ion flux was separated into several beams depending on the charge state of the ions by a deflection electric field that changes inverse-proportionally to the square of time. However, some problems remain to be solved; *e.g.* the influence of the MCP gate voltage on the ion orbit caused the insufficient separation of ion beams. To analyze charge state distribution with high precision, these problems need to be resolved. Furthermore, it will be necessary to select optimum ion detectors for the simultaneous measurement of the flux waveforms of different charge states. In the present setup, direct measurement of ion flux by Faraday cup may be difficult because the available ion beam current is very small. Instead of the Faraday cups, the use of electron multipliers such as channeltron is possible. However, careful considerations will be necessary because the sensitivity of the channeltron depends on the charge state of the detected ions.

References

[1] J. W. Kwan *et al*., “Ion Sources and Injector for HIF Induction Linacs”, Nucl. Instrum. and Methods A 464, p. 379-387 (2001).

[2] J. W. Kwan, “High Current Ion Source and Injectors for Induction Linacs in Heavy Ion Fusion”, IEEE Trans. on Plasma Sci., vol. 33 no. 6, December (2005).

[3] L. Z. Barabash *et al*., “Laser Produced Plasma as Ion Source for Heavy Ion Inertial Fusion”, Laser Part. Beams, vol. 2, part 1, pp. 49-59 (1984).

[4] Y. Y. Tsui, *et al*., “Single Shot Charge Analyzer for Laser-Produced Plasma Studies”, Rev. Sci. Instrum. 66 (1) p. 148-153 January 1995

Development of nano-second pulse generator with connecting arrester and effect of pulse widths on ozone yield and NO removal efficiency

Takatoshi Kakuta, Ippei Yagi* and Koichi Takaki

Department of Electrical Engineering and Computer Science, Iwate University, Morioka, Iwate 020-8551, Japan

**Department of Advanced Energy, The University of Tokyo, Tokyo, 227-8568, Japan*

ABSTRACT

An effect of pulse widths of applied voltage on ozone yield and NO removal efficiency were investigated experimentally. Nano-second high voltage pulse was generated using an inductive energy storage pulse power circuit with semiconductor opening switch and an arrester. Fast recovery diodes were utilized as semiconductor opening switch. The pulse voltage was applied to a center wire electrode in the corona reactor. The corona reactor had coaxial geometry and consisted of the center high-voltage wire and outer grounded cylinder electrodes. The pulse widths of applied voltage were reduced from 13 to 9 ns by connecting the arrester in parallel to the reactor. The ozone yield was improved from 270 to 300 g/kWh by connecting the arrester. The pulse widths of the applied voltage were reduced from 21 ns to 14 ns by connecting the arrester. The NO removal efficiency was improved from 8.2 to 35.7 g/kWh by connecting the arrester.

Keywords

Nano-second pulsed power generator, fast recovery diode, arrester, ozone generation, NO removal

1. Introduction

Ozone is a powerful oxidizing agent, which is used in a wide range of application such as water treatment and food processing and so on [(1)]. A nitrogen oxides (NO_x), including nitric oxide (NO) and nitric dioxide (NO_2) are exhausted from fuel combustion and industrial processes [(2)]. The emission of NOx into the atmospheric is one of the responsible factors for acid rains and atmospheric photochemical smog. There is pulse discharge as the ozone generation and NO removal methods [(3),(4)]. The pulse discharge is the promising high ozone yield and NO removal efficiency methods [(5),(6)]. The pulse discharge develops basically in two phases; streamer discharge propagation and glow-like discharge phases [(7),(8)]. When a positive high voltage is applied to a center electrode (i.e. anode), a small luminous zone called a streamer head develops from the center electrode to the outer electrode (i.e. cathode). The streamer head reaches the cathode and generates an ionized filament that bridges gap between the anode and the cathode. This initial phase of the streamer propagation is called a 'primary streamer'. After the arrival of the primary streamer at the cathode, a subsequent streamer develops from the anode toward the cathode. That is called a 'secondary streamer' or 'glow-like discharge'. The characteristics of the primary and secondary streamers are quite difference. The primary streamer includes a relatively large amount of high energy electron to dissociate the molecules such as nitrogen and oxygen. Therefore it is expected that the energy efficiency of the primary streamer is higher than that of the secondary streamer. Additionally, the continuous energy input during the secondary

streamer phase decrease the efficiency due to increase of gas temperature [9]-[11]. The pulsed power technique is expected to contribute to improve the energy efficiency in gas treatment process by reducing the duration time of the secondary streamer phase.

We developed the compact pulsed power generator using a semiconductor opening switch (SOS) for interruption of an inductor current within 100 ns [5],[12]. The SOS is suitable for production of a short pulse with high voltage because the reverse current can be interrupted within short time [13]. Moreover, the output voltage of the pulse generator using SOS can be changed easily by changing values of the circuit parameters [14],[15]. The waveform of the applied voltage to the corona reactor can also be changed by connecting the arrester in parallel to the reactor because the arrester is component for diverting the circuit current when the voltage reaches to the threshold voltage.

In this paper, we developed nano-second pulse voltage with connecting the arrester. The ozone yield and NO removal efficiency were evaluated with changing the pulse width of the applied voltage using nano-second pulse voltage without and with connecting the arrester.

2. Experimental Setup

Figure 1 shows a schematic of the pulse power circuit using SOS diode and the arrester. The pulse power circuit consists of primary and secondary circuits via a pulse transformer (Hitachi Metals Ltd., FT-3H). The primary circuit consists of a gap switch and a capacitor. The secondary circuit consists of a capacitor, an inductor, the SOS diode, a resistor and the arrester (Mitsubishi Materials Corporation, DSA-362MA). First recovery diodes (Voltage Multiplier K100UF) are utilized as semiconductor opening switch. The rated values of the diodes are 10 kV maximum voltage, 100 A maximum current and 100 A reverse current time. The capacitor stored in C_1 is charged by a dc voltage power supply. After closing switch, the charge C_1 flows through the pulse transformer to the SOS diode in forward direction.

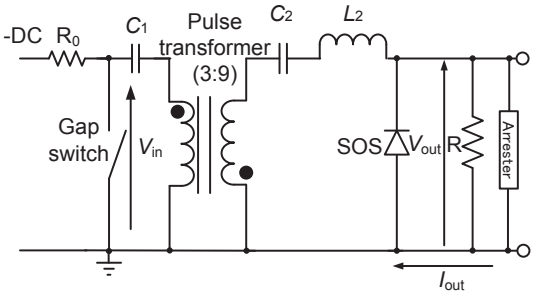

Fig. 1. Schematic of the pulse power circuit using SOS diode and the arrester.

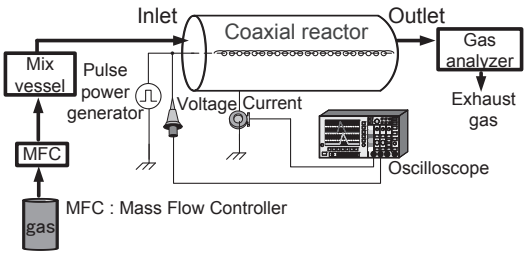

Fig. 2. Schematic diagram of the experimental setup for gas treatment.

After the pulse transformer saturates magnetically, the charge stored in C_2 flows through the SOS diode in reverse direction. Then the current in SOS diode is rapidly interrupted. As a result, a pulse voltage is caused by an induced electromotive force and is supplied to the output side of the circuit. The voltage and the current are measured using a high-voltage probe (Tektronix P6015A) and a current transformer (Bergoz CT-D1.0-B), respectively. Digital oscilloscopes (Tektronix DPO 4104B and Tektronix TDS3054B) are used to record the voltage and the current signals.

Figure 2 shows a schematic diagram of the experimental setup for gas treatment. The coaxial reactor consists of 2 mm stainless wire of the center electrode and 28 mm inner diameter stainless cylinder with the 300 mm in length. The center rod electrode is wrapped with spirally-twisted tungsten wire of 0.2 mm in diameter with 5 mm interval in order to decrease the corona onset voltage. For experimental ozone generation, the oxygen gas is fed in the reactor at 2 L/min in gas flow rate. The ozone concentration is measured using Ebara Jutugyo EG-2001B Ozone Monitor. For experimental NO removal, The NO gas is diluted with nitrogen and is

fed into the reactor at 5 L/min in gas flow rate. The NO initial concentration is set to be 200 ppm. The concentration of NO is measured using a gas analyzer (BEST Sokii BCL-511) at the outlet of the reactor.

3. Results

3.1 Electrical property

Figure 3 shows typically waveforms of the applied voltage, the discharge current and the energy consumption without and with connecting the arrester in oxygen gas. The pulse width is defined by duration time between 50 and 50 % of the peak voltage. The energy consumption is calculation from the applied voltage and the discharge current waveforms. The peak voltage is fixed at 31 kV. The pulse width without and with connecting the arrester are 13 and 9 ns, respectively. Also, the energy consumption without and with connecting the arrester are 17 to 11 mJ, respectively. The pulse width reduced to 4 ns by connecting the arrester. The energy consumption decreases by 65 % with connecting the arrester.

Figure 4 shows typically waveforms of the applied voltage, the discharge current and the energy consumption without and with connecting the arrester in nitrogen gas containing 200 ppm NO. The peak voltage is fixed at 30 kV. The pulse width without and with connecting the arrester are 21 and 14 ns, respectively. Also, the energy consumption without and with connecting the arrester are 67.1 to 5.8 mJ, respectively. The pulse width decreases to 7 ns by connecting the arrester. The energy consumption decreases by 8.6 % with connecting the arrester. It is confirmed that the energy consumption reduced by shortening the pulse width.

3.2 Ozone yield

Figure 5 shows ozone concentration as a function of input energy density. The pulse repetition rate is changed from 10 to 70 pps. The input energy density w [J/L] is expressed by following equation;

$$w = \frac{60 \cdot U \cdot f}{q} \cdots\cdots\cdots\cdots\cdots\cdots (1),$$

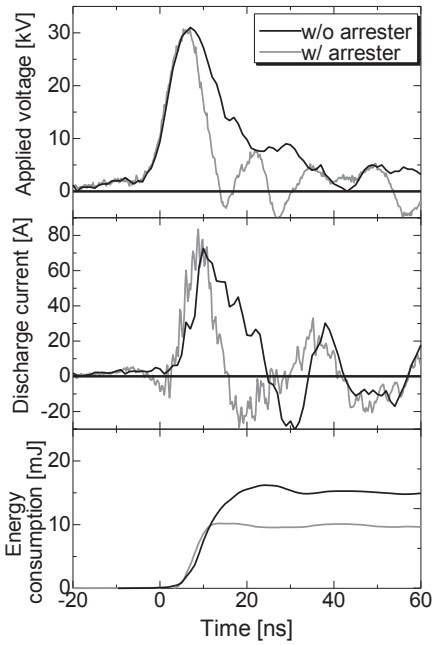

Fig. 3. Typically waveforms of applied voltage, the discharge current and the energy consumption without and with connecting the arrester in oxygen gas.

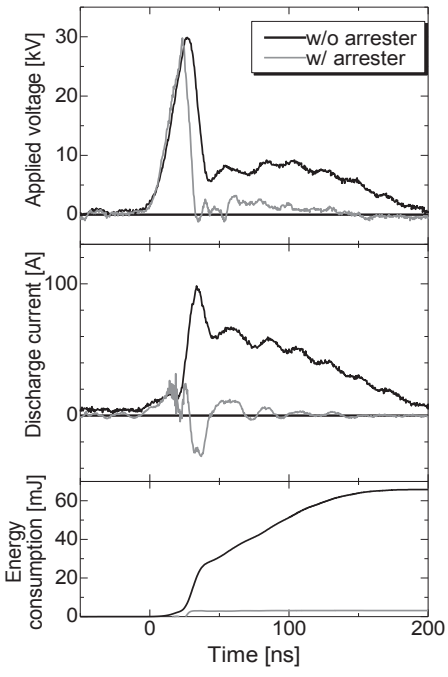

Fig. 4. Typically waveforms of the applied voltage, the discharge current and the energy consumption without and with connecting the arrester in nitrogen gas containing 200 ppm NO.

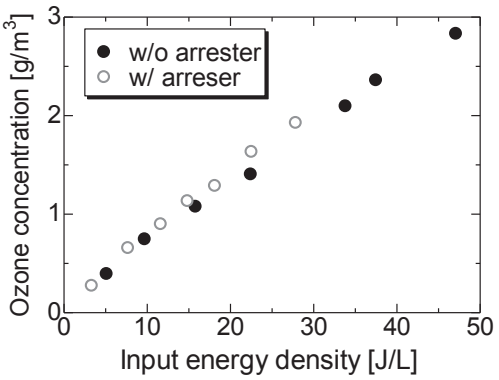

Fig. 5. Ozone concentration as a function of input energy density.

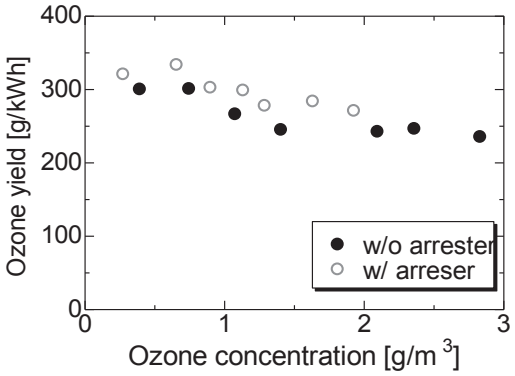

Fig. 6. Ozone yield as a function of ozone concentration.

where U [J] is the energy consumption per one pulse, f [pps] is pulse repetition rate and q [L/min] is gas flow rate. The ozone concentration increases with increasing the input energy density. When the input energy density is around 22.5 J/L, the ozone concentration with connecting arrester is higher than that without connecting the arrester.

Figure 6 shows ozone yield as a function of ozone concentration. The ozone yield η [g/kWh] is expressed by following equation;

$$\eta = \frac{60 \cdot q \cdot [O_3] \cdot M_{ozone}}{22.4 \cdot P} \times 10^{-3} \text{[g/kWh]} \cdots\cdots (2),$$

where q [L/min] is the gas flow rate, $[O_3]$ [g/m^3] is ozone concentration, M_{ozone} is ozone molecular weight and P [W] is consumed power in the reactor. The ozone yield decreases with increasing the ozone concentration. The ozone yields without and with connecting the arrester are 270 and 300 g/kWh, respectively, for around 1 g/m^3 ozone concentration. The ozone decomposition mainly occurs by following [1];

$$O_3 + O \rightarrow 2O_2 \cdots\cdots\cdots\cdots\cdots\cdots (3).$$

$$k = 1.8 * 10^{-11} \exp(-2300/T)[cm^3/s]$$

Namihira reported as duration time of the glow-like phase is longer, temperature in the reactor rises [11]. Also, the duration time of glow-like phase is longer as the pulse width increases. Moreover, the ozone dissociation occurs the glow-like phase because electron energy of glow-like phase is low [16]. Hence, it is indicated that the ozone yield decreases with increasing the pulse width.

3.3 NO removal efficiency

Figure 7 shows NO removal as a function of input energy density. The pulse repetition rate is changed from 10 to 90 pps. In figure 7, the NO removal increases with increasing input energy density. NO removal with connecting the arrester is higher than that without connecting the arrester in all energy density.

Figure 8 shows NO removal efficiency as a function of NO removal. NO removal efficiency η [g/kWh] is expressed by following equation;

$$\eta = \frac{60 \cdot q \cdot NO \cdot M_{NO}}{22.4 \cdot P} \times 10^{-3} \text{[g/kWh]} \cdots\cdots (4),$$

where q [L/min] is the gas flow rate, NO [ppm] is NO concentration after plasma treatment, M_{NO} is NO molecular weight and P [W] is consumed power in the reactor. The NO removal efficiencies without and with connecting the arrester are 8.2 and 35.7 g/kWh, respectively, for 30 % NO removal. The NO removal efficiency with connecting the arrester is approximately 4.4 times higher than that without connecting the arrester. The reduction of NO mainly occurs by the following processes in gas mixture of N_2 and NO [17];

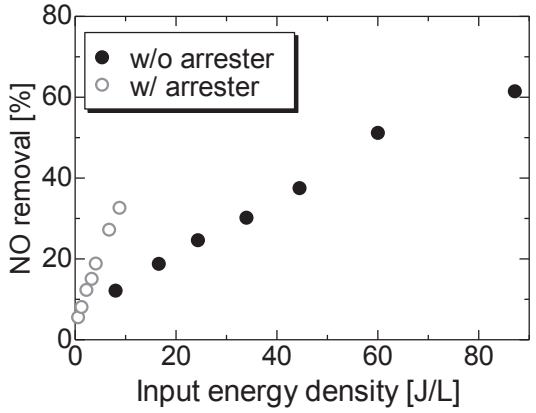

Fig. NO removal as a function of input energy density.

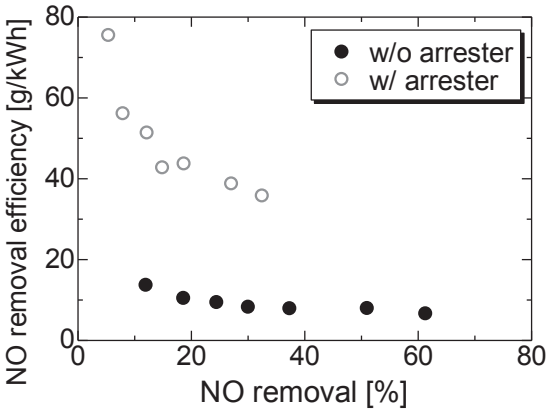

Fig. 8. NO removal efficiency as a function of NO removal.

$$e + N_2 \rightarrow e + N + N \cdots\cdots\cdots\cdots\cdots (5),$$
$$N + NO \rightarrow N_2 + O \cdots\cdots\cdots\cdots\cdots (6),$$

where *e* is electron. Therefore, this result indicates that the shorter duration time of the applied voltage contribute to improve the energy efficiency for production of N radical, which works as for the agent for NO decomposition in gas mixture of N_2 and NO Therefore, it was found that N radical produces effectively with reducing the pulse width.

4. Conclusion

The effect of pulse widths of applied voltage on ozone yield and NO removal efficiency were studied. We succeed the development of nano-second pulse circuit with connecting the arrester. The pulse width and the energy consumption with connecting the arrester are shorter than that without connecting the arrester. The ozone yield is improved from 270 to 300 g/kWh with connecting the arrester at 1 g/m^3 ozone concentration. The NO removal efficiency is improved from 8.2 to 35.7 g/kWh with connecting the arrester at 30 % NO removal. The ozone yield and NO removal efficiency are improved by reducing the pulse width.

Acknowledgments

The author would like to thank Dr. S. Mukaigawa at Iwate university for their valuable comments and discussions. The author would also like to thank Mr. Shida at Iwate university technical staff. This work was supported by a Grant-In-Aid of Science Research from Japan Ministry of Education, Science and Culture (JSPS Fellowship No 21246047).

References

(1) B.Eliasson, M.Hirth and U.Kogelschatz : J.Phys.D:Appl.Phys., **20** (1987) 1421.

(2) S.Hirata and A.Yukimura : IEEJ Trans. FM. **126** (2006) 443 [in Japanese].

(3) K.Takaki, I.Yagi, T.Fujiwara and T.Go : IEEE Trans. Dielectr. Insul. **18** (2011) 1752.

(4) T.Namihira, S.Tsukamoto, D.Wang, S.Katsuki, R.Hackam, H.Akiyama, Y.Uchida and M.Koike : IEEE Trans. Plasma Sci. **28** (2000) 434.

(5) D.Wang, T.Matsumoto, T.Namihira and H.Akiyama : J.Adv.Oxid.Technol., **13** (2010) 71.

(6) T.Matsumoto, D.Wang, T.Namihira and H.Akiyama : IEEE Trans. Plasma Sci. **38** (2010) 2639.

(7) R.Ono and T.oda : J. Phys. D ; Appl. Phys. **36** (2003) 1952.

(8) D.Wang, M.Jikuya, S.Yishida, T.Namihira and S.Katsuki and H.Akiyama : IEEE Trans. Plasma Sci. **35** (2007) 1098.

(9) E.J.M.van Heesch, G.J.J.Winands andA.J.M Pemen : J. Phys. D ; Appl. Phys. **41** (2008) 234015.
(10) O.Eichwald, O.Ducasse, D.Dubois, A.Abahazem, N.Merbahi, M.Benhenni and M.Yousfi : J. Phys. D ; Appl. Phys. **41** (2008) 234002.
(11) T.Namihira, D.Wang, T.Matsumoto, S.Okada and H.Akiyama : IEEJ Trans.FM. **129** (2009) 7 [in Japanese].
(12) I.Yagi, S.Mukaigawa, K.Takaki, T.Fujiwara and T.Go : IEEJ Trans. FM. **130** (2010) 549 [in Japanese].
(13) M.Gieselmann, M.Kristiansen, G.Grinstead and M.Wilson : IEEE Industry Application Conference **1** (2000) 588.
(14) I.Yagi, S.Okada, T.Matsumoto, D.Wang, T.Namihira and K.Takaki : IEEE Trans. Plasma Sci. **39** (2011) 2232.
(15) T.Sugai, W.Liu, A.Tokuchi, W.Jiang and Y.Minamitani : IEEE Trans. Plasma Sci. **41** (2013) 967.
(16) I.C.Walker, J.M.Gingell, N.J.Mason and G.Marston : J.Phys.B: At. Mol. Opt. Phys., **29** (1996) 4749.
(17) D.Wang, T.Namihira, S.Katsuki and H.Akiyama : J.Adv. Oxid. Technol. **8** (2005) 248.

Study of Cusp Magnetic Field Ion Source on IEC Device

Ngamdee Wantapon, Keita Nobe, Nanjo Kazuki, Kashiwagi Kouhei
Masato Watanabe and Eiki Hotta

Department of Energy Sciences, Tokyo Institute of Technology
4259 J2-35, Nagatsuta, Midori-ku, Yokohama, 226-8502 Japan

ABSTRACT

An Inertial Electrostatic Confinement Fusion (IECF) device is a compact fusion proton/neutron source with an extremely simple configuration, high controllability, and hence high safety. Previously, a cylindrical IECF device has been constructed with a 5 mm diameter single rod cathode. With this configuration, accelerated ions which move toward the cathode have probability of hitting and thus damaging the cathode. To increase durability of this device, a cathode with 4 parallel rods which provide a space at the center has been used instead of a single rod cathode. The center space among cathode rods is used for ion recirculation. The diameter of cathode rod is 3 mm, which enables the cathode to withstand the damage caused by hit of high energy ions. Furthermore, a cusp magnetic field configuration generated by small permanent magnets placed on the outer chamber wall is also used in this experiment in order to trap and force electrons to circulate near the anode, which will contribute to the generation of more ions near the anode. Moreover, pulsed discharge operation has been adopted. Normally a neutron production rate (NPR) increases with increasing discharge current and voltage, however an operation in high current and voltage for long time will damage the cathode and the inner wall of chamber. The operation in pulsed mode allowed us to expand experimental condition range to higher current of a few amperes without damaging the cathode and the chamber wall.

Keywords

Key Words: fusion, cusp magnetic field, confinement

1. Introduction

An Inertial Electrostatic Confinement (IEC) fusion device is a compact and simple fusion device. Generally, it is composed of a spherical anode (chamber) and a grid cathode which is set at the center of the anode. By applying negative high voltage to the cathode, glow discharge occurs and then the generated ions are accelerated toward the cathode by a strong electric field. These ions have high probability of colliding with each other, which leads to nuclear fusion. This is how the IEC device works for fusion reaction. Normally, fusion reactions occurring in the IEC device can be classified according to fuel gas as follows [1];

$$D + D \rightarrow {}^{3}He + n \quad (1)$$
$$T + p \quad (2)$$
$$D + T \rightarrow {}^{4}He + n \quad (3)$$
$$D + {}^{3}He \rightarrow {}^{4}He + p \quad (4)$$

Above equations show that fusion reaction can produce neutrons and/or protons, but in the typical IEC device its fusion rate (10^{6}-10^{8} neutron/s) is still very low compared to productions from nuclear fission reactor (10^{13} neutron/s/cm^{2} or more). Therefore one of the challenging objectives in IEC research is the increase of its fusion rate. The reactions which play important roles behind fusion reaction in IEC device can be classified as follows [2-3];

Beam – Beam (BM-BM)
Beam – Background neutral gas (BM-BG)
Beam – Cathode (BM-C)
Beam – Anode (BM-A)

As shown in Fig. 1, “Beam” represents energetic particles including positive ions, negative ions and fast neutral particles

Increase of a fusion reaction rate means to increase any reaction rate mentioned above. Normally, the Beam-Beam reaction is the most effective one because its reaction rate is proportional to the square of discharge current while the other reaction rates are merely proportional to the discharge current.

However, this is not a major reaction in the IEC system. Because the major reaction in the IEC system is a beam-background reaction, it is needed to increase the number of this reaction to get the higher fusion rate in the IEC device.

One of attempts was to apply a uniform axial magnetic field to confine electrons to travel around anode due to **ExB** drift motion. These electrons will generate more ions by collisional ionization process. Thus the region near the anode acts as an ion source for fusion. The generated ions are accelerated to the cathode by electric field and fuse when they collide with each other. The system is called Magnetic-assisted Electrostatic Confinement (MEC) [4]. The axial magnetic field avoids ions hitting against the cathode by bending their inward orbits due to Lorentz force.

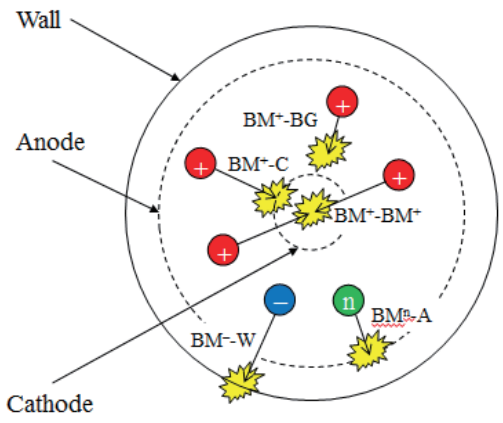

Fig. 1 Interactions related to fusion reaction in IEC

However, with the axial uniform magnetic field, electrons had been confined even near the cathode. The electrons near the cathode also contribute to the ionization, which leads to generation of many low energy ions because the ions are generated near the cathode. To prevent this situation, a new improvement has been studied, that is, application of cusp magnetic field near the chamber wall instead of the axial uniform magnetic field. With azimuthal cusp magnetic field configuration, electrons are forced to circulate along the chamber wall [5].

To measure the fusion reaction rate in this IEC device, a He-3 proportional counter was used. In our study, we use only deuterium gas as fuel gas, so that the fusion reaction occurring in the device is related to equations (1) and (2), which take place evenly.

2. Experimental Setup

Figure 2 shows the magnet configuration in IEC device which generates point cusp magnetic field. Permanent magnets (max. 120 mT at surface) with dimension of 10 mm x 4 mm x 4 mm are placed around outer side of chamber. A cylindrical vacuum chamber made of stainless steel has inner diameter of 118 mm and height of 160 mm. Four cathode stainless steel rods of 3 mm in diameter are placed at 7.5 mm from the center of the chamber.

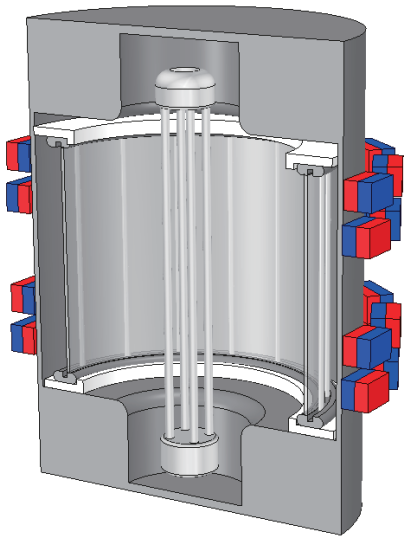

Fig. 2 IEC configuration with small permanent magnets around chamber wall

A mesh anode is placed at 10 mm far from the inner wall surface. Deuterium gas has been

introduced into the chamber through a mass flow controller and the pressure is maintained in a range of a few Pa.

From a calculation, when a voltage of -20 kV is applied to the cathode, while a space between the cathode and the grounded inner wall of chamber is 5 cm, an electric field of -4x10^5 V/m toward the center of chamber (Ex) was generated. By applying 40 to 50 mT of azimuthal magnetic field (Bz), the Larmor radius of electron that has been trapped by Bz is about 10 mm. While the Larmor radius of ion is about 60 cm. Compared to the space between the wall and the anode (10 mm), the electron Larmor radius should not be larger than the anode-wall space. These electrons trapped near the wall will contribute to the generation of more ions near the anode.

Comparing 50 mm of anode-cathode space and 60 cm of ion Larmor radius, the ion Larmor radius is much larger than the anode-cathode space, so that we can assume that the magnetic field we used does not interfere ion trajectory in the anode-cathode space.

Working voltages and currents that are applied to the cathode have been varied from -20 kV to -30 kV and 1 to 8 A in pulsed operations at repetition rate of 50 Hz. Typical waveforms measured in this experiment are shown in Fig. 3.

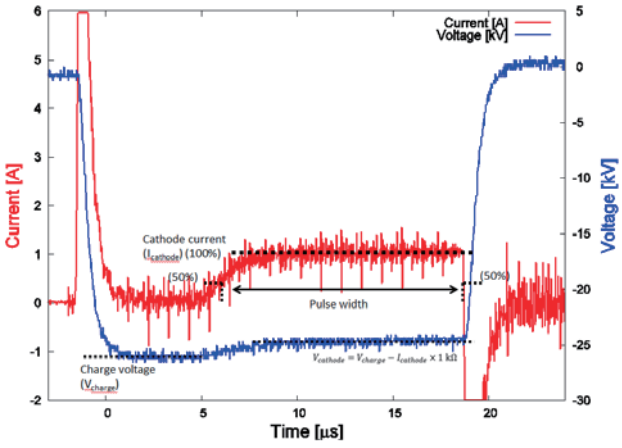

Fig. 3 Typical waveforms in this experiment

The benefit of pulsed operation is allowing us to use higher current without destroying the cathode due to overheat. Because NPR is directly proportional to current in this system, we can expect higher NPR for higher current, which is available in pulsed operation. Small magnets were set as shown in Fig. 4 a) or b) in which red blocks refer to North Pole while blue blocks refer to South Pole of permanent magnets. With different magnet configurations, different cusp magnetic fields will be generated as shown in Fig. 4. Figure 4 a) provides point cusp magnetic field and b) provides line cusp magnetic field.

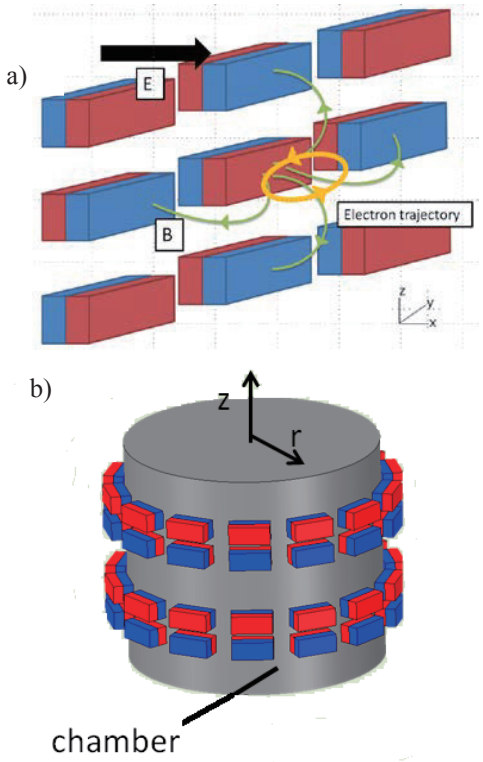

Fig. 4 Permanent magnets configurations: a) point cusp b) line cusp

In this report, the configuration shown in Fig.4 b) was used. Hence azimuthal line cusp magnetic field is generated, which is expected to trap electrons and makes them circulate near and along chamber wall by **ExB** drift. These trapped electrons have high possibility to generate ions near the wall due to electron impact ionization.

3. Results and Discussion

3.1 Line Cusp magnetic field distribution

The component of magnetic field in line cusp used

for trapping electrons in this experiment is z component (Bz), which is perpendicular to electric field. The radial distribution of Bz measured between the axially adjacent cusp magnets is shown in Fig. 5. It is clearly seen that a high value of Bz appears near the wall. Magnetic flux density decreases rapidly within a few cm from the wall.

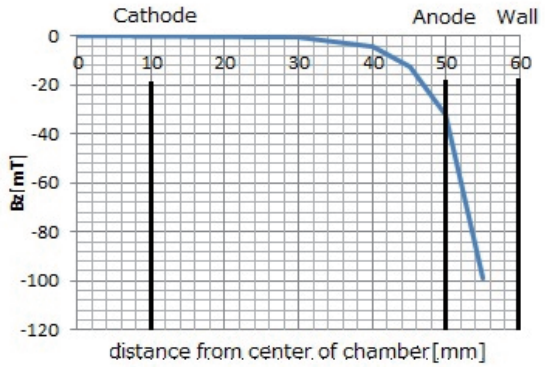

Fig. 5 Bz distribution

However from Fig. 5, it is seen that Bz in anode-wall region has magnetic flux density of 40-100 mT which is corresponding to 0.2-0.9 mm of electron Larmor radius if they are accelerated through an electric field of 400 kV/m. This means that Bz can trap electrons to remain only in wall-anode region.

3.2 Discharge voltage vs discharge current with and without cusp magnetic field

In this section, we study the variation of discharge voltage and current with working pressure in case of with and without cusp magnetic field. The result is shown in Fig. 6.

It is clearly seen that the discharge voltage is directly proportional to current in pressure range from 35 to 50 mTorr. Cusp magnetic field seems to reduce discharge voltage needed for maintaining a discharge because electrons trapped in anode-wall region can generate more ions due to electron impact ionization, thus the power required to maintain discharge is reduced.

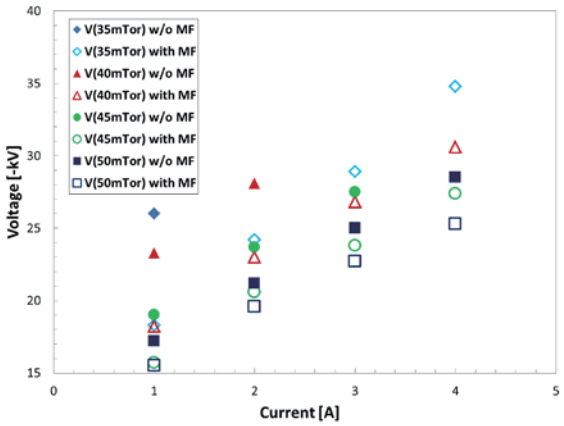

Fig. 6 Discharge voltage and current variation with working pressure

Discharge voltage required to maintain a discharge varies with pressure. It is found that in lower pressure range (35 mTorr), the discharge voltage is 35 kV at 4 A, on the other hand, in higher pressure range (50 mTorr) the required voltage becomes lower (25 kV) because at high pressure there is plenty of fuel gas to be ionized, and thus plenty of ions and electrons. As a result, a voltage needed to maintain the discharge at higher pressure becomes lower than that at a lower pressure.

3.3 Dependence of NPR on cathode current

In this section, we study dependence of NPR on cathode current with applying cusp magnetic field.

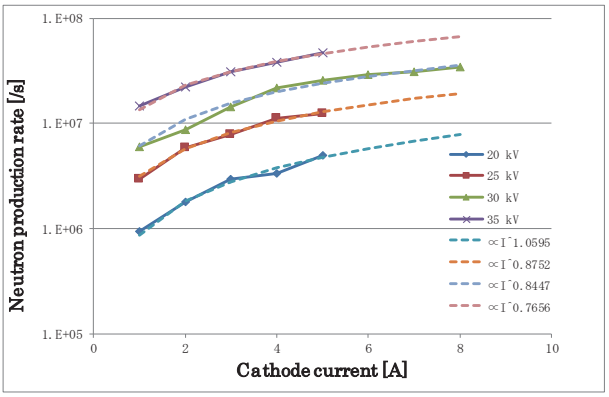

Fig. 7 Dependence of NPR on discharge current

The relationship between NPR and current obtained in pulsed mode is shown in Fig. 7. Experimental data are shown by colored points while

estimated trend lines are shown by broken lines. From this graph, NPR in pulsed mode is almost proportional to the 1st power of cathode current. The highest exponent of cathode current is 1.06, which is obtained at the lowest applied voltage of -20 kV. On the other hand, the lowest exponent is 0.76 for the highest applied voltage of -35 kV, while the highest NPR comes from the highest applied voltage. This means that the rate of NPR increment is high at low applied voltage (in low NPR region), however when the NPR is increased (in high NPR region) the rate becomes lower.

3.4 NPR with and without cusp magnetic field and effect of anode resistance

The relationship between NPR and the cathode current is shown in Fig. 8, which indicates that NPR is increased when cusp magnetic field is applied to the system. This indicates the possibility that cusp magnetic field traps electrons in the anode-wall region and that the trapped electrons contribute to an increase of ionization near the anode as expected. The generated ions in anode-wall region are accelerated by electric field to fuse at the center of chamber. With an increase of ion density near the anode, which plays a role as an increase of fusion fuel, the increase of fusion rate in term of NPR is expected.

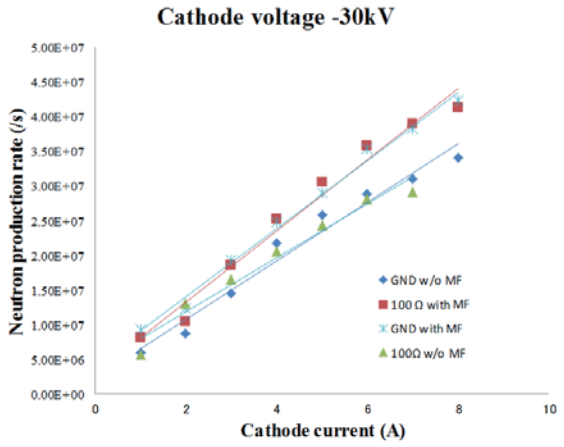

Fig. 8 NPR vs. cathode current with and without anode resistance

From Fig. 8, it can be also seen that NPR increases in proportion to the cathode current for both with and without applied cusp magnetic field. This means that even though the applied cusp magnetic field can improve NPR, it does not change the main fusion reaction in this device, and the main fusion reaction is still not the Beam-Beam but the Beam-Background reaction as we have already discussed in section 1.

The effect of anode resistance on NPR was also studied. An anode resistance is used to give the anode the bias potential. When the anode potential is biased, its potential is not zero anymore and an electric field between anode-wall has been established. We expect that if the electric field between anode and the wall is strong enough, it could extract more ions from the anode-wall region to the cathode-anode region. Combining with the effect of cusp magnetic field, it is expected that the application of anode bias potential contributes to the increase of NPR. However, in Fig. 8, it is seen that anode bias potential does not contribute to the increase of NPR on the contrary to our expectation. This means that the dominant factor to increase NPR in this experiment is the magnetic field. We need to conduct more experiments before we can get a reliable conclusion on the effect of anode bias resistance on NPR.

4. Conclusions

A cusp magnetic field generated by small permanent magnets of 120 mT can trap electrons in the region between the inner wall of chamber and the anode. These trapped electrons can generate more ions in the system so that it can reduce the applied cathode voltage used for maintaining the discharge. In addition, ions generated in the wall-anode region can be fully accelerated by electric field, which leads to the enhancement of NPR.

A study of discharge voltage and current dependence on cusp magnetic field showed that the discharge voltage is directly proportional to the current while cusp magnetic field can reduce the discharge voltage.

Even in the case of cusp magnetic field applied, NPR still increases in proportion to the discharge current. This fact shows that the main fusion reaction

in this device is a Beam-Background reaction.

Although the anode bias potential by connecting a resistance between the anode and the ground was applied, no difference was found between the NPR obtained by with and without bias potential. An enhancement of NPR was found only when a cusp magnetic field was applied. In order to clarify the effect of a bias anode resistance on NPR, deeply detailed experiments with anode resistances of different values are required.

References

[1] G. H. MILEY et al., "Inertial-Electrostatic Confinement Neutron/Proton Source", *Proc. 3rd Int. Conf. on Dense Z-pinches*, AIP Press, pp.675–688 (1994).

[2] K. YAMAUCHI et al., "Neutron Production Characteristics and Emission Properties of Spherically Convergent Beam Fusion", *Fusion Technol.*, **39**, 3, pp.1182–1187 (2001).

[3] T. A. THORSON et al., "Fusion Reactivity Characterization of a Spherical Convergent Ion Source", *Nuclear Fusion,* **38**, 4, pp.495-507 (1998).

[4] K. TOMIYASU et al., "Particle-in-cell simulation of magnetic-assisted electrostatic confinement device", *Fusion Engineering and Design*, **85**, pp.728–733 (2010).

[5] Kei Takakura et al., "Effects of azimuthal cusp magnetic field on neutron production rate in a cylindrical inertial electrostatic confinement device", *13th US-Japan Workshop on Inertial Electrostatic Confinement Fusion (IEC 2011)*, Book of Abstract, WE-07, p.11 (2011).

Magnetic field control of pulse magnetron glow plasma

Takumi Konishi[a], Koichi Takaki[a] and Ken Yukimura[b]

[a]*Iwate University, 4-3-5 Ueda, Morioka, Iwate 020-8551, JAPAN*
[a]*Iwate Universit and Nanoelectronics Research Institute,National Institute of Advanced Industrial Science and Technology-Tsukuba Central,Ibaraki 305-8568*

ABSTRACT

A power deposition in pulsed magnetron glow plasma and the plasma density were controlled by magnetic field distribution. The pulsed magnetron glow plasma was produced using a pulse modulator, which supplied -2.1 kV repetitive pulse at 7 μs in pulse width. The magnetic field distribution was arranged using neodymium magnets which were put behind a carbon target disk. The pulse magnetron glow plasma generated along a race trace i.e. position of maximum amplitude of radial magnetic field. The power deposition increased with increasing pulse voltage applied to the carbon target. The diameter of the race trace increased with increasing number of the internal magnets which were located of the center of the target. However, the peak intensity of the light emitted from the plasma and the power deposition decreased with increasing number of the internal magnets. The argon and carbon ions were confirmed in the plasma from spectroscopic measurement. The number densities of the ions increased with voltage applied to the target.

Keywords

HiPIMS, DLC, Glow plasma, Magnetic field distribution

1. Introduction

High power impulse magnetron sputtering (HiPIMS) is a novel physical vapor deposition technology. The technology allows for production of high density plasma without macroparticle generation, very high electron densities are achieved. The high electron density results in a high ionization fraction of the sputtered vapor [1]. Magnetic field design is important in magnetron sputtering to affect the plasma and the film deposition. Magnetic mirroring, a consequence of magnetic moment conservation, may occur as the electron gyration center follows the field line into a region of increasing field. The electron gyration center exhibits a pendulum-like motion, following the arch of the magnetic field structure, due to magnetic mirroring and reflection by the electric field [2]. Thus, magnetic field configurations of different ***B***-field strengths changes race track widths and race track patterns.

Diamond-like carbon (DLC) films have attracted much attention as a hard coating due to excellent mechanical properties which take advantage of the high mechanical hardness, low friction, optical transparency and chemical inertness of the material [2-5]. DLC films therefore have been prepared by many methods, such as magnetron sputtering, vacuum arc deposition, pulse laser deposition, plasma assisted chemical vapor deposition and plasma based ion implantation.

This paper describes the influence of magnetic field distribution on power deposition of the plasma. The high-density plasma was produced using a HiPIMS discharge at source voltage of -2100 V for various magnetic field distributions. This source voltage is high enough compared with that of conventional magnetron discharge [1]. The high voltage application, however, induces transition of the plasma from a glow to an arc discharges. To avoid the arcing the magnetic field configurations on the target should be optimized. Therfore, the high-power magnetron

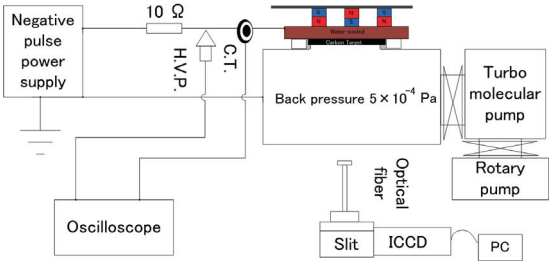

Fig. 1 Schematics of the experimental setup. ; H.V.P.: High voltage probe. C.T.: Current probe.

plasma with a high current was evaluated for various magnetic field distributions.

2. Experimental Setup

Fig. 1 shows schematics of the experimental setup. A cylindrical vacuum chamber was evacuated down to 5 $\times 10^{-4}$ Pa. A carbon disk of 150 mm diameter was utilized as the target. An insulated-gate bipolar transistor was used as the closing switch to transmit the energy from the charged capacitor to the magnetron sputtering plasma. The visible and ultraviolet optical emission spectra from the HiPIMS glow plasma were observed using a spectroscope with a gated intensified charge-couple device (ICCD, Model Andor type DH510).

The magnet arrangement was configured as shown in Fig. 2(a) for n = 1, (b) for n = 3, and (c) for n = 7 inner magnets. The magnets were arranged in a concentric circle. By varying n, both the magnetic flux density on the target and its distribution were altered. Hence, n altered the location of the generated plasma. The magnetic flux was in a direction parallel to the target surface at the location of the two peaks in the magnetic flux density. The peaks of the magnetic flux density moved toward the outside of the target as n increases. Thus, the location of plasma generation moved toward the grounded plate of the magnetron sputtering plasma.

3. Results and Discussion

3.1 Magnetic Flux Density

Fig. 3 shows spatial-distribution of the magnetic

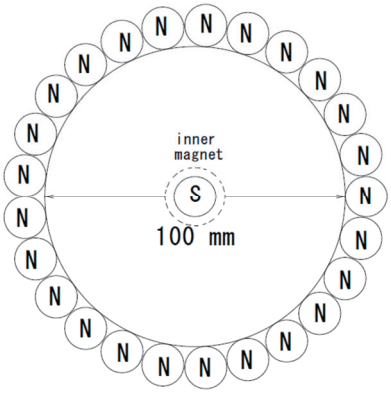

(a) n = 1

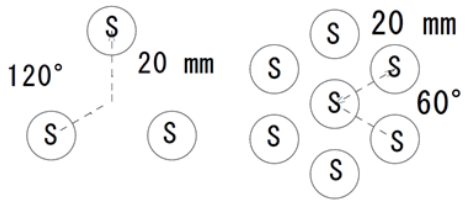

(b) n = 3 (c) n= 7

Fig. 2 Arrangement of external magnets at number of the inner magnets are (a) one, (b) three, and (c) seven.

flux density for (a) radial and (b) the axis directions. The central position of the target is 0 mm position. The distribution is symmetric to the center of the target. There are two peaks in the magnetic flux density observed on the target surface. The magnetic flux is in a direction parallel to the target surface at the location of the two peaks in the magnetic flux density. The peaks of the magnetic flux density move toward the outside of the target as n increases. Thus, the location of plasma generation moves toward the grounded plate of the magnetron sputtering (MS) plasma production system [6].

3.2 Plasma Power Characteristics

Fig. 4(a) and (b) shows the waveforms of the target voltage, the current through the target and the power consumed in the MS glow plasma. The glow plasma is produced at instance of the application of the source voltage. As time passes, the current linearly

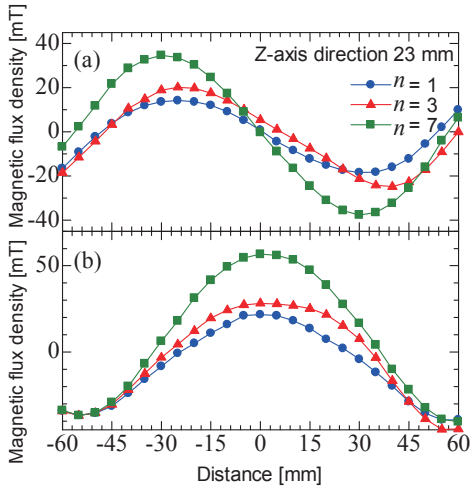

Fig. 3 Spatial-distribution of magnetic flux density for (a) radial and (b) the axis directions.

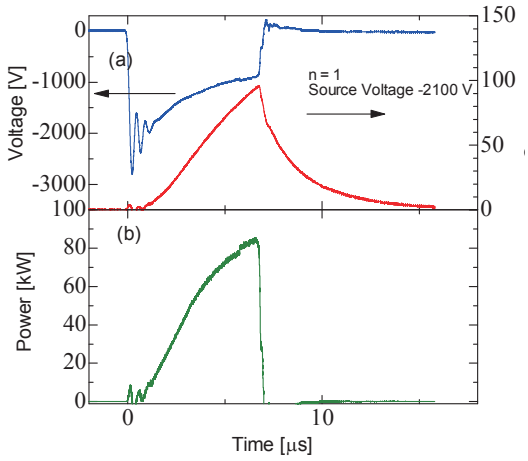

Fig. 4 Time-dependent behavior of (a) target voltage ,the glow current, and (b) power consumed in the glow plasma at n = 1 for source voltages of -2100V.

increases and the target voltage decreases due to the decrease of the plasma impedance. The target voltage at the end of the pulse is -900 V with a source voltage of -2100 V. The target voltage decreases by approximately 40% from the source voltage, whereas

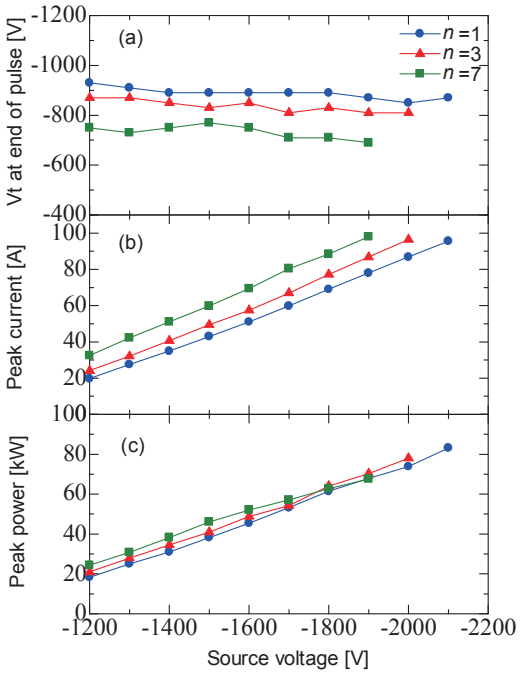

Fig. 5 Dependency of target voltage, current, power deposition in the plasma or initial source voltage for three different magnet number.

the current changes from zero to 100 A during the voltage pulse. Therefore, the consumed power is almost determined by the current. In the after-glow region, the target voltage returns to the ground voltage in less than 1 μs, whereas the current decreases gradually in approximately 8 μs due to the residual ions.

Fig. 5(a)–(c) shows the target voltage, the glow current, and the consumed power at the end of the pulse voltage as a function of the source voltage. The source voltage was charged from -1200 to -2100 V for each condition of the inner magnet. The maximum values, which mean the glow-to-arc transition, were limited because the stable glow discharge was maintained by applying the source voltage for each condition of the inner magnet. For example, the glow discharge of n = 3 is maintained stably at -2000 V source voltage, whereas the glow discharge transits to the arc discharge source voltage -2100 V. There is a tendency that the glow-to-arc

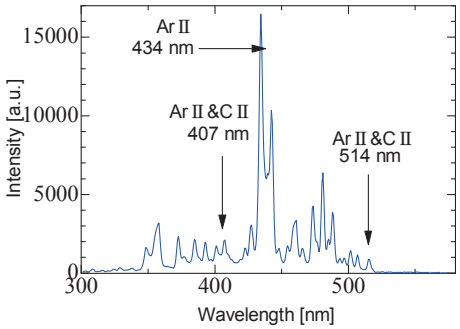

Fig. 6 The spectrum of optical emission of the MS glow plasma for the source voltages of -2100 V at n = 1.

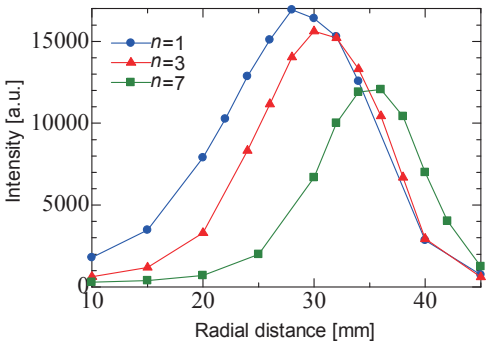

Fig. 7 Spatial-distribution for the wavelength of 434 nm in the spectrum at 7 μs after applying voltage for three different magnet numbers.

discharge transition voltage decreases with increasing value of n; specifically, the threshold voltages were approximately -2100 V, -2000 V, and -1900 V for n = 1, for n = 3, and for n = 7, respectively. The glow voltages at the end of the pulse were approximately -900 V, -880 V, and -720 V, respectively.

3.2 Optical Emissions

Fig. 6 shows the spectrum of optical emission from the MS glow plasma at source voltages of -2100 V and n = 1. Several peaks of argon and carbon ions are observed. It was found that the peak intensity of Ar II is higher than others.

Fig. 7 shows spatial-distribution of light emission

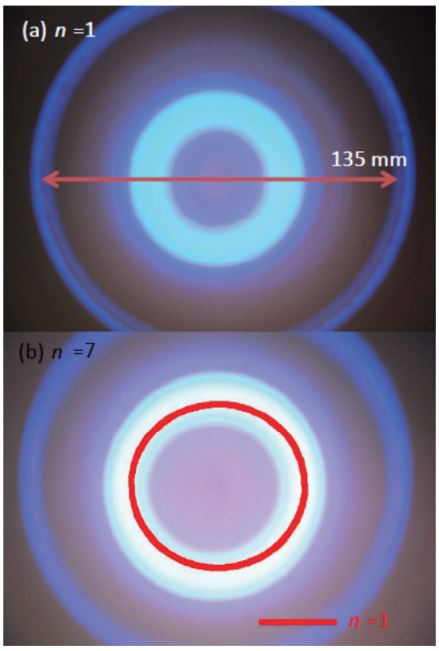

Fig. 8. Photos of the light emission from the plasma at (a) n = 1 and (b) n = 7.

intensity the wavelength of 434 nm at 7 μs after applying voltage for three different magnet numbers. It is confirmed that the plasma is produced at the peak position of the magnetic flux density. The peak position of the light-emission intensity is shifted towards radial direction with increasing number of the inner magnets. It is noticed that the glow discharge is transited to an arc discharge by the number of inner magnets. Because the plasma production zone changes with increasing the number of inner magnets, the arc transition voltage is reduced by decrease the number of inner magnets.

3.3 Light emission from the plasma

Fig.8 (a) and (b) shows still photos of the HiPIMS plasma at n = 1 and n = 7, respectively. It is found that ring-shaped plasma is produced and the number of inner magnets affects the location of the plasma production, where the magnetic flux density peaks and is in a direction parallel to the target surface. Therefore, the plasma production zone is extended in the radial direction with increasing the number of the inner magnets.

4. Conclusions

In this paper, we discussed the influence of the magnetic field configuration on the distribution and the power consumption of the HiPIMS glow plasma was studied experimentally. The magnetic flux density on the target and its distribution are altered by modifying the arrangement of the permanent magnets, which is configured in an unbalanced concentric circle. The power consumed in the plasma at the threshold voltage of the glow-to-arc transition also decreases with increasing the number of inner magnets. Therefore, it has been found that a higher source voltage can be applied to the target when the number of inner magnets is small. Moreover, the highest glow voltage with the highest power consumption can be obtained at at n = 1 in our experiments.

References

[1] U.Helmersson, M.Lattemann, J.Bohlmark, A.P. Ehiasarian, J.T.Gudmundsson "Ionized physical vapor deposition (IPVD): A review of technology and applications", *Thin Solid Films*, vol. 513, no. 1/2, pp.1-24. August. 2006

[2] K. Yukimura, H. Ogiso, S. Nakano, K. Takaki, "Carbon Ion Production Using a High-Power Impulse Magnetron Sputtering Glow Plasma", *IEEE Trans. Plasma Sci.*, vol. 41, no.10, pp. 3012-3020. Oct. 2013..

[3] K. Takaki, O. Kumagai, S. Mukaigawa, T.Fujiwara, M. Kumagai and K. Yukimura, "Ion Extraction From Magnetically Driven Carbon Shunting Arc Plasma", *IEEE Trans. Plasma Sci.,* 34, 4, pp.1209-1215 (2006).

[4] K. Yukimura and S.Masamune, "Shunting Arc Plasma Generation over a Wide Range of Ambient Pressure and Ion Extraction", *Rev. Sci. Instrum.*, **73**, pp.860-862 (2002).

[5] K. Yukimura, M. Kumagai, M. Kumagai, H. Saito, M. Kohata and K. Takaki, "Deposition of Amorphous Carbon Using a Shunting Arc Discharge", *Surf. Coat. Technol.,* 174/175, pp.1187-1190 (2003).

[6] A. E. Wendt and M. A. Lieberman, "Spatial structure of a planar magnetron discharge", *J. Vac. Sci. Technol*. A, vol. 8, no.2, pp.902-907, 1990.

Power Flow in Counter-facing Plasma Guns for Extreme Ultra-Violet Plasma Light Source

Koki Kano[1], Shi Jia Liu[1], Tatsuya Sodekoda[2], Hajime Kuwabara[2], Akira Tokuchi[3], Mitsuo Nakajima[1], Tohru Kawamura[1], and Kazuhiko Horioka[1]

Department of Energy Sciences, Tokyo Institute of Techology[1], Nagatsuta 4259, Midori-ku, Yokohama, 226-8502, Japan

Yokohama Engineering Center, IHI Corporation[2], Shin-nakaharacho 1, Isogo-ku, Yokohama, 235-8501, Japan

Plused Power Japan laboratory ltd.[3], Oji 2-3-16, Kusatsu, Shiga, 525-0032, Japan

ABSTRACT

The total energy consumed in the load of a laser-triggered discharge produced plasma light source was measured as functions of the applied voltage, the electrode polarity and the laser energy. When the device operated with negative polarity, the energy consumed in the load was low in comparison with positive mode. In addition, when the laser energy increased, the consumption energy decreased a little.

Keywords

Keywords : EUV light source, Plasma focus, High energy density plasma, Electrode erosion

1. Introduction

Extreme Ultra-Violet (EUV) light sources are attracting our attention as the next generation photolithography. We have developed a counter-facing plasma focus system for the EUV light source, and have been challenging for the practical use of the device. Highly repetitive and long-life operation are required for the practical use. Hence efficiency improvement with the reduction of the electrode heat load is necessary. Therefore the final goal of this research is to develop a high efficiency EUV plasma source with decreasing the electrode erosion.

Although it is said that the degree of integration of an integrated circuit increases 4 times every three years [1], this has been supported with the lithography technology especially the development of a practical light source. The minimum processing size of a photolithography depends on the wavelength of the light source, and Extreme Ultra-Violet (EUV) plasma light sources are attracting our attention as a short wavelength light source for the next generation micro fabrication.

The EUV light is contained in a radiation from a high energy density plasma (T_e=10~30 eV, n_e=10^{18}~10^{19} cm^{-3}) [2]. Practical schemes of the light source are classified as Laser Produced Plasma (LPP) [3] and Discharge Produced Plasma (DPP) [4]. In order to realize a practical EUV light source, high average power is of crucial importance. However, when the input power is increased simply for higher output power, life time of the device, such as electrodes and the optical component, are degraded by the huge thermal load accompanied by the electrode erosion and undesirable byproducts; debris. Therefore, coexistence of high average power and reduction of the heat load to the device component becomes indispensable for practical light source.

We have developed a counter-facing plasma focus system for the EUV light source [5], which may be classified into Laser triggered DPP. The pulse output of EUV light was typically 100mJ per shot [6]. The final goal of this research is to develop a practical EUV plasma source using the counter-facing configuration. Thus, as the following step towards the practical use, we are aiming at repetitive operations with 1 kHz - 10 kHz. However, because the conversion efficiency from the plasma to the output EUV energy is a few percent at most, increase of the heat load to electrode is expected in performing the highly repetitive operation.

At first, the consumption energy of the whole load per one shot was measured, and it is investigated how much energy was consumed in the plasma, at the electrodes, and transformed to the device components. If it is possible to evaluate the details of power flow in the EUV device, we can optimize the discharge condition, in which the heat load is smaller and the conversion efficiency is larger.

In this paper, the energy consumed in the whole load per one shot is measured as a function of the electrode polarity, applied voltages and the laser energy. The influence of those factors is discussed based on the results.

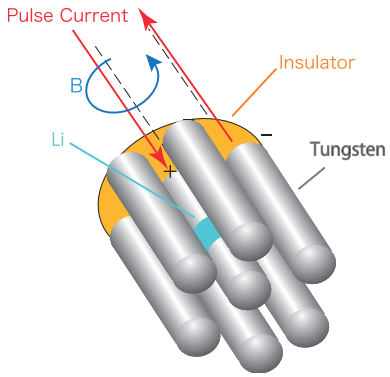

Fig.1 Electrode geometry of counter-facing plasma focus system.

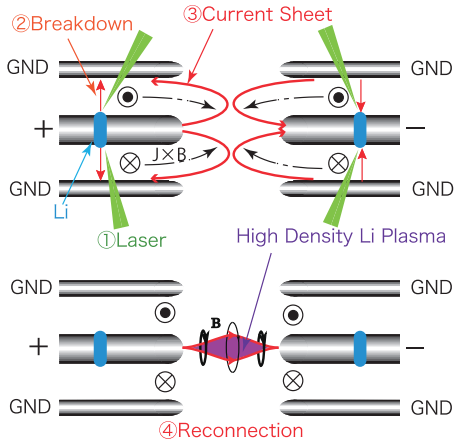

Fig. 2 Operation of counter-facing plasma focus system.

2. Experimental Setup and Method

2.1 Couter-facing Plasma Guns for EUV light source [5]

Figure 1 shows a schematic of the electrodes which has a plasma focus configuration. The operation procedure is shown in Fig. 2.

At first, voltages are applied between six independent outer electrodes and one center electrode. A pulse discharge is induced between the electrodes by irradiating a YAG laser on a Li source attached to the center electrode. Then, the plasma is accelerated to the top of center electrodes by the Lorentz force, which is generated by interaction of the current flowing in the plasma sheet and the self-magnetic field. The counter moving plasmas collide and thermalize in the center of electrode gap. As shown in Fig.2, the current sheets can reconnect when the electrodes are charged with reverse-polarity mutually. Then a high energy density plasma can be confined and make a bright EUV radiation for a long time.

2.2 Measurement of Consumption Energy in the Whole Load

Figure 3 shows a circuit diagram of the experiment that corresponds to one of the six channels. As shown, the current and the potential difference between the electrodes are measured by a Rogowski coil and a high-voltage differential probe respectively. The energy was calculated by time-integration of the current and the potential difference product.

Figure 4 shows an illustration of the potential

distribution between electrodes. As shown, we measured the potential differences of not only the plasma but also sheaths and obtained consumption energy in the whole load.

In this experiment, we operated the plasma focus device with single-side mode. The current waveform

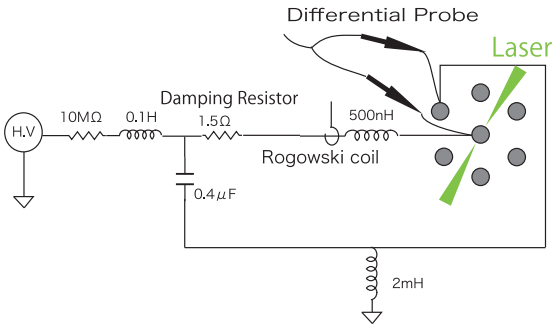

Fig. 3 Circuit diagram of the experiment.

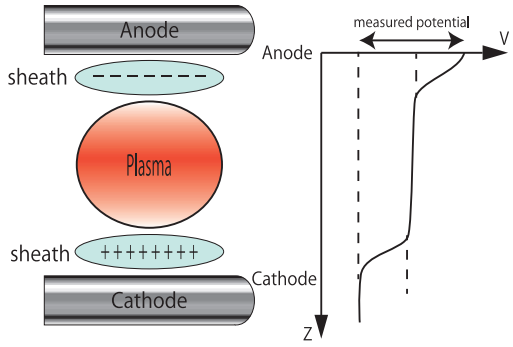

Fig. 4 Potential distribution between electrodes.

was regulated by putting a damping resistor to secure the stable EUV output. When we perform highly repetitive operation, we will use a power supply with an energy recover unit, which applies first half period of current to the load and the remainder is recovered for the next operation. We used a Nd:YAG laser for the formation of initial plasma with 2ω (532 nm) mode and 15 ns pulse width. In this experiment, we measured power input as a function of the applied voltages, the polarity, and the laser energy.

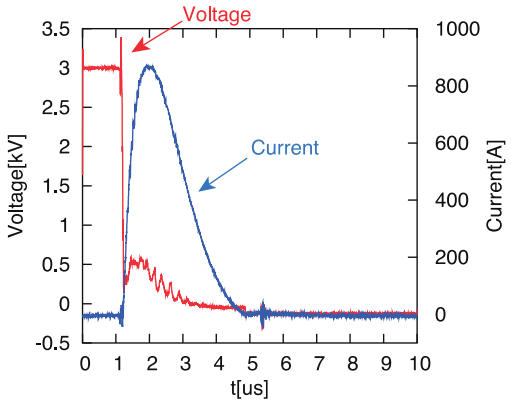

(a) Center electrode : positive

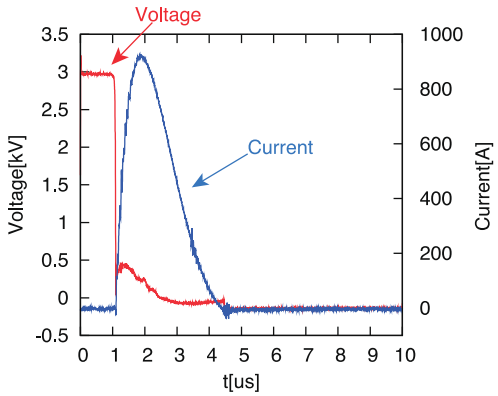

(b) Center electrode : negative

Fig. 5 Discharge voltage and current waveforms for operations with positive(a) and negative(b) polarities.

3. Results and Discussions

3.1 Discharge Voltage and Current Waveforms

Figure 5 shows typical waveforms of the discharge voltage and the current. When we compare the polarity effect on the waveforms, it is obvious that the spike of the discharge voltage waveform of negative is fewer than positive polarity. The results show that the current is slightly larger and the voltage during discharge is a little lower in case of negative polarity operation. That means, the plasma impedance is smaller when the device was operated with negative polarity.

3.2 Consumption Energy in the Whole Load

Figure 6 shows the dependence of consumed energy (i.e. the energy consumed in the electrode region) on the applied voltage. The vertical axis is the consumed energy in the load for one channel of the six channels and the horizontal axis is the charged voltage of the capacitor.

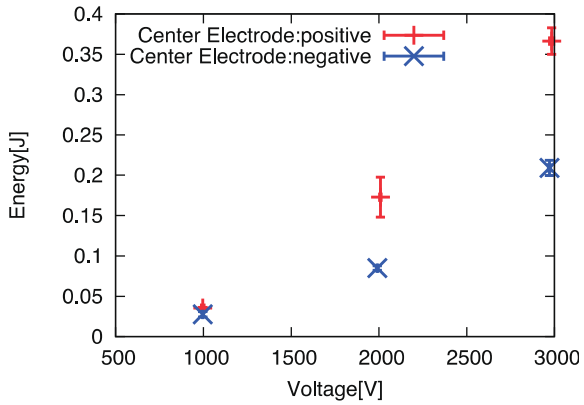

Fig. 6 Polarity dependence of consumption energy.

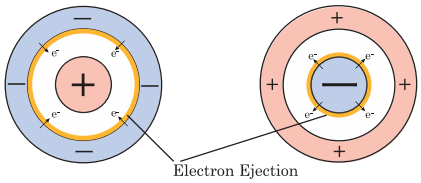

$$E \propto \frac{1}{r}$$

Fig. 7 Difference of initial plasma behavior between positive and negative polarity operations.

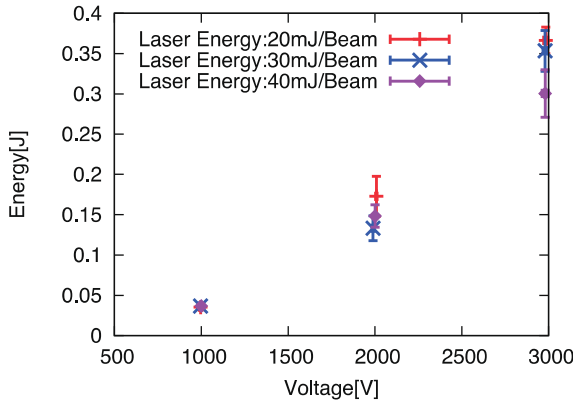

Fig. 8 Laser energy dependence of consumption energy.

According to Fig. 6, we know that the consumed energy in the discharge region is less than 10% of stored energy in the capacitor, and when the device is operated with negative polarity, the consumed energy is low in comparison with that of positive operation. The cause of this result is attributed to the voltage shown in Fig. 5, in which voltage during discharge is a little smaller in case of negative operation.

Figure 7 shows the difference in the strength of the electric field from which an electron receives energy for the discharge plasma. As illustrated in Fig. 7, in the coaxial geometry, electric field around the cathode is stronger and electrons are easily supplied when the center electrode is negative. As a result, the potential of the ion sheath is considered to become small and the load impedance decreases; i.e. the voltage during discharge decreases.

Figure 8 shows the laser energy dependence. In Fig. 8, although the difference is small, the consumption energy in the load tends to be small when the laser energy increased. As the amount of initial plasma increases by raising the laser energy, the number of careers increases. Consequently, the impedance of breakdown plasma is considered to decrease, and thereby energy consumption decreases.

4. Conclusions

In a counter-facing plasma focus device for EUV light source, the consumption energy of the whole load per one shot is measured as functions of the applied voltages, polarity and laser energy.

Results showed that, when the device was operated with negative polarity, the whole consumption energy was low in comparison with positive mode. This is likely to be attributed to the difference of the electric field strength from which electrons receive energy during the breakdown process. Moreover, the consumption energy tends to be a little smaller as the laser energy becomes large. This is likely to be due to enhancement of the number of careers by raising the

laser energy.

The results discussed in this report was just only the whole consumption energy in the discharge region. In order to optimize the operation and the electrode geometry, we have to evaluate hereafter where the energy is consumed and how the amount of energy depends on the operating parameter.

References

[1] G.E. Moore, Tech. Digest of IDEM 1975, pp.11-13 (1975).

[2] Majid Masnavi et al., "Estimation of optimum density and temperature for maximum efficiency of tin ions in Z discharge extreme ultraviolet sources", *Journal of Applied Physics,* **Vol.101**, No.3, pp. 033 306 1-9 (2007).

[3] BRANDT David C. et al., "LPP Source System Development for HVM", *Proc. Of SPIE,* **Vol.7**, 636, pp. 76 361 1-6 (2010).

[4] Y. Teramoto et al., "Dependence of Laser Parameter on Conversion Efficiency in High-Repetition Laser-Ablation-Discharge EUV Source", *Proc. Of SPIE,* **Vol.7**, 271, pp. 727 139 1-8 (2009).

[5] Yusuke Kuroda et al., "Counter-facing Plasma Guns for Efficient Extreme Ultra-Violet Plasma Light Source", *Seventh International Conference on Inertial Fusion Sciences and Applications (**IFSA2011**),* p. 5 (2013).

[6] Tatsuya Sodekoda et al., "Repetitive operation of counter-facing plasma focus device: toward a practical light source for EUV lithography", *Proc. of SPIE,* **Vol. 9048**, pp. 904824 1-8 (2014).

Plasma dynamics in counter-facing plasma-focus type extreme-ultraviolet light source

Kenta Kawaguchi, Tatsuya Sodekoda*, Hajime Kuwabara*, Masashi Masuda, Shi Jia Liu, Kouki Kanou, Mitsuo Nakajima, Tohru Kawamura, Kazuhiko Horioka

Department of Energy Sciences, Tokyo Institute of Technology, Yokohama 226-8502, Japan

**Research Laboratory, IHI Corporation, Shin-nakaharacho 1, Isogo-ku, Yokohama 235-8501, Japan*

ABSTRACT

We have developed a counter-facing plasma focus device for the next generation Li plasma light source of photo-lithography. The plasma dynamics in counter-facing plasma focus was discussed to optimize the operating condition. We obtained time-resolved spectra of the Li-plasma, which showed spectral purity evolves as a function of time. Based on the results, we estimated a current sheet profile and the total amount of Li mass that contributes the focusing plasma.

Keywords

EUV lithography, Plasma focus, Lithium emission, Spectroscopy, Plasma diagnosis

1. Introduction

Extreme-ultraviolet (EUV) lithography is eager to put it into practical use. For the practical application, we have to develop an efficient light source in wave-length region of 13.5nm ± 1% (in band).

A properly controlled plasma composed of hydrogenlilke Li has a strong line emission at 13.5 nm. Compared with other plasma source, it has some advantages for EUV light source such as little heating load from out-of-band emissions and less energetic debris [1]. To get a lot of 13.5 nm photon fluence, we have developed a new type of DPF type device [2, 3].

Figure 1 shows emissivity of the Lyman-α line originated in hydrogen-like Li ions. We used a collisional-radiative rate equation model for the calculation [4]. In the calculation, we assumed pure Li-plasma and neglected the effect of doubly excited states.

An expected spectral efficiency of in-band emissions (13.5 nm ± 1%) is shown in Fig. 2. In the calculation [5], emissivity of the Li plasma was estimated in a range from 9.5 nm to 124.0 nm.

As we see in Fig. 1 and Fig. 2, there are optimum operating conditions for the emissivity and the spectral efficiency. This means the purity and intensity of the line emission are provided basically by the plasma temperature and density which are determined by the plasma dynamics. If we can confine the plasma for more than μs, the high energy density plasma may realize an efficient and high average power EUV source [6]. In order to optimize the operating condition, it is important to know the Li plasma dynamics in the counter-facing plasma focus.

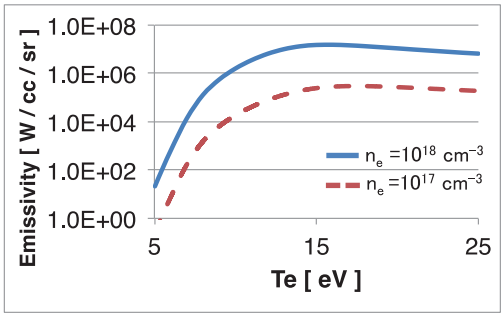

Fig. 1 In-band-emissivity of lithium Lyman-α line (13.5 nm ± 1%) vs. electron temperature Te.

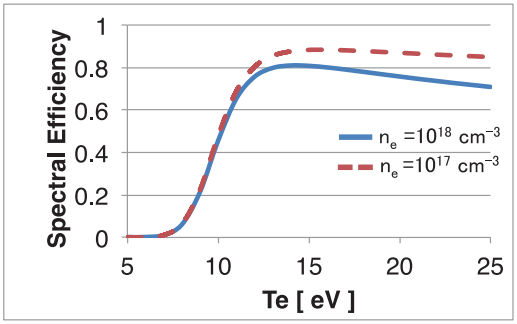

Fig. 2 Estimated spectral efficiency of Li-plasma as a function of electron temperature. Spectral efficiency of 13.5 nm ± 1% was calculated by integration of pure Li emissivity from 9.5 nm to 124.0 nm.

To know the plasma behavior, we tried time-resolved EUV optical emission spectroscopy (EUVOES) for the counter-facing plasma focus. From the evolution of spectra, we could estimate the amount of Li plasma and understand some plasma dynamics.

2. Experimental Setup

Figure 3 shows a schematic illustration of the counter-facing plasma focus device and the EUV spectrometer composed of a diffraction grating (HITACHI-No.001-0437) and a MCP (F2223-21P) which is controlled by a gate-driver circuit. The image of the MCP was recorded by a CCD camera. Figure 4 shows typical geometry of the focus electrodes.

First, initial plasma is made by Nd-YAG laser from solid Li at the root of the inner electrodes. The laser energyis about 20 mJ/beam/15ns. Second, a discharge between the inner and outer electrodes is triggered by the laser ablation. Third, the plasma sheet is accelerated in the direction of the center of the gap between the counter-facing electrodes. And then, the plasma begins to pinch, be thermalized, and emits the light in EUV region.

This spectrograph has sensitivity in a range from 12nm to 30nm. When the focus device was in operation, a high voltage from +5kV to +7kV was applied between the inner and outer electrodes, and a discharge was driven by 6 capacitors of 2.4 μF in total.

As shown in Fig. 3, there are 6 outer electrodes which have inductively isolated current paths.

The EUV spectrograph has temporal resolution of 200 ns with the fast gate driver using MOSFET.

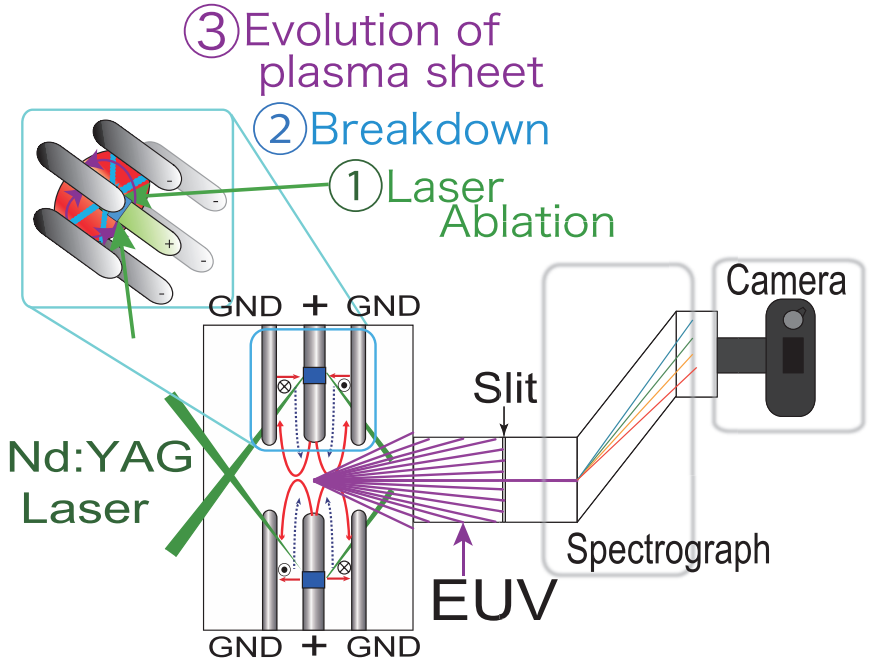

Fig. 3 Schematic of the discharging device and the EUV spectrograph by using diffraction grating plate and MCP controlled by driver circuit.

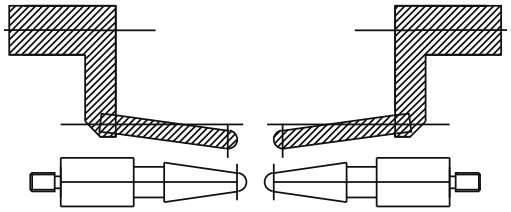

Fig. 4 Geometry of the electrodes

3. Results and Discussion

3.1 Characteristics of plasma focus phenomena

A time-integrated photograph of the plasma in the counter facing plasma focus device is shown in Fig. 5, where the device was operated with positive-positive mode. As we can see in Fig. 5, the pinch plasma was formed at the center of two electrodes. Strong green light at the roots of the electrodes was caused by the scattering of Nd-YAG (2ω) laser.

Figure 6 shows typical spectrum image of the EUV plasma. By converting the information on the pixels of the CCD camera into wavelength, we can obtain the spectrum intensity vs. wavelength.

Figure 7 shows typical discharge current profiles at the inner electrode, for operations with single focus mode and the counter-focusing mode. Here, $t = 0$ is defined at the laser trigger signal.

3.2 Results and Discussions

There was a difference in the current periods between counter-facing plasma focus and single plasma focus (see Fig.7). From a LCR circuit equation, we estimated that a difference of 0.2μs current period is caused by a difference of 2nH inductance of current path. The difference of inductance can be attributed to the evolution of plasma sheet. Figure 8 shows the evolution model of the current sheet in the single plasma focus mode.

On the other hand, Fig. 9 shows the expected current sheet behavior in the counter-facing plasma focus device.

As we show in Fig. 8 and in Fig. 9, the protrusion of current sheet in the counter-facing plasma focus seems to be suppressed. Therefore, a current period of the counter facing plasma focus becomes shorter than that of the single plasma focus because of smaller inductance.

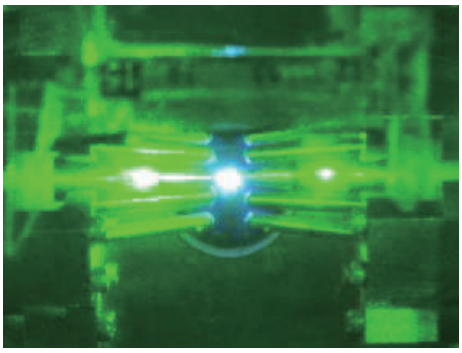

Fig.5 Time-integrated photograph of the plasma in counter-facing plasma focus.

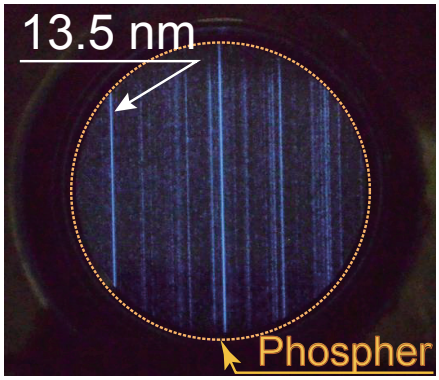

Fig. 6 Typical spectrum of Li plama.

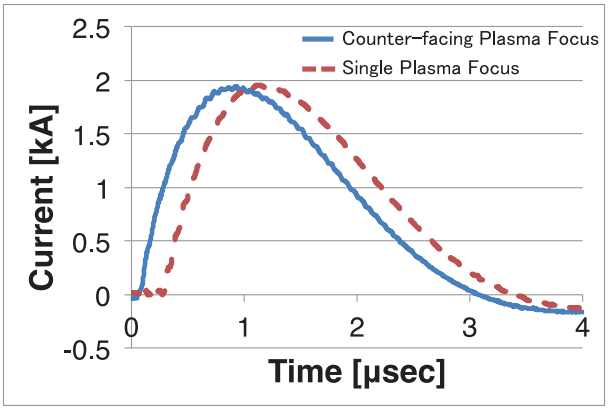

Fig.7 Typical current profiles. Solid line shows the current in counter facing plasma focus device and dotted line shows that in single plasma focus mode.

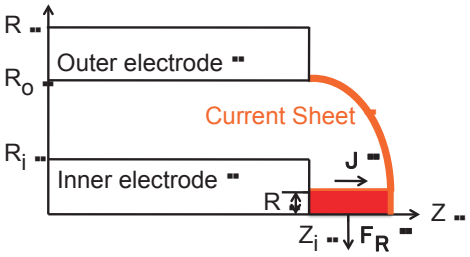

Fig. 8 Evolution of current sheet in single plasma focus mode.

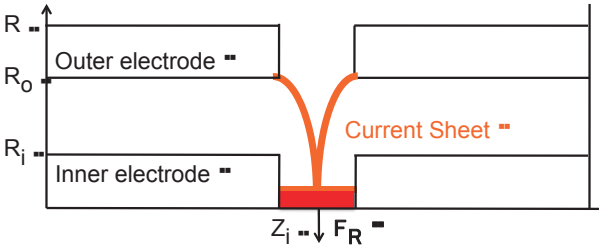

Fig. 9 Expected evolution of current sheet in counter-facing plasma focus device.

Figure 10 (a) - (e) show the results of time-resolved EUV optical emission spectroscopy. As shown in Fig. 10 (b), the 13.5nm line emission appears 800-1000ns after the laser trigger and that evolves to continuous spectra around 1800ns. This result suggests that the best condition for EUV light source is the beginning of the EUV emission from the point view of spectrum purity. At this moment, Li plasma may be strongly confined by the counter-facing current sheet and hold the temperature of electrons, at least, over 10eV.

As time goes by, the constraint force of self magnetic field seems to become insufficient to confine the plasma. Hence the plasma starts to diffuse and emit various spectral lines. Figure 10 revealed that the in-band EUV emission was maintained for ~1μs, which is almost 10 times longer than those of conventional plasma EUV light sources.

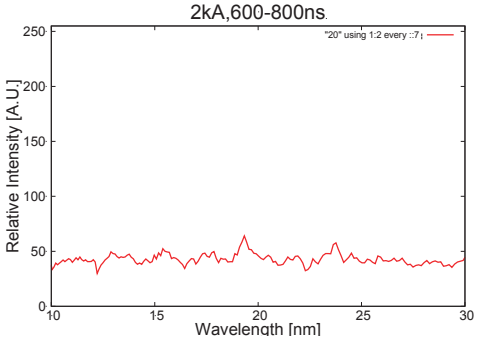

(a) t = 600-800 ns

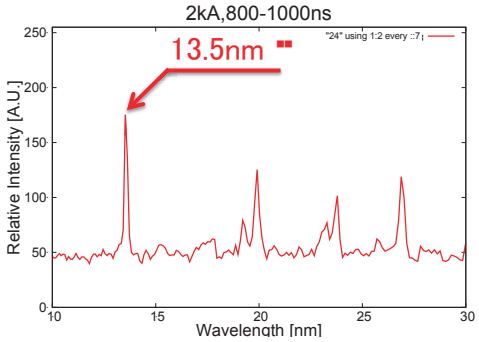

(b) t = 800-1000 ns

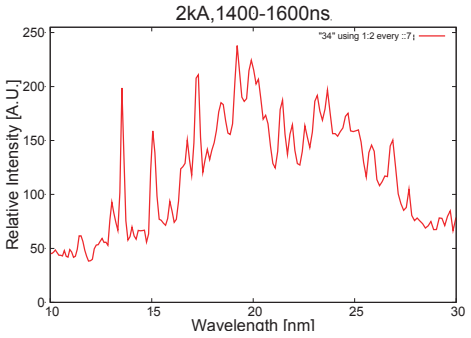

(d) t = 1400-1600 ns

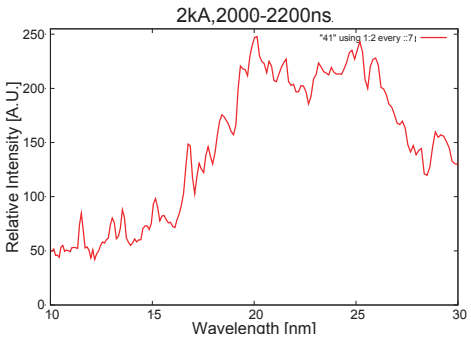

(e) t = 2000-2200 ns

Fig.10 Time-evolution of EUV spectra from counter-facing plasma.

Assuming 1-D equation of motion driven by electro-magnetic force and the plasma mass is constant, the displacement of the plasma z can be described by the equation below,

$$z = \iint \frac{1}{M_Z}\frac{\mu_0}{4\pi}\ln\left(\frac{R_0}{R_i}\right) I^2\, dtdt \qquad (1)$$

where M_z is the mass of plasma; μ_0 is the permeability; R_i and R_o are the radii of the inner and outer electrodes; and I is the single channel current through the plasma.

Figure 11 shows the plasma axial displacement estimated by the dynamics model of plasma focus and measured current profile I. As shown, the plasma arrives the center of gap between two electrodes, at least 800ns after the laser triggering (see Fig. 10). The distance between the laser spot and the center gap between two electrodes was about 18mm. So we can estimate the mass of the plasma which is confined is ~1.0ng for each current path. Therefore the total mass of the confined plasma was estimated to be ~12ng because the discharge plasma is driven by 12 channels.

If the plasma is closed in a sphere having 3mm diameter, the density of plasma is estimated to be ~10^{17}cm^{-3}, which is the best density from the view of spectral efficiency as shown in Fig.2.

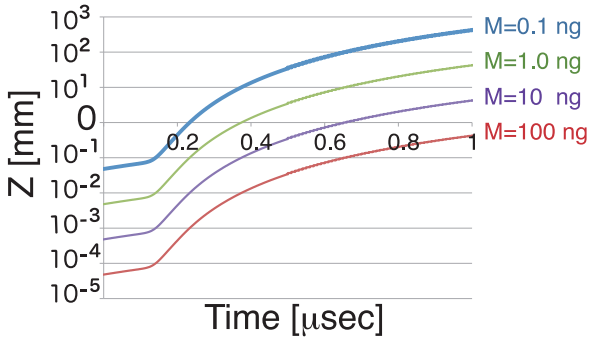

Fig. 11 Plasma axial displacement z estimated using 1-D dynamics model of plasma focus and measured current profile.

4. Concludung Remarks

We studied the plasma dynamics in the counter-facing plasma focus device. We got the current data and the time-resolved EUV OES data. We discussed the correlation between the plasma dynamics and the experimental results. Two issues were clarified from the results. One is the evolutions of the current sheet profile in the focus device. Another is the estimation of the amount of plasma closed in the center of gap between two electrodes. That is, the amount of plasma contributing the EUV emission.

What we should do next is estimating the evolution of electron temperature because we can know more detailed plasma dynamics if we do this. By that means, we can optimize the operating condition of the counter-facing device.

References

[1] Coons RW, Harilal SS, Campos D, Hassanein A, "Analysis of atomic and ion debris features of laser-produced Sn and Li plasmas", J Appl Phys 108(6):063306(2010).

[2] Y. Kuroda, K. Hayashi, H. Kuwabara, M. Nakajima, T. Kawamura, and K. Horioka. "Counter-facing plasma guns for efficient extreme ultra-violet plasma light source". In NIFS-PROC-90, (2012).

[3] H. Kuwabara, K. Hayashi, Y. Kuroda, H. Nose, K. Hotozuka, M. Nakajima, K. Horioka, "Counter-facing plasma focus system as an efficient and long-pulse EUV light source", Proc. SPIE 7969 (2011).

[4] T. Ozawa, S. Yamamura, N. Tatsumura, K. Horioka, and T. Kawamura, "Lasing of extreme ultraviolet light with nitrogen plasma in a recombining phase-Roles of doubly excited states", Phys. Plasmas **19**, 063302 (2012).

[5] T. Kawamura, K. Mima, F. Koike, "Line shapes of He beta including higher-order satellite lines for Ar ions in dense plasmas", Plasma Phys. Controlled Fusion **43**, 53 (2001).

[6] M. Masnavi, M. Nakajima, E. Hotta, K. Horioka, Appl, Phys.Lett., 89, 031503 (2006)

Decomposition of Formaldehyde Molecule in Water Solution by Irradiation of Pulsed, Intense Relativistic Electron Beam

Ryohei Myodo[1], Haruki Nakamura[1], Takashi Kikuchi[2], and Go Imada[1,3]

[1] *Department of Information and Electronics Engineering, Niigata Institute of Technology, 1719 Fujihashi, Kashiwazaki, Niigata 945-1195, Japan*

[2] *Department of Nuclear System Safety Engineering, Nagaoka University of Technology, 1603-1 Kamitomioka, Nagaoka, Niigata 940-2115, Japan*

[3] *Extreme Energy Density Research Institute, Nagaoka University of Technology, 1603-1 Kamitomioka, Nagaoka, Niigata 940-2115, Japan*

ABSTRACT

The formaldehyde in water solution has been successfully decomposed with irradiation of pulsed, intense relativistic electron beam. The concentration of formaldehyde decreases from 5000 ppm to 4000 ppm. It is found that the bremsstrahlung has little effects for the decomposition.

Keywords

Pulsed Intense Relativistic Electron Beam, Formaldehyde, Decomposition, Bremsstrahlung, Waste water

1. Introduction

Formaldehyde (CH_2O) is organic compound having pungent smell. It is used for an antiseptic, materials on organic synthesis, etc. in many factories. International Agency for Research on Cancer has been reported that the formaldehyde is carcinogenicity, and is harmful to a human body [1]. For this reason, the waste gas and/or water contained with formaldehyde must be treated, and be satisfied in WHO regulation even if the amount of formaldehyde is small [2]. Formaldehyde has been effectively treated with the chemical. In this treatment technique, however, the problem of waste water has arisen.

In this study, we propose a novel technique for deposition of formaldehyde in water solution by irradiating pulsed, intense relativistic electron beam (PIREB). The high energy electron has ability to decompose the formaldehyde molecule by elastic collision. The electron generates a hydroxyl radical (OH) if it reacts with water molecule (H_2O). The hydrogen atom in formaldehyde molecule is taken by the OH radical due to its strong oxidizing power. In addition, bremsstrahlung generated by the collision of PIREB with metallic materials may affect the decomposition.

In this paper, we demonstrate the decomposition of formaldehyde molecule by irradiation of the PIREB into the water solution. The decomposition of a small amount of formaldehyde will be anticipated due to the huge scale of electron shower.

2. Experimental Setup

2.1 PIREB Generator

Figure 1 shows schematic diagram of PIREB generator, “ETIGO-III” installed in Extreme Energy-Density Research Institute, Nagaoka University of Technology. It consists of a charger, capacitor, pulse transformer, pulse forming line, transmission lines, and induction acceleration cells of four stages [3]. The voltage pulse generated in the capacitor becomes high-voltage pulse of 670 kV with the pulse transformer and the pulse forming line. This high-voltage pulse is distributed to three magnetic cores installed in each acceleration cell. Each core operates as a 1:1 transformer, and is connected in

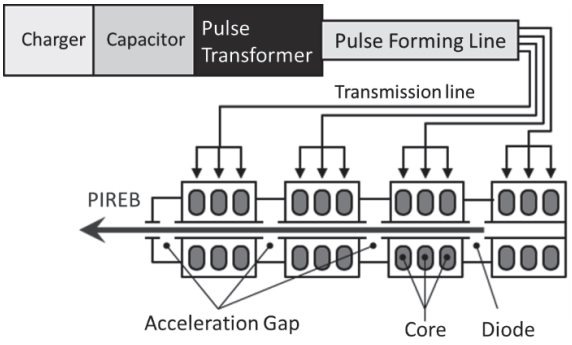

Fig. 1 Schematic diagram of PIREB generator "ETIGO-III".

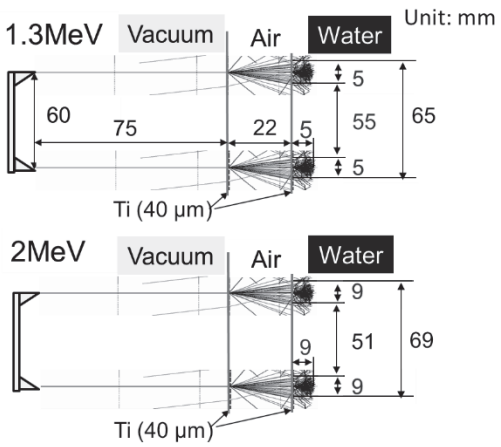

Fig. 2 Calculated trail of electrons in water.

series. In the acceleration cell, hence, the accelerating voltage of 2 MV (670 kV × 3) is obtained. If the electron-beam diode and acceleration gap are attached at the 1st acceleration cell and the other one respectively, the PIREB of 8 MeV, 5 kA, and 50 ns is generated. The peak kinetic energy of PIREB varies with the stages of acceleration cells as 2, 4, 6, and 8 MeV.

2.2 Decomposition chamber

Figure 2 shows the trail of 2-MeV electrons injected into the water. Since the average kinetic energy of PIREB is approximately two third of the accelerating voltage in ETIGO-III, the trail of 1.3-MeV electrons is also indicated. The behavior of electron is calculated by using CASINO ver. 2.48 software [4]. In the calculation, we assume that the electrons are emitted from a hollow anode with the diameter of 60 mm. It is found that the 1.3-MeV electrons penetrate into the water within 5 mm and spread over 5 mm.

Figure 3 shows the cross-sectional view of decomposition chamber. It is designed with the results mentioned in Fig. 2, and is made of acrylic resin. The chamber is separated from the vacuum part of ETIGO-III by the bulkhead (40-μm-Ti : 5-mm-air : 40-μm-Ti). The Rogowski coil is installed in the bulkhead to measure the PIREB current. The PIREB generated and accelerated at ETIGO-III propagates through the bulkhead, and then is irradiated into the distilled water contained 5000 ppm of formaldehyde.

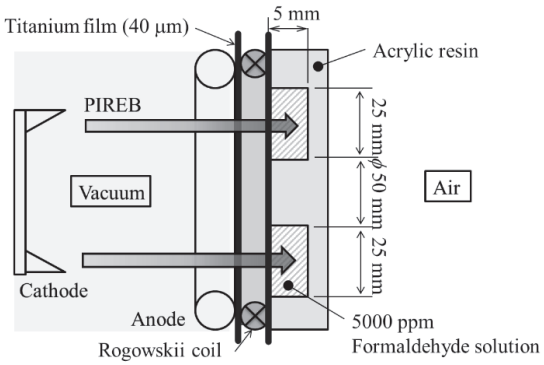

Fig. 3 Cross-sectional view of decomposition chamber.

The depth, inner and outer diameters of water vessel are 5 mm, 50 mm$^{\phi}$, and 100 mm$^{\phi}$, respectively. The volume of water is calculated to be 29.5 cm^3.

2.3 Measurement of formaldehyde

The concentration formaldehyde in the water solution is measured by using absorption spectrophotometry technique. The formaldehyde reacts with chromotropic acid diluted in acid solution to form a violet dye [5]. In this experiment, NANOCOLOR Formaldehyde 8 and PF-12 (MACHEREY-NAGEL GmbH & Co. KG) are used as a reagent and a filtered photometer, respectively. The measuring wavelengths of the photometer are 345, 436, 470, 540, 585, 620, and 690 nm with ±2 mm accuracy.

3. Results and Discussion

3.1 Acceleration voltage and current of PIREB.

Figure 4 shows the typical acceleration voltage of PIREB (V_a) at each acceleration cell in ETIGO-III. Here, V_a is measured from the current which flows a branch resistor connected with the acceleration gap in parallel. It is found that the peak voltage reaches 2 MV in each cell, and the pulse width is 70 ns (FWHM). Since the average kinetic energy of PIREB (E) is approximately two third of V_a, we obtain the PIREB of E = 1.3, 2.8, and 4.3 MeV.

Figure 5 shows the typical current of PIREB (I_0) irradiated into the water solution. The peak current ranges from 1000 to 1500 A. The PIREB slightly decreases in current with its propagating into drift tube between the acceleration gaps.

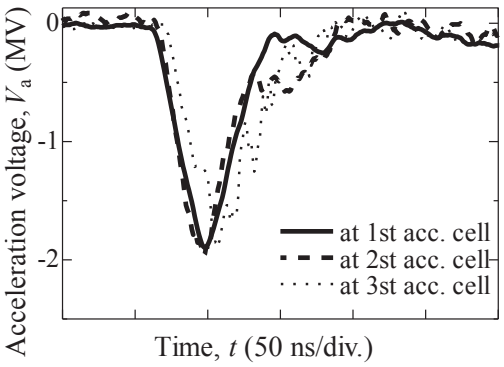

Fig. 4 Typical acceleration voltage of PIREB at each acceleration cell.

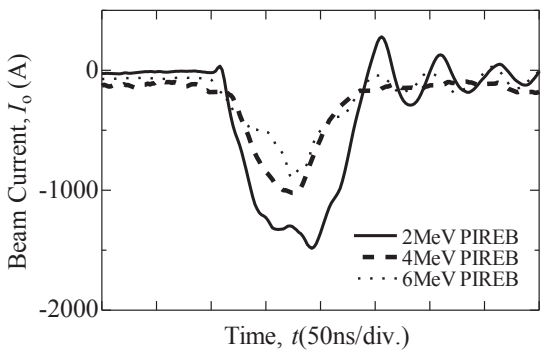

Fig. 5 Typical current of PIREB irradiated into water solution.

3.2 Decomposition of formaldehyde

Figure 6 shows the concentration (H) and amount (m_0) of formaldehyde in the water solution as a function of the total number of PIREB irradiation (N). It is found that H decreases from 5000 to 4000 ppm by the PIREB having 2-MeV peak energy. At 4- and 6-MeV peak-energy PIREB, H also decreases to 4600 and 4200 ppm, respectively. From these results, we confirmed the decomposition of formaldehyde by irradiation of PIREB.

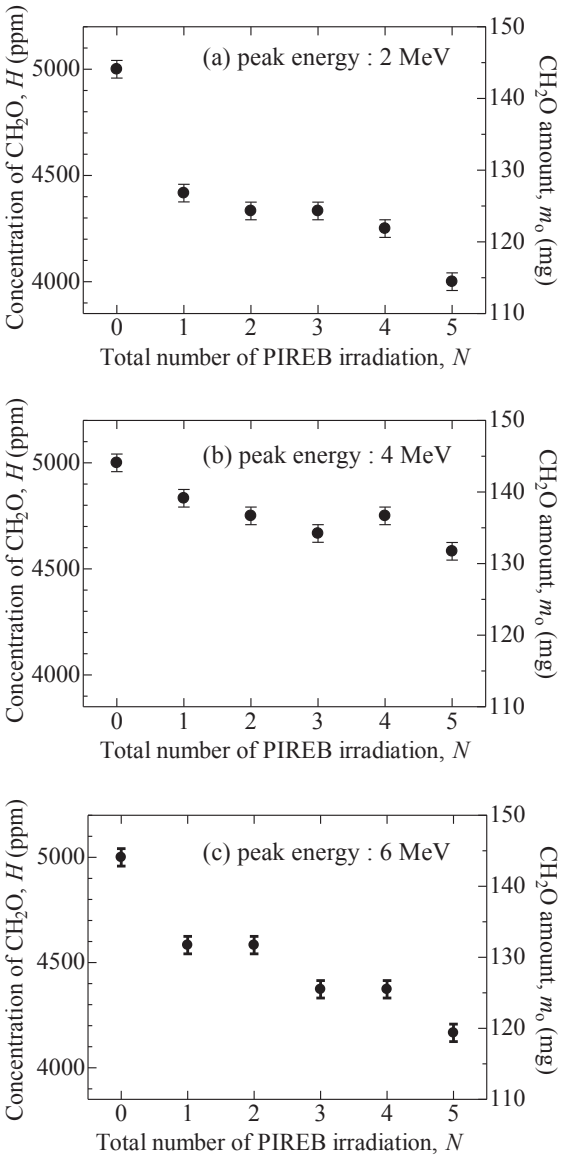

Fig. 6 Concentration and content of formaldehyde in water solution as a function of total number of PIREB irradiation.

Table 1 Decomposition energy efficiency.

Peak energy	Stack of cells n	Number of PIREB irradiation N	Injected energy W (kWh)	Decomposed amount m (mg)	Decomposition efficiency η (g/kWh)
2 MeV	1			29.4	137
4 MeV	2	5	4.3×10^{-5}	12.3	29
6 MeV	3			23.5	36

The decomposition energy efficiency (η) is summarized in Table 1. Here, η is estimated from the following equation.

$$\eta = \frac{m}{WNn} \quad (1)$$

where, m is the amount of formaldehyde decomposed, W is the injected electric energy into each acceleration cell, n is the stack of acceleration cells. Since the high energy electron tends to pass through a medium without interaction, the efficiency decreases with increasing the electron energy. In high energy electron, on the other hand, the intensity of bremsstrahlung increases. Figure 7 shows the radiation yield of titanium caused by electron impact. The radiation yield is calculated by using ESTAR software [6]. The titanium foils are used in the decomposition chamber as the bulkhead between vacuum and water. The yield nearly tripled on the electron energy going from 2 to 6 MeV. However, the decomposed amount of formaldehyde at 6-MeV electron is small compared with that at 2-MeV electron. In this experimental setup, the bremsstrahlung has little effects for the decomposition.

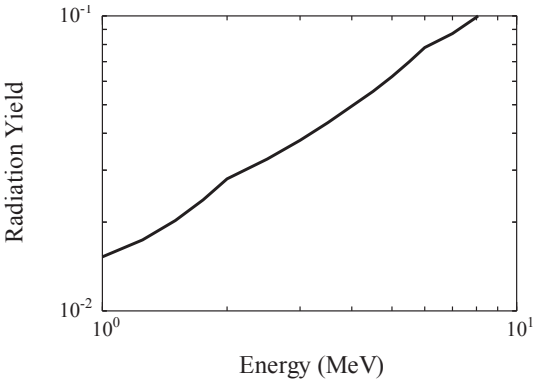

Fig. 7 Radiation yield of titanium caused by electron impact.

4. Conclusion

The formaldehyde in water solution has been successfully decomposed with irradiation of pulsed, intense relativistic electron beam. The concentration of formaldehyde decreases from 5000 ppm to 4000 ppm.

Acknowledgement

The authors wish to acknowledge the support on experiments from all the members of ETIGO-III team.

References

[1] IARC, "Chemical Agents and Related Occupations - A Review of Human Carcinogens -", IARC Monographs on Evaluation of Carcinogenic Risks to Humans, **100F**, pp. 401-435 (2012).
[2] WHO, "Formaldehyde", Concise Int'l Chem. Assessment Doc., 40 (2002).
[3] A. Tokuchi, *et. al*, "Development of High Energy Induction Accelerator, "ETIGO-III"", Proc. 12th Int'l Conf. on High-Power Particle Beams, pp. 175-178 (1998).
[4] http://www.gel.usherbrooke.ca/casino/index.html
[5] http://www.mn-net.com/tabid/4702/Default.aspx
[6] http://www.nist.gov/pml/data/star/index.cfm

Influence of Metal Target on the Evolution of Laser Supported Detonation Waves

Ken Yonezawa, Mitsuo Nakajima, and Kazuhiko Horioka

Department of Energy Sciences, Interdisciplinary Graduate School of Science and Engineering, Tokyo Institute of Technology, 4259 Nagatsuta, Midori-ku, Yokohama 226-8502, Japan

ABSTRACT

Laser induced-phenomena were studied using a TEA（Transversely Excited Atmospheric pressure）CO_2 laser which was focused onto a metal target in an ambient gas of N_2 (0.5 atm – 2.0 atm) or He (1.0 atm) . Evolutions of the laser-absorption region and the laser-induced shock waves were observed by a fast framing camera and a shadowgraph method. Results showed that the laser induced phenomena evolve as a laser supported detonation. Results also indicated that the metal target plays an important role both for the formation of laser plasma and the acceleration of the laser-induced shock waves.

Keywords

Laser induced plasma, Shock waves, Laser supported detonation wave, Fast electron

1. Introduction

Processes using laser-induced breakdown plasma have already been used in wide ranges of industrial and scientific fields. However effects of target material on the breakdown process and the evolution of laser-induced shock wave were not clarified yet.

A scheme based on vapor assisted breakdown model has been advocated conventionally, in which the laser breakdown is induced by an ablation plasma made from contaminated materials on the metal surface [1, 2]. A schematic illustration of the conventional scheme of the breakdown is shown in Fig. 1. As shown, in the first stage, a metal surface is heated until the adsorbing impurities on the target surface and/or on the defects are vaporized. In the second stage, the conditions are led for ignition of an initial plasma in the vapor-gas mixture close to the laser irradiated area. Then, this initial plasma evolves to a dense plasma and induces a shock wave into the surrounding vapor and gas.

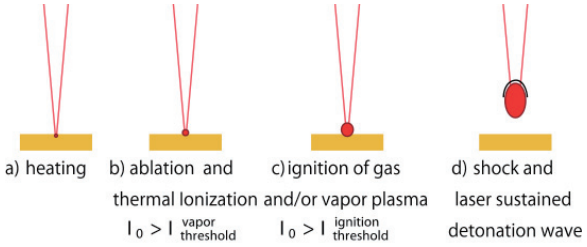

Fig. 1 Vapor-initiated laser breakdown mechanism.

The shock heated region is able to absorb the forthcoming laser radiation and evolves rapidly to a fully developed plasma which strengthen the shock wave, and vice versa; that is to say, the formation of Laser Supported Detonation (LSD) wave.

The intensity threshold to initiate a breakdown is based on the criterion $\Gamma_+ > \Gamma_-$, where Γ_+ is the rate of electron energy increase and Γ_- is .the rate of energy losses. Assuming that the average energy of electrons is $\Delta/3$, the criterion can be transformed as follows [3], where Δ is the ionization potential of neutral particles

$$I_i > 2\times10^3 \frac{\Delta}{\lambda^2 M} \quad (\mathrm{MW\ cm^{-2}}) \qquad (1)$$

with Δ in eV, λ in μm and M (amu) the atomic mass.

For our case of CO_2 laser (λ=10.6μm) irradiation, Eq. (1) can be written as follows,

$$I_i \geq 18 \frac{\Delta}{M} \quad (\mathrm{MW\ cm^{-2}}) . \qquad (2)$$

On the other hand, according to a recent laser breakdown experiment [4], in spite of CO_2 laser (1.5 J, 1μs) irradiation on a target under ambient gas of He (1 atm), any spectral compositions of target material

were not observed. This result indicates that the ignition of laser breakdown is not induced by the ablation of target material. However, when we consider that work functions of metallic materials are ~ eV, it hardly occurs to make electrons by direct photoemissions from the target surface by the CO_2 laser (10.6 μm).

In this study, we discuss the laser induced phenomena such as laser supported detonation waves specifically on the influence of metal target during the laser induced breakdown processes.

2. Experimental Setup

A schematic of our experimental setup is shown in Fig. 2. A Transversely Excited Atmospheric (TEA) CO_2 laser (USHIO Electric UNIMARK400, 2.0-2.6 J, 10.6 μm, 1 μs) induced a breakdown plasma in a test chamber. The test chamber has six windows with diameter of ϕ 62 mm. A typical waveform of the laser intensity is shown in Fig. 3. As shown, the laser formed a μsec pulse with a sharp peak at initial phase of full width at half maximum (FWHM) of 120 ns. The laser beam with 20 mm×30 mm cross-section was focused through a ZnSe window on the center of the test chamber to a spot of ϕ 0.5 mm.

A vacuum pump was capable of evacuation down to 10^{-1} Torr. A part of the laser beam was split in the direction of a pyro detector (GENTEC-EO INC. QS-H3) and recorded the intensity of laser pulse.

The laser energy was monitored with a joule meter

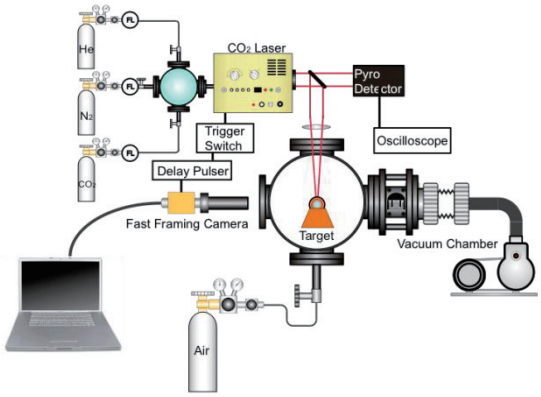

Fig. 2 Schematic of experimental set-up.

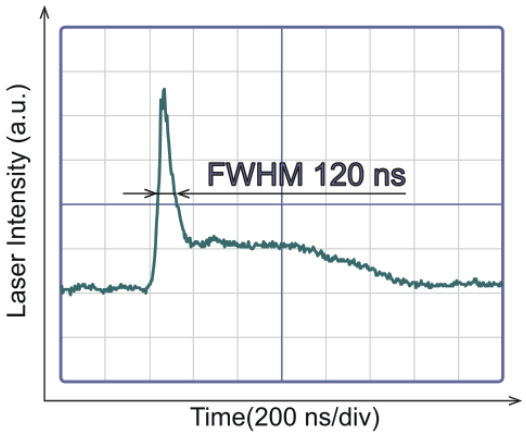

Fig. 3 Typical waveform of CO_2 laser power.

(SCIENTECH INC.-MODEL PHD50).

A conical target made of brass with a rounded top with ϕ 1 mm diameter was placed in the test chamber. We observed a laser plasma and a laser-induced shockwave by fast framing cameras (NAC Image Technology ULTRA-Neo and HAMAMATSU, A1976-01) and a shadowgraph system with He-Ne laser (632.8 nm, 75mW). Visible images of the laser induced plasma were observed by using the camera with exposure time of 50 ns. A charge-coupled device (CCD) camera recorded the image through a band pass filter (632.8 nm). The shutter timing and the exposure time (10ns) were controlled using a delay pulsar (Stanford Research, DG645).

3. Results and Discussion

At first, to investigate the target influence, we compared temporal-spatial evolutions of light emitting region of the laser-produced plasma and the shock waves with and without the solid target.

3.1 Behaviors of plasmas and shock waves in N_2 atmosphere with and without solid target

We focused on the role of solid target for the breakdown and the evolution of laser induced phenomena. By observing the evolution of laser plasma and the shock waves around the solid target with the fast framing cameras, we compared the behaviors of laser induced phenomena with and without the solid target.

First of all, we compared the laser-induced plasma behavior in atmospheric N2 under room temperature with and without the solid target. Typical results observed by the high-speed framing camera are shown as a function of time from the laser injection in Fig. 4 and Fig. 5, where the exposure time of the high-speed camera was 50 ns.

As shown in Fig.4 and Fig.5, at around 600nsec from the laser injection, the plasma is divided to two parts. As also shown with these photos, we confirmed that the laser plasma moves to the upstream, that is, the direction to the laser injection.

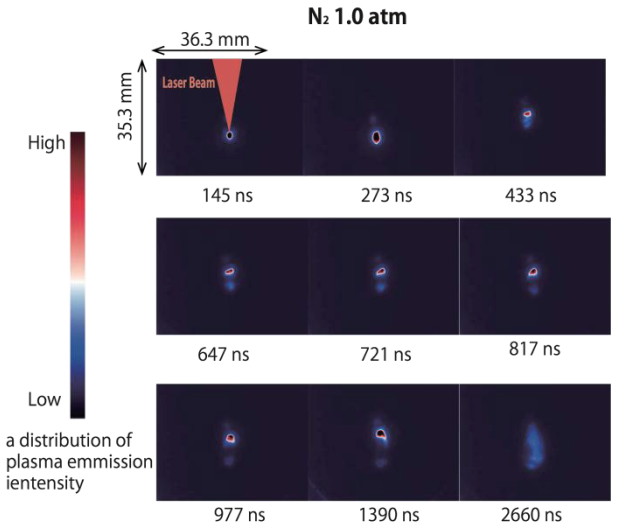

Fig. 4 Evolution of laser-induced plasma in N_2 without solid target gas.

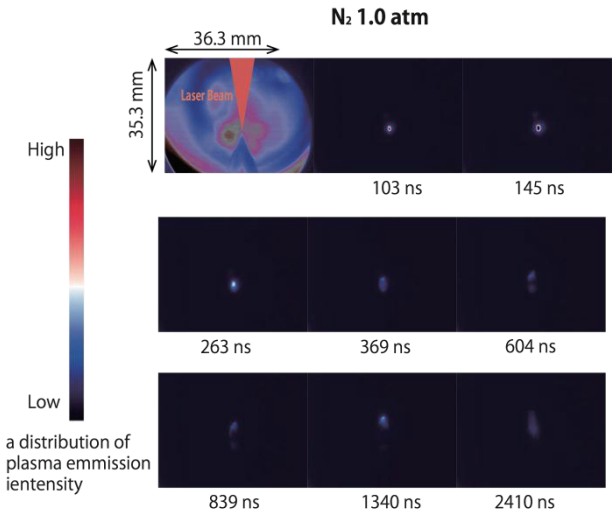

Fig. 5 Behavior of laser breakdown plasma in N_2 gas with solid target.

The behavior can be explained by the development of absorption region of laser energy, namely the region corresponding to the critical density of plasma moves to the upstream according to the plasma evolution and/or the shock wave propagation. Results also show that the plasma moves much faster when we make the laser breakdown plasma with solid target.

Next, temporal-spatial evolutions of the shock wave were investigated by the shadowgraph with exposure time of 10nsec. The results are shown in Fig. 6 and Fig. 7. As is well known, the expansion of laser induced plasma drives a shock wave in the ambient gas. Hence the history of laser plasma

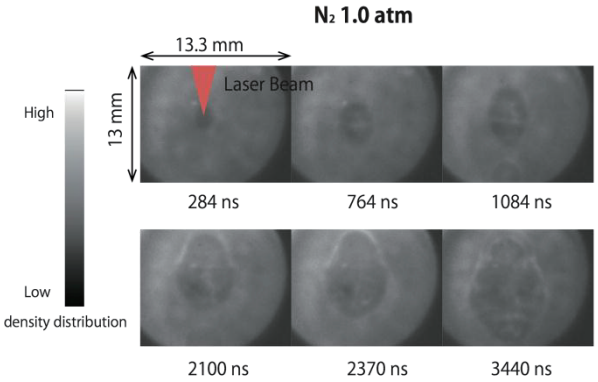

Fig. 6 Beavior of laser-induced shock wave in N_2 gas without target.

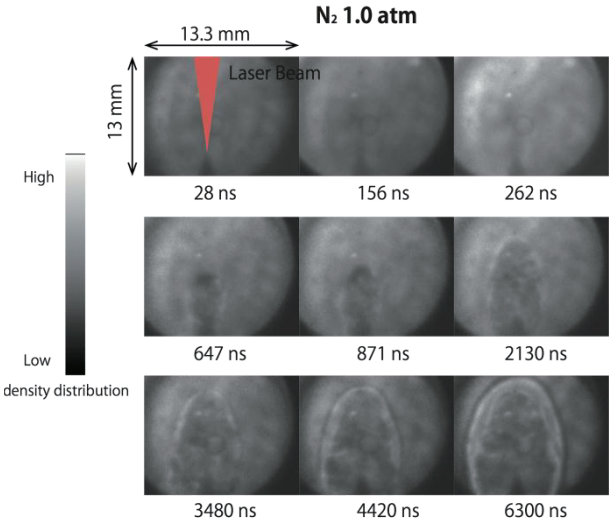

Fig. 7 Behavior of laser-induced shock wave in N_2 gas with solid target.

evolution is considered to be reflected in the behavior of shock waves.

As we can see from the shadow images, the shock waves driven by the laser plasma are corresponding to the behaviors of laser plasma shown in Fig.4 and Fig.5. As shown, the shapes of shock waves were always elliptic regardless of experimental conditions.

All of the results showed that regardless of the experimental conditions, the CO2-laser induced plasma evolves accompanied by a shock wave with elliptic shape. These results indicate that, in all of our experimental conditions, the shock induced plasma works as a trigger for the breakdown and this strengthen the shock wave; namely the phenomena evolve as the laser supported detonation.

In order to discuss the role of solid target on the evolution of laser-induced phenomena, we plotted places of the visible fronts of laser plasmas and those of shock waves as a function of time. Results for laser-breakdown in N2 gas are shown in Fig. 8. In the figure, we plotted the brightest position of the plasma front and compared them with the shock front.

The clearest difference shown in the figures is the progress speed between in the cases with solid target (upper figure) and without it (lower figure). As the upper figure shows, the speed of the plasma emission at around 100 ns from the laser irradiation was almost ~ 10^4 m/s. On the other hand, that is ~10^3 m/s without target. The results indicate that there is a mechanism which enhances the propagation of laser interaction region to the upstream of laser irradiation.

3.2 Pressure dependence of the behaviors of plasmas and shock waves in N_2 gas

We investigated the effects of ambient gas (N2) pressure on the behaviors of laser-induced plasma and the shock wave. Figure 9 shows the results, where the laser output energy was 2J.

As shown in the figures, the evolutions of plasma region and the shock front slightly depended on the ambient pressure. We also observed that when we decreased the ambient pressure, the plasma emission region moved faster than the shock wave. Conventional schemes of laser supported detonation are based on mechanisms ablation assisted

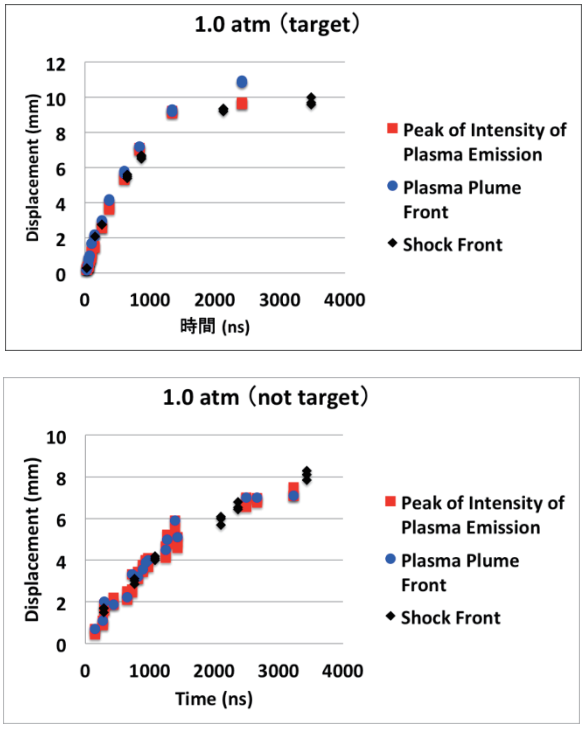

Fig. 8 Speeds of front propagation of laser-induced plasmas and shock waves in N_2 gas with and without solid target.

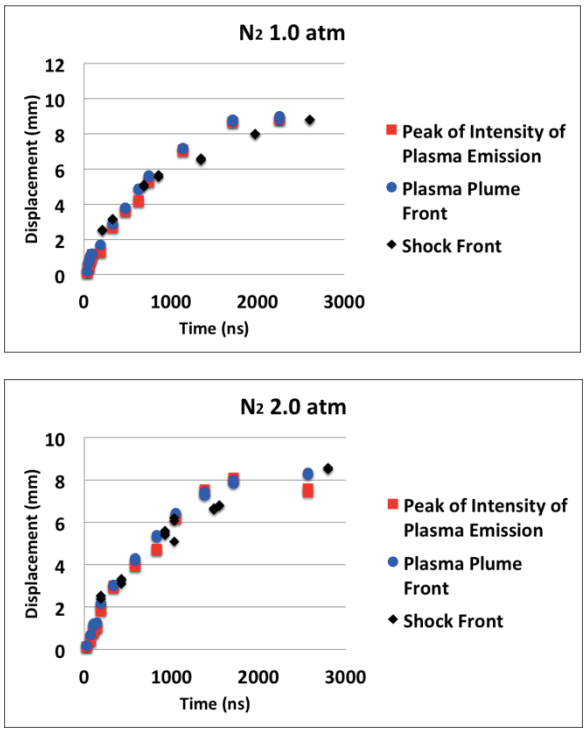

Fig. 9 Pressure dependences of propagation speed of plasma evolutions and shock waves in N_2 gas with solid target.

breakdown and detonation wave induced by the shock heated plasma [3]. However, this result indicates that, a mechanism that accelerates the laser absorption region other than the shock heated layer, plays some roles in the case of laser induced breakdown process with solid target.

3.3 Behaviors of laser induced plasmas and shock waves in He gas

In order to investigate gas species effects on the plasma evolution, we filled the test chamber with He gas of 1atm, where the other experimental conditions were fixed. Figure 10 shows the framing images of plasma evolution induced by the CO2 laser injection. A comparison of those images with Fig.5 shows that,

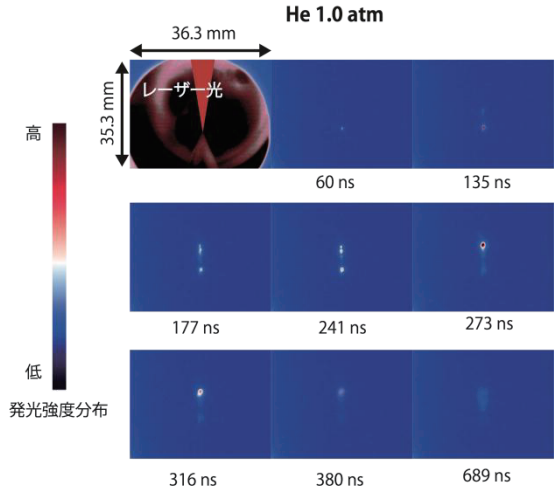

Fig. 10 Evolution of laser-induced plasma in He gas .

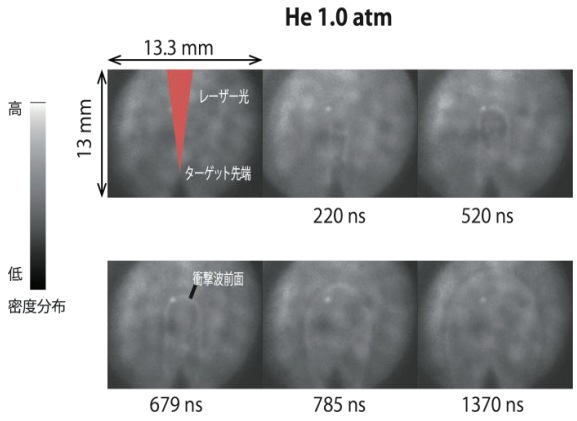

Fig. 11 Behavior of laser induced shock wave in He atmosphere.

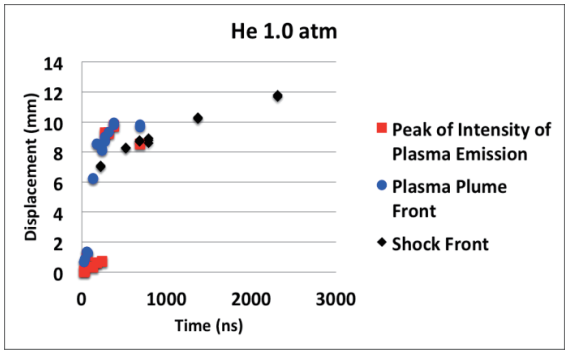

Fig. 12 Evolutions of laser plasma front and shock waves in He atmosphere.

in the early phase of laser injection, the laser plasma was clearly divided to two parts and the plasma front in He moved much faster than that in N2 gas.

On the other hand, when an insulator is set at the same place instead of the metal target, the front part of emission zone was not observed. From these facts, we concluded that the emission zone was formed by the fast electrons emitted from the target.

Evolutions of laser induced shock wave are shown in Fig.11. As shown the shapes of the shock waves are more elliptic than those in N2 gas, particularly at the early phase of laser interaction; 200-700nsec from the laser injection. The shape of elliptical shock wave is due to the fast move of the laser absorption region.

Figure 12 shows evolutions of the front of laser plasma and that of shock wave. From the figure, we can see that the plasma front moves faster than that of shock wave at the early phase of laser injection.

The quantitative differences of behaviors in N2 and in He gas are probably due to smaller cross section of electron-He atom compared with that of N2 molecule. Also the results indicate that fast electrons formed from the metal target in the breakdown phase play an important role for the laser induced phenomena.

4. Conclusions

We studied laser induced breakdown phenomena in an ambient gas (N2 or He) and a solid conical target using a TEA CO2 laser with μsec pulse duration. In particular, our efforts were focused on the study on

effects of solid target for the laser breakdown phenomena.

Results obtained in this study are summarized as follows;

1. The laser-induced plasma evolved always with an elliptic shock wave; namely it evolved as a laser supported detonation.
2. The speed of plasma evolution was enhanced almost order of magnitude by placing a solid (metal) target (with target) at focusing region and that depended on the gas species.
3. The propagation speed was ~ 10^4 m/sec. That cannot be explained with conventional laser detonation schemes in which an ablated material from the target induces laser breakdown and the laser plasma evolves with an assist of shock wave propagation.
4. All of the results obtained in this study, indicated that fast electrons produced during the breakdown phase plays an important role for the enhanced propagation of laser induced plasma.

Acknowledgements

We would like to express our appreciation to Mr. S.Someya and Mr.S.Matsumura of NAC Image Technology for help with the fast framing photography. Our thanks are also given to Mr. K.Kawaguchi for his interest on this study.

References

[1] C.Boulmer-Leborgne, J. Hermann, and B. Dubreuil, "Plasma formation resulting from the interaction of a laser beam with a solid metal target in an ambient gas", Plasma Sources Science and Technology, **2**(3), p.219 (1993).

[2] Y. P. Raizer, Soviet Phys. , JETP 21, 1009 (1965)

[3] J. Hermann, C., I. Mihailescu, B. Dubreuil. "Multistage plasma initiation process by pulsed CO2 laser irradiation of a Ti sample in an ambient gas (He, Ar, or N2)", Journal of Applied Physics, **73**(3), pp.1091–1099, (1993).

[4]M.Ramli, N.Idris, K.Fukumoto, H.Niki, F.Sakan, T.Maruyama, K.H.Kurniawan, T.J.Lie, and K. Kagawa. "Hydrogen analysis in solid samples by utilizing He metastable atoms induced by TEA CO2 laser plasma in He gas at 1 atm", Spectrochimica Acta Part B, Atomic Spectroscopy, **62**(12):1379 – 1389, (2007). A Collection of Papers Presented at the 4th International Conference on Laser Induced Plasma Spectroscopy and Applications (LIBS 2006).

Smith-Purcell Radiation of Oversized Backward Wave Oscillator

Kazuo Ogura, Kiyoyuki Yambe, Takayuki Iwasaki, Shota Magori, Junpei Kojima, Akihiko Kojima and Fumiaki Kawabe

Niigata University

ABSTRACT

Smith-Purcell (SP) radiations of oversized K-band backward wave oscillator (BWO) are examined. By injecting an annular beam in the weakly relativistic region less than 100 kV, a beam mode with harmonic number n = 1 excites BWO radiations based on the TM_{01} surface wave. The same beam mode excites higher order modes leading to SP radiations in the U- and E-bands. For a beam mode with n = 2, SP radiations are in the F- and D-bands, up to about 100 GHz, which is about four times higher than the frequency of the TM_{01} surface wave. The SP radiation in the U-band can be enhanced by using a self-bunching of K-band BWO.

Keywords

Oversized backward wave oscillator, Surface wave, Smith-Purcell radiation, Cherenkov interaction, Slow cyclotron interaction, Weakly relativistic electron beam

1. Introduction

Tunable and compact electromagnetic (EM) wave sources of about 1 GHz to above 100 GHz at moderate or high power levels (dozens kW to MW level) are in demand for widespread applications including plasma heating, plasma diagnostics, telecommunication systems and radar systems[(1)]. Moreover, applications for THz radiation have been growing in various fields such as biology, food, agriculture and medicine. Since EM wave sources utilizing electron beam are able to realize relatively high-power operations, they attract attentions and are extensively studied from GHz to THz wave regions. Beam kinetic energy is transferred to EM wave energy through wave-particle interactions. Typical interactions are cyclotron interaction in the fast-wave region and the Cherenkov interaction in the slow-wave region. Corresponding microwave sources are gyrotron for the former and backward wave oscillator (BWO) and traveling wave tube (TWT).

BWO and TWT are slow-wave devices driven by an axially streaming electron beam without an initial perpendicular velocity. These slow-wave devices use the slow-wave structure (SWS) to reduce the phase velocity of EM wave to the beam velocity. In principle, sizes of SWS become too small to be fabricated in the millimeter or terahertz wave region. Moreover, the EM wave is concentrated on the SWS wall. Electron beams should propagate inside the spread of such a surface wave to insure a strong beam coupling. The interaction space of surface wave may be too narrow for beam to propagate in the sub-millimeter or terahertz wave region.

To increase the frequency, the higher order mode operation may be considered. Utilization of higher order mode is also seen in the fast wave device, i.e., gyrotron and is a common solution for high frequency devices driven by electron beams. As for the Cherenkov device based on the higher order mode, there is Smith-Purcell free electron laser (SP-FEL) from millimeter wave to visible light regions. Original SP-FEL is based on spontaneous emission and the radiation intensity is essentially weak[(2)]. Recently, enhanced SP radiations by using the short pulsed bunching of the relativistic electron beam in MeV region was reported[(3)]. This is a kind of the super-radiance by a relativistic electron beam with a bunch length shorter than wavelength of radiating

field.

Another kind of enhanced SP radiation was realized by using a weakly relativistic electron beam less than 100 kV[4]. The grating of SP-FEL has a surface wave and the beam is bunched via the surface interaction. And self-bunched beam causes the stimulated SP emission[5]. This SP-FEL uses no accelerator for beam bunching and is a feasible candidate for a compact desktop THz wave source.

The surface wave interaction may result in a BWO or TWT operation depending on the group velocity. To increase the frequency and power handling capability, oversized SWSs have been successfully used. The diameter of the oversized SWS is larger than the wavelength of the output EM wave. In the oversized SWS, SP radiations due to the higher order modes may coexist with the BWO radiation based on the surface wave[6]. In this work, SP radiations of oversized BWO driven by a weakly relativistic electron beam are examined.

2. Oversized SWS

Periodic corrugation is widely used for BWOs. Typical corrugations have sinusoidal and rectangular shapes. Other shapes of corrugation such as semicircle and trapezoid may also be used. Although many shapes of corrugation are conceivable, important parameters are amplitude h_0 and periodic length z_0. The corrugation wave number k_0 is defined as $k_0 = 2\pi/z_0$. Typical values of h_0 and z_0, as well as the SWS diameters in BWO experiments of Niigata University are listed in Table 1. Values of D/λ are about 1 for the X-band and larger than 1 for the K- and Q-bands. Moreover, the frequency of the surface wave increases up to G-band, for which D/λ becomes a very large value of about 18.

Table 1. Corrugation parameters of X-, K-, Q- and G-band oversize slow wave structure.

Band	D [mm]	z_0 [mm]	h [mm]	λ [mm]	D/λ
X	28.9	8.0	4.45	30	1.0
K	31.4	3.0	1.7	11.8	2.7
Q	30.0	2.0	1.0	7.5	4.0
G	30.0	0.5	0.3	1.7	18

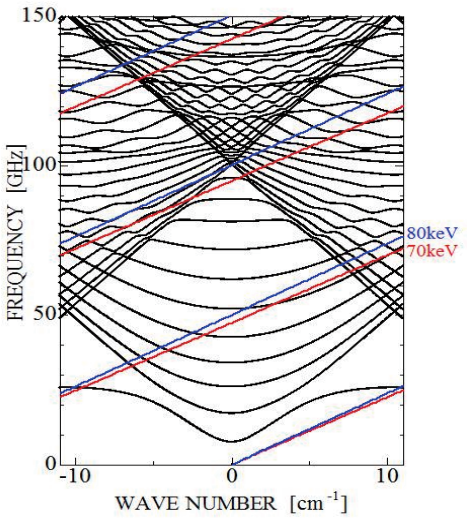

Fig. 1. Dispersion curves of the oversized K-band SWS and beam lines $\omega = k_n v_0$ with 80 kV and 70 kV.

EM fields in the SWS are expressed by a sum of spatial harmonics in accordance with the Floqut's theorem.

$$\boldsymbol{E}(r,\theta,z,t) = \left[\sum_{n=-\infty}^{\infty} \boldsymbol{A}_n(r)\right] \exp\left[\mathrm{i}\left(k_z z + m\theta - \omega t\right)\right] \quad (1)$$

Here, m is the azimuthal mode number, k_z is the axial wave number and ω is the angular frequency, $k_n = k_z + nk_0$ and $\boldsymbol{A}_n(r) = \boldsymbol{E}_n(r)\exp\left[\mathrm{i}\left(k_n z\right)\right]$ is the nth Floqut's harmonic.

The dispersion curves of EM field are periodic in the k_z-space with period k_0. Similar periodic dispersion can be seen in the band theory of solid state physics based on the Bloch's theorem. The periodic dispersions can be displayed in three schemes, i.e., reduced zone, periodic zone and extended zone schemes. Note that they represent the same dispersion. And we use suitable schemes for analyzing phenomena.

Dispersion curves of oversized K-band SWS are shown in Fig. 1, which is a reduced zone scheme from $k_z = -k_0/2$ to $k_z = k_0/2$. The lowest mode is TM_{01}, which is a surface wave in the slow-wave region and has an upper cutoff frequency of about 25 GHz at $k_z = \pm k_0/2$. The higher order modes are TM_{02}, TM_{03},

TM_{04} … and complicated higher order modes composed of the multiple spatial harmonics of TM. The higher order modes are in the fast-wave regions. The lower cutoff of TM_{02} is lower than the upper cutoff of TM_{01} resulting in overlapping of modes. Beam modes with velocity v_0 are expressed by $\omega = k_n v_0$ with any integers n. The n-value of $\omega = k_n v_0$ does not change for the period of $k_z = -k_0/2$to $k_0/2$ in the reduced zone scheme of Fig. 1. Near $k_z z_0 = \pi$, BWO operation occurs attributed to the Cherenkov interaction between TM_{01} and beam mode with $n = 1$.

Figure 2 shows the dispersion curves of oversized G-band SWS. The upper cutoff frequency of fundamental TM_{01} mode is mainly determined by z_0 and h_0 and about 170 GHz with the parameters of Table 1. And the higher order modes are mainly determined by z_0, which is about 1/6 of K-band. Hence, the frequency region of higher mode becomes about 6 times higher than that of K-band. Many

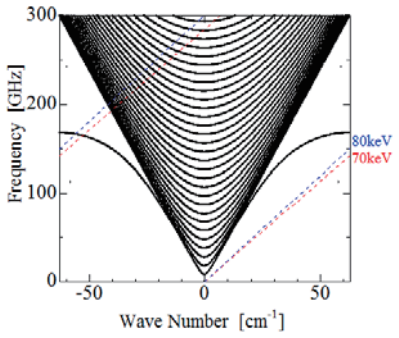

Fig. 2. Dispersion curves of the oversized G-band SWS and beam lines $\omega = k_n v_0$ with 80 kV and 70 kV.

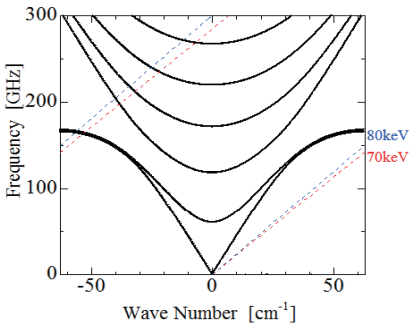

Fig. 3. Dispersion curves of the oversized G-band coaxial BWO and beam lines $\omega = k_n v_0$ with 80 kV and 70 kV.

higher order modes exist in the oversized G-band SWS of Fig. 2. Figure 3 shows dispersion curves of oversized G-band coaxial SWS. The outer corrugation of Fig. 2 is used. The inner corrugation has the diameter of 25.2 mm and the same z_0 and h_0 as Fig. 2. The inner conductor reduces drastically the higher order modes. Generally, the inner conductor generates the fundamental transverse EM (TEM) mode. When the inner conductor is corrugated like Fig. 3, the TEM mode becomes a TM dominant surface wave of the inner corrugation and is referred to as the cylindrical surface wave (CSW)[7]. The CSW is mainly determined by z_0 and h_0 like the TM_{01} surface wave. Upper cutoff frequency of CSW is lower than but very close to that of the TM_{01} surface wave.

3. Surface Wave Excitation and SP Radiation

Surface wave excitation and SP radiation in oversized BWO are schematically shown in Figs. 4(a) and (b), respectively. When the slow-wave interaction in Fig. 4(a) is the Cherenkov interaction in the Compton regime, it is a three wave interaction and includes the fast and slow space charge waves and the surface wave. The excited surface wave clings to the corrugation surface. Some of the surface wave is reflected back at the corrugation ends and the other goes out of corrugation. The reflected surface waves form an axial mode for a strong BWO operation[8]. In Fig. 4(b), the Cherenkov interaction includes the slow space charge wave and the higher order mode and is a two wave process.

The two mechanisms coexist in the periodic slow-wave device as pointed out in the pioneering work of the Ledatron[6]. In the Ledatron, the two mechanisms are controlled by using a Fabry-Perot resonator. Recent experiments on SP-FEL reveal that the two mechanisms are closely related with each other[4,5]. Sufficient bunching of beam by the interaction with the surface wave is essential to the stimulated SP emission.

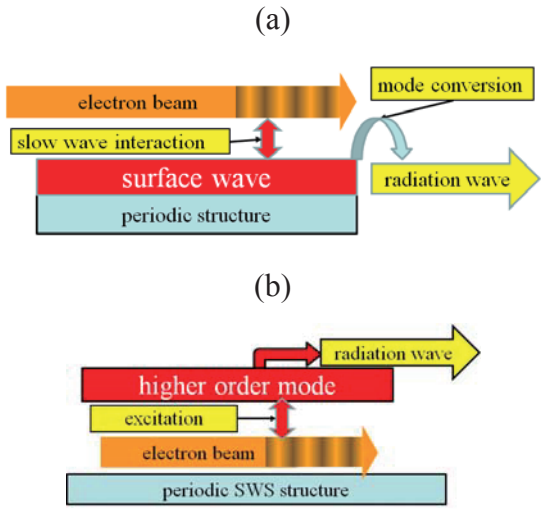

Fig. 4. Beam interactions with (a) surface wave and (b) higher order modes.

4. Oversize BWO Experiment

We study weakly relativistic oversized BWOs in X-, K- and Q-bands with hollow SWS[9,10]. They are driven by an annular electron beam with energy less than 100 keV. Diameters of SWS are about 30 mm as listed in Table 1 and parameters of injected beam are almost the same among these BWOs. Radiation powers are up to about 5 MW, 500 kW and 200 kW for X-, K- and Q-bands, respectively. The quality factor Pf^2 of our weakly relativistic BWO is about 3.5×10^5 [kW·GHz^2] as shown in Fig. 5.

Recently, performance of G-band BWO was also examined with an annular electron beam in a weakly relativistic region less than 100 kV. The radiation power level is estimated to be in some kW- some 10 kW level and the quality factor is the same as $Pf^2 = 3.5\times10^5$ [kW·GHz^2] obtained from the X-band to Q-band as shown in Fig. 5.

5. SP-radiation of oversize BWO

Typical signals from oversized K-band BWO including higher order mode radiations are shown in Fig. 6. The K-band signal is attributed to BWO operation of the K-band surface wave and its frequency is estimated to be about 26 GHz by the time of flight method. SP radiations above the K-band are detected from U-band to H-band systems. Higher order mode radiations are confirmed up to

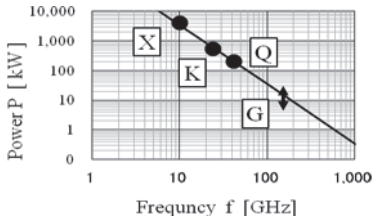

Fig. 5. Output versus frequency of weakly relativistic oversized BWO.

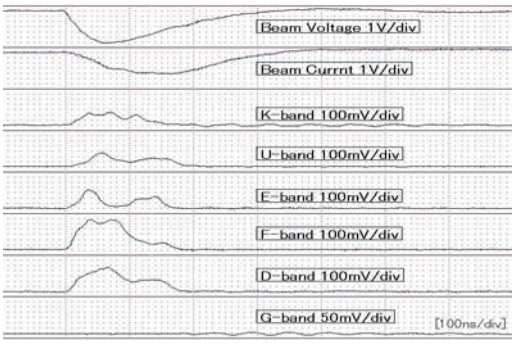

Fig. 6. Waveforms of measured signal. The beam voltage and current have the peak values of about 80kV and 300A, respectively.

around 100 GHz and no signal above G-band is detected.

Is it possible to control the SP-radian? The answer is "Yes". To demonstrate a controlled SP-radiation, the bunching section is separated from oversized BWO. The bunching section is composed of coaxial SWS with an inner corrugation and is placed upstream from oversized BWO. A beam is injected near the inner corrugation of bunching section. The beam is far away from the wall of oversized BWO. In

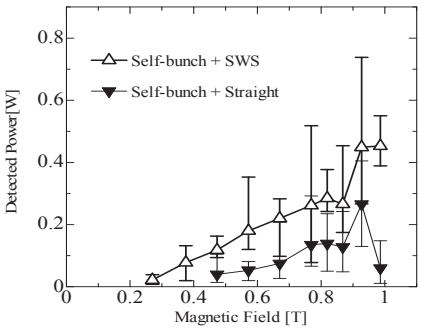

Fig. 7. Peak value of the U-band signal versus magnetic field with the ϕ20 mm cathode.

other words, the beam radius is too small to interact with the surface wave of oversized BWO. The self-bunched beam by the bunching section goes into oversized BWOs. SP radiations of oversized BWO are enhanced in U-band by several times as shown in Fig. 7.

6. Discussions and Conclusions

The larger distance between the beam and the oversized BWO wall is preferable for high power beam propagation without damage on the corrugation. However, the beam should propagate within the interaction region of the surface wave for oversized BWO operation. This is true for the SP-FEL in unbounded configuration. It seems commonly accepted concept that the interaction region of higher order modes is the same as that of the surface wave. The beam should propagate within the interaction region of surface wave to ensure enough beam coupling with EM waves in oversized BWO and SP-FEL. On the contrary, our experiments demonstrate that a strong SP radiation can also be obtained by a beam propagating outside the surface interaction region, if the beam is self-bunched. More definite studies of bunching section will be required to optimize the enhanced SP radiations of oversized BWO.

In conclusion, SP radiations of oversized K-band BWO are examined by injecting an annular beam in the weakly relativistic region less than 100 kV. The beam excites BWO radiations based on the TM_{01} surface wave. It also excites higher order modes leading to SP radiations in the U- and E-bands with n = 1 and SP radiations in the F- and D-bands with n = 2. The SP-radiations observed is up to about 100 GHz which is about four times higher than the frequency of the TM_{01} surface wave.

The SP radiations can be enhanced by using a self-bunching configuration, which allows us to set the beam radius independently from the radius of oversized BWO. Strong SP radiation by the self-bunched beam is unique and may be of considerable interest for development of high-power SP-FEL using intense electron beams.

References

[1] J. N. BENFORD et al., "High Power Microwaves, second edition, (Taylor & Francis, New York, 2007).

[2] S.J. SMITH et al., "Visible Light from Localized Surface Charges Moving across a Grating", *Phys. Rev.* **92**, p.1069 (1953).

[3] S.E.KORBLY et al., "Observation of Frequency-Locked Coherent Terahertz Smith-Purcell Radiation", *Phys. Rev. Lett.* **94**, 054803 (2005).

[4] J. URATA et al., "Superradiant Smith-Purcell Emission", *Phy.Rev. Lett.* **80**, 3, pp.516-519 (1998).

[5] H. L. ANDREWS et al., "Observation of THz Evanescent Waves in a Smith-Purcell Free-Electron Laser", *Phys. Rev. ST Accel. Beams* **12**, 080703 (2009)

[6] K. MIZUNO et al., "Two Different Mode Interactions in an Electron Tube with a Fabry-Perot Resonator-The Ledatron", *IEEE Trans. Electron Devices*, **20**, 8, pp.749-752 (1973).

[7] K. OGURA et al., "Normal Modes and Slow-Wave Instabilities in Oversized Coaxial Slow-Wave Structure with Rectangular Corrugations", *IEEE Trans. Plasma Sci*., **41**, 10, pp.2729-2734 (2013).

[8] K. OGURA et al., "Study on Oscillation Starting Condition of K-Band Oversized Backward Wave Oscillator Driven by a Weakly Relativistic Electron Beam", *J. Plasma Fusion Res. SERIES*, **6**, pp.703-706 (2004).

[9] K. Tanaka: "Theoretical and Experimental Studies on Nonaxisymmetric Mode Radiation from X-Band High Power Backward Wave Oscillator", PhD thesis, Niigata University (1999).

[10] S. Aoyama et al., "Improved Performance of Oversized Backward Wave Oscillator Driven by Weakly Relativistic Electron Beam", Trans. Fusion Sci. Tech. **51**, 204 (2007).

Experimental Study on an Intense Free Electron Maser using Bragg Resonators

Tomoaki Ogawa, Takuma Asami, Takahiro Yamaguchi, Momoko Katsuoka, Ryusuke Kiyomoto, Yukihiro Soga, Keiichi Kamada, and Naum S. Ginzburg*

Graduate School of Science and Technology, Kanazawa University, Kanazawa, Ishikawa, 920-1192, Japan

**Institute of Applied Physics, Russian Academy of Sciences, Nizhny Novgorod, 603600, Russia*

ABSTRACT

A Bragg resonator was used to increase the frequency selectivity of an intense free electron maser powered by an intense relativistic electron beam. An electron beam with energy of around 770 keV, current of 200 A and pulse duration of 150 ns was injected into the cylindrical tube immersed in a guide and a helical wiggler magnetic field. A 40 GHz Bragg resonator with two traditional Bragg mirrors was set inside the cylindrical tube. The microwave with frequency of nearly 40 GHz was observed as expected using a 100 m dispersive line and a band pass filter only when the beam propagates through the wiggler field. However, when the Bragg resonator was inserted and the wiggler field was applied, the microwave with frequency of 45 GHz was observed by a reflection grating. Unexpected coupling resulted in the higher frequency radiation. The experiment is continued in future.

Keywords

electron beam, microwave source, Bragg resonator, FEM, IREB

1. Introduction

An electron tube using a pulsed mildly relativistic electron beam (REB) is expected to realize an intense THz source. One of the candidates of THz source among electron tubes is a free electron maser (FEM). An intense mildly relativistic electron beam (REB) with energy of ~ 1 MeV and output power of 1 GW is used for an energy source of an intense FEM. One of the problems for the intense FEM to be solved is the wide frequency spectrum of the radiation. A normal Bragg resonator is utilized to make the radiated frequency spectrum narrower. Two traditional Bragg reflectors work as mirrors in the optical distributed feedback LASER [1-5]. But the traditional Bragg reflector loses the selective features over transverse indexes, as the radiated frequency increases. An advanced Bragg reflector was proposed by Ginzburg [6]. The dispersion curves of a traditional and an advanced reflectors are shown in Fig. 1. While a traditional Bragg reflector uses the interaction between forward and backward wave of TE_{11} mode, an advanced Bragg reflector utilizes the interaction between a propagating wave and a quasi-cutoff mode to provide a higher selectivity over the transverse index than a traditional Bragg reflector. Structural difference between the traditional and the advanced reflectors is mainly on the periodic length of the corrugation. While the corrugated period length of a traditional Bragg reflector is a half of the wavelength, that of an advanced Bragg reflector is

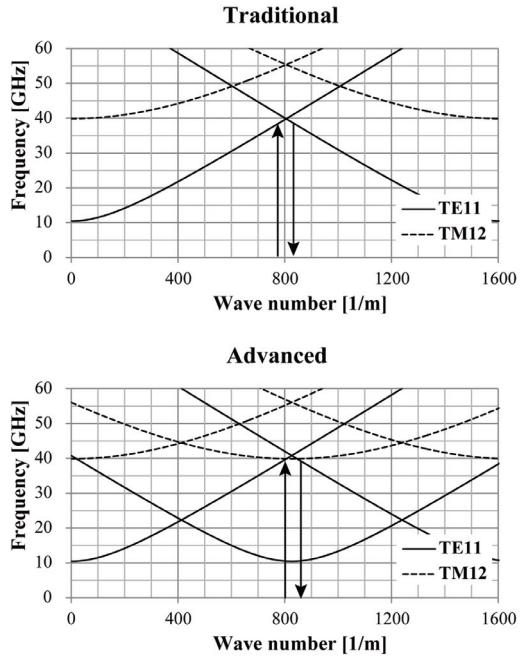

Fig. 1 Dispersion curves. Upper: a traditional Bragg reflector. Lower: an advanced Bragg reflector.

nearly equal to it. Two traditional Bragg reflectors are used at the entrance side and the exit side of the normal Bragg resonator. In the hybrid Bragg resonator, an advanced Bragg reflector is used at the entrance side and at the exit side the traditional Bragg reflector is utilized.

2. Experimental Apparatus

Figure 2 shows the experimental setup. An intense relativistic electron beam (IREB) with energy of around 770keV and current of around 200 A was injected through an annular anode with diameter of 8 mm into the drift tube with diameter of 17 mm. Axial magnet field (Bg) with strength of up to 1T was applied by a solenoid coil. The IREB was diverged to the wall at the exit of the axial magnetic field. A helical wiggler coil [7] located inside the solenoid coils provided a periodic radial magnetic field (Bh) up to 0.18 T.

The location of the Bragg reflectors is both side of the helical wiggler coil. The period of corrugation for a traditional Bragg reflector can be determined by

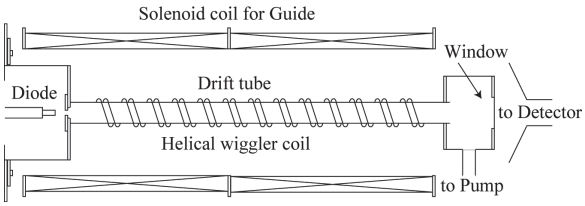

Fig. 2 Experimental setup

the relation $k_g=k_b/2$, where k_g is the wave number for 40 GHz, TE_{11} mode of the circular waveguide and k_b is that of the corrugation period. To determine the depth of the corrugation and the length of the reflectors, we use the simulation code CST MW studio and also we use the simulation to determine the parameters of an advanced Bragg reflector. The parameters of both Bragg reflectors are summarized on Table 1 [7].

Table 1 Parameters of traditional and advanced Bragg reflectors

	Traditional	Advanced
Mean Radius [mm]	8.4	8.4
Mode	TE_{11}	TE_{11}⇆TE_{12}
Frequency [GHz]	39.8	39.8
Center Frequency [GHz]	±0.5	±0.05
Corrugation Period [mm]	3.9	7.6
Corrugation Depth [mm]	0.25	0.1
Corrugation Length [mm]	250	200

The cold tests of both Bragg reflectors were carried out [7]. The network analyzer E8354C (Agilent Technology) was utilized as shown in Fig. 3 (upper). The transmitted spectra as shown in Fig. 3 (lower) were obtained. While the frequency of 39.6 ±0.5 GHz was reflected with the traditional Bragg reflector, that of 39.85±0.05 GHz was reflected with the advanced Bragg reflector as shown in Fig. 4. The advanced Bragg reflector could be expected to

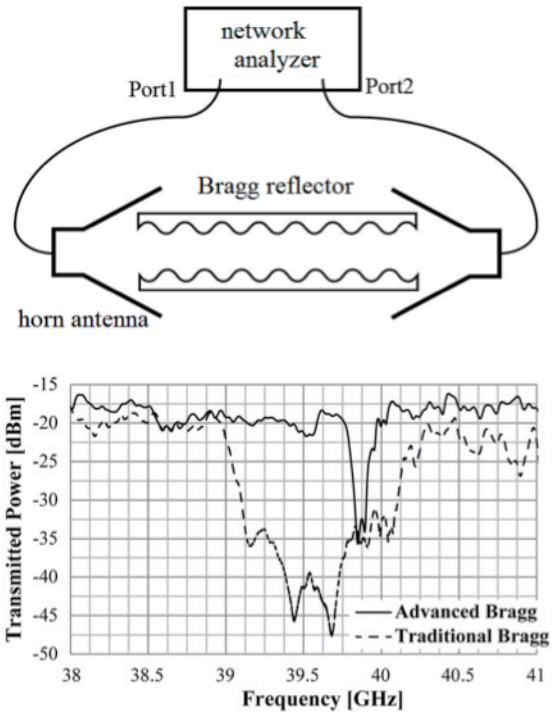

Fig. 3 Upper : Microwave is radiated from the port 1 and the transmitted microwave is detected by port 2. Lower : Waveforms of the tranmitted microwave.

obtain higher frequency selectivity. About the cold test of Bragg resonators, while several peaks observed with frequency range of about 39.6±0.5 GHz using the normal Bragg resonator, a single peak was obtained with the width about 39.85±0.05 GHz using the hybrid Bragg resonator. The appropriate length between the reflectors remained to be solved.

A damage pattern on a brass plate inserted from the downstream side of the waveguide showed the circular shape of beam cross section with diameter of 8 mm.

A horn antenna was set just behind the acrylic window to observe the radiated microwave. The frequency spectrum of the radiated microwave was observed by a 100 m dispersive line, a 3 band (26.5-31.5 GHz, 30.7-35.7 GHz , 35.5-40 GHz) filter bank and a diffraction grating system for 30-50 GHz.

3. Experimental Results and Discussions

We used the dispersive line to observe the overall frequency spectrum of the radiation. The waveforms of the microwave detected at the entrance and the exit of the 100 m dispersive line are shown in Fig. 4. The diode voltage is also depicted. The calculated frequency in Fig. 4 is not accurate because the correspondence between the signals detected at the entrance and the exit cannot be clear. The waveforms of the microwave detected at the entrance of the dispersive line show the difference with and

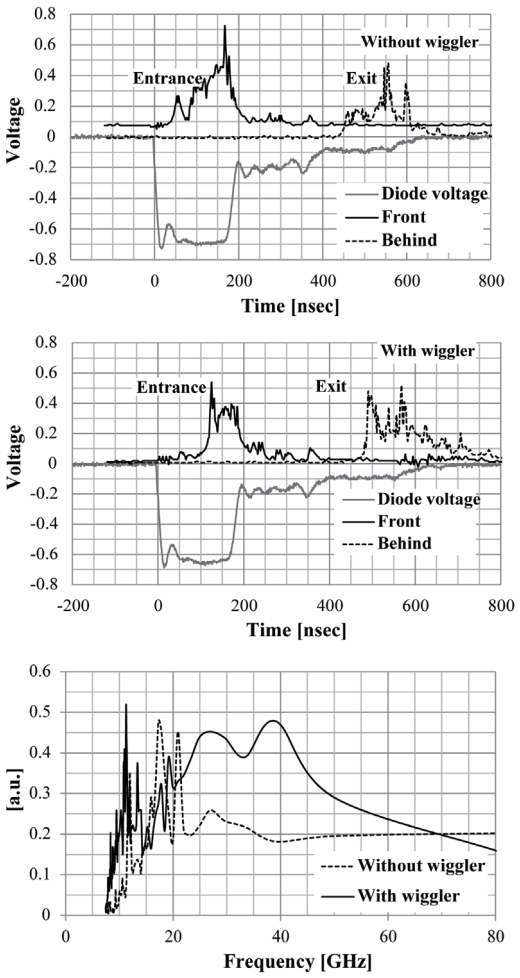

Fig. 4 Diode voltage and microwave waveforms of the dispersive line without (upper) and with (center) wiggler magnetic field. Roughly calculated frequency spectra (lower).

without the wiggler magnetic field. The signals below 25 GHz were suspected to be the interaction between the beam cyclotron mode and the waveguide mode. The frequency near the 40 GHz was observed only when the wiggler field was applied.

With the filter bank, the microwave with frequency 33.3-40 GHz was observed only when the wiggler field was applied as shown in Fig. 5.

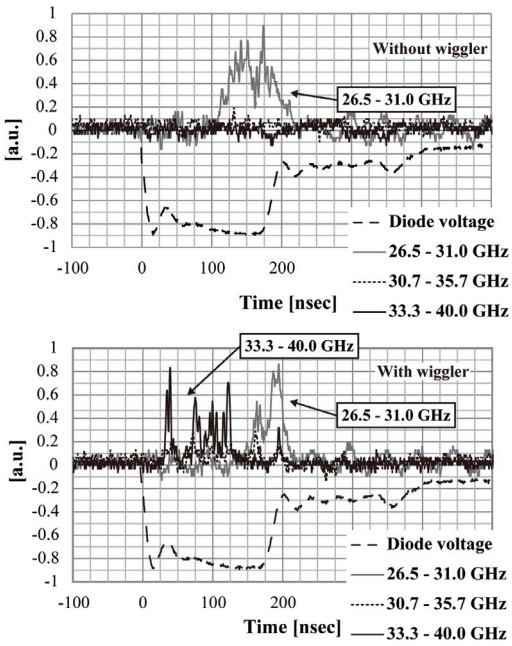

Fig. 5 Diode voltage and microwave waveforms of the filter bank without (upper) and with (lower) wiggler magnetic field.

The radiation with frequency of around 40 GHz was observed only with the wiggler magnetic field in the experiments as described above. However, when the diffraction grating was used, the difference of the radiation between with and without the wiggler field is not clear as shown in Fig. 6. The radiation was observed with frequency of roughly around 39 - 45 GHz with and without the wiggler field.

It was not clear the difference among the experimental results with three observation systems.

When the traditional Bragg resonator was inserted, the radiation with frequency of 44 GHz showed

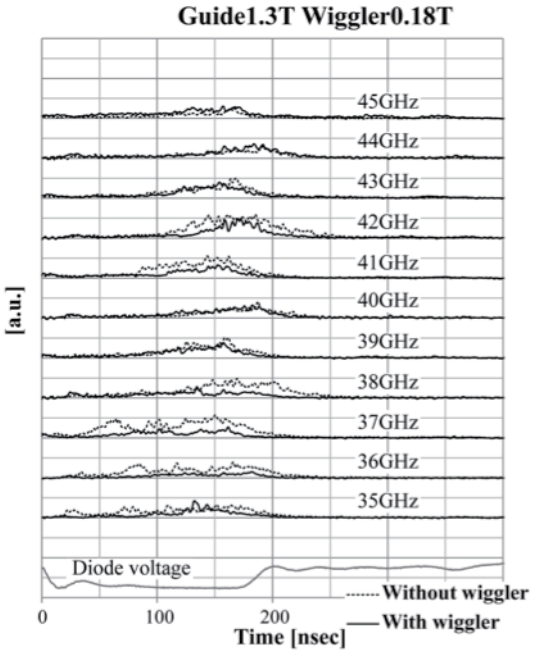

Fig. 6 Diode voltage and microwave waveforms of the diffraction grating. Solid line and dotted line indicate with and without wiggler magnetic field, respectively. No Bragg resonator was used.

difference between with and without the wiggler field as shown in Fig. 7. The experiment of the 45 GHz radiation without wiggler field could not be carried out because of the malfunction of the apparatus. Further investigation became impossible.

The dispersion relation between the beam mode and the Bragg resonator mode is shown in Fig. 8. The simple beam mode in the wiggler magnetic field is written as $\omega = (k + nk_w)v$, where ω, k, v are the angular frequency, the wave number and the velocity along the guide magnetic field of the beam electron respectively, $k_w = 2\pi/L$, and n is an integer. L is the corrugation period. In Fig. 9, the second harmonic of the beam mode and the TE_{31} Bragg reflector mode intersected at near 44 GHz. And the Bragg reflector could work at 44 GHz. Therefore, the interaction between the second harmonic of the beam mode and TE_{31} mode is suspected to cause the 44 GHz radiation.

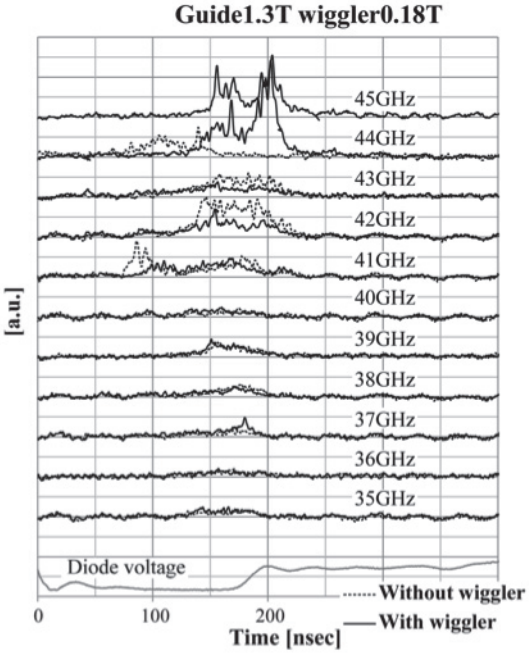

Fig. 7 Diode voltage and microwave waveforms of the diffraction grating. Solid line and dotted line indicate with and without wiggler magnetic field, respectively. A traditional Bragg resonator was used.

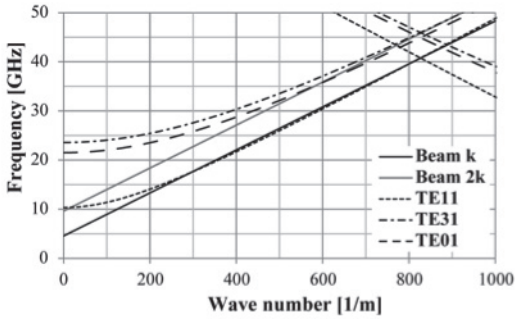

Fig. 8 Dispersion relation.
Fundamental and second harmonic of the beam mode in the wiggler magnetic field are depicted.

4. Conclusions

The radiation with frequency around 40 GHz was observed when the wiggler magnetic field was applied in the experiments with the dispersive line and the filter bank. But in the experiment with the diffraction grating, it could not be reconfirmed. Further experiment could not be carried out because of the malfunction of the apparatus.

After the apparatus is restored, our urgent problems to be solved are below. (1) The wiggler magnetic field was necessary or not for the radiation with frequency around/over 40 GHz. (2) The radiated frequency of around 44 GHz was observed and the designed frequency 40 GHz was not observed yet with the traditional Bragg resonator. After these problems are solved as expected, the experiments with the hybrid Bragg resonator will be carried out.

References

[1] A. Kasugai, K. Sakamoto, K. Takahashi, K. Kajiwara and N. Kobayashi, Nuclear Fusion, Vol. 48, Issue 5, pp. 054009 (2008).

[2] G. G. Denisov, M. G. Reznikov, Radiophysics and Quantum Electronics, vol. 25, No 5, pp. 407-413, (1982).

[3] R. B. Mccowan, Int. J. Electronics, Vol.65, No.3, pp. 463-475, (1988).

[4] I. Boscolo, Appl. Phys. B57, pp. 217-225, (1993)

[5] T. S. Chu, F. V. Hartemann, B. G. Danly, and R. J. Temkin, Phys. Rev. Lett., 72, 2391-2394 (1994)

[6] N. S. Ginzburg, A. M. Malkin, N. Yu. Peskov, A. S. Sergeev, A. K. Kaminsky, S. N. Sedykh, E. A. Perelshtein, A. P. Sergeev, A. V. Elzhov, Phys. Rev. ST-AB, vol. 8, 040705, (2005).

[7] K.Kamada, Y. Soga, S. Odawara, K. Misawa, M. Yoshida, N. S. Ginzburg , Plasma Fusion Res. 8, 2406154 (2013).

MEASUREMENT OF FINE PARTICLES USING X-RAY IN A GAS-PUFF Z-PINCH

T. Miyazaki and K. Takasugi*
College of Science and Technology, Nihon University, Tokyo 101-8308, Japan
** Institute of Quantum Science, Nihon University, Tokyo 101-8308, Japan*

Abstract

The x-ray shadowgraph measurement was used for comb over to spatial distribution of fine particles at the besides maximum pinch time in a gas-puff z-pinch. The experiment of Sn fine particles on change to gas density at the discharge starting time was conducted. The fine particles was not observed on condition of high density gas, so it was considered that the generation quantity of fine particles were extremely little. According to the maximum pinch time, the reduce technique to be generated of Sn electrode material include fine particles were discovered on the experiment condition of the gas density gets higher.

1. Introduction

The debris occurred by large current discharge, and debris makes dirty the focusing mirror on development of discharge produced plasma light source. Specially, Sn electrodes for extreme ultra-violet (EUV) light source generate a lot of debris. In the debris of the gas-puff z-pinch, the debris were scattered preference of radially angle direction from between the electrodes in right of the debris by interacting with plasma.[1] The debris are considered to be made of vapor, droplet and fine particles derived from Sn electrodes, specially, the Sn fineparticles size is about 1 to 100 μm.[1, 2]

The Sn neutral atoms include fine particles radiated characteristic x-ray around the electrode. This x-ray was excited by collision of high energy electrons in a pinch intention.[3] The spatial distributions of characteristic x-ray was cloud like form, and the x-ray form shows distribution of neutral atoms at a maximum pinch time.[3] On the other hand, the mechanism of the generation and scattering process of neutral atoms from electrodes were incompletely understood.

The Sn fine particles of comparatively large size of about 100 μm was focused in this study, the measured spatial distribution and scattering process based on x-ray shadowgraph in agas-puff z-pinch were demonstrated. The x-ray shadowgraph measurement is useful for nondestructive inspection, it was used for examine of fine particles distributionin a plasma. The distribution was measured by change gas density at the discharge starting time in a gas-puff z-pinch, and experiment condition as delay-time and reduce technique of generation quantity of Sn electrode material is discussed.

2. Experiments

Gas-puff z-pinch plasma with generation of fine particles were made by SHOTGUN-1 in the Nihon University. The SHOTGUN-1 is a pulse power device, capacitance and maximum charged voltage were 24 μF and 25 kV and maximum current was about 0.3 MA. The C (graphite) and Sn were used as anode electrode, and aluminum was used as cathode electrode. The distance between anode and cathode electrodes is 30 mm. Helium gas was used as gas-puff. Figure 1 shows set up position of x-ray source, gas-puff electrodes and x-ray detector on the SHOTGUN-1 device.

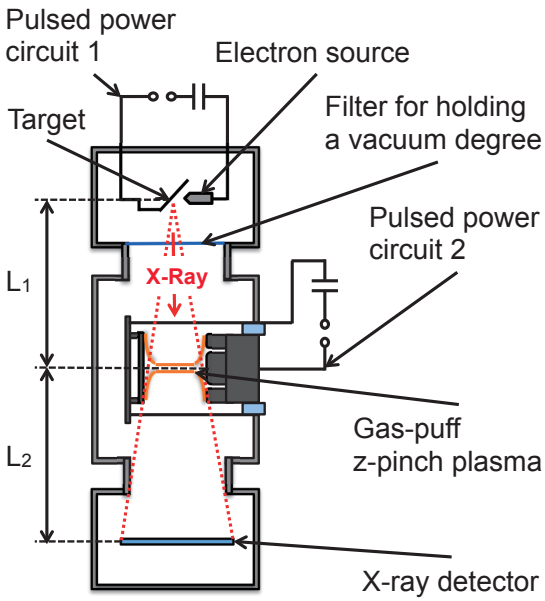

Fig. 1. Schematic of the vacuum chamber, gas-puff z-pinch plasma position, and the x-ray source and detector for x-ray shadowgraph were used in this study.

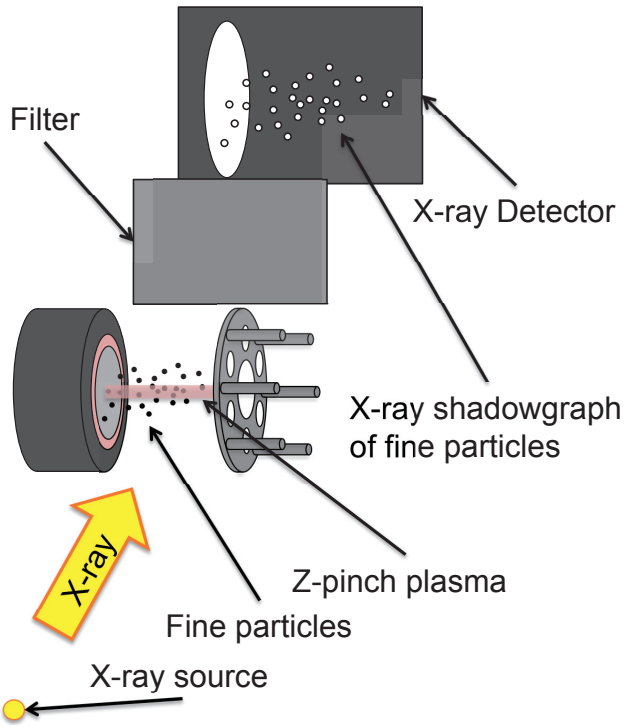

Fig. 2. Schematic illustration of x-ray shadowgraph for fine particles in a z-pinch plasma. The filter absorbs radiation light under about 3 keV from z-pinch plasma.

The between x-ray source and gas-puff electrodes were divided by miler filter of 50 μm in thickness. This miler filter kept a vacuum in x-ray source chamber. The x-ray source based on a vacuum-arc used as x-ray shadowgraph. The specifications of the vacuum-arc x-ray source device used in this study are as follows: brass needle electron source electrode (size of Φ4 × 70 mm) and copper target (size of 0.5 mm thick × 20 mm in width, the electron incident angle of 45 degrees), the distance between the electrodes is 1 mm. This x-ray source was connected to pulse power supply by charged condenser with 20 kV, and the x-ray output were characteristic energy of 18 keV and over a 60 ns FWHM. The x-ray energy of 18 keV was absorbed about 90% by Sn thickness about 100 μm. It was already confirmed that to can take a x-ray shadowgraph by Sn wire thickness 150 μm.[4] This x-rays ource was used to x-ray shadowgraph of Sn particles in this study.

The arrange of x-ray shadowgraph used in this study are as follows: distance between x-ray source and z-pinch plasma L_1 of 470 mm, distance between z-pinch plasma and x-ray detector L_2 of 370 mm. Therefore, the shadowgraph image on x-ray detector was enlarged 1.8 times from effective size. Figure 2 shows schematic illustration of x-ray shadowgraph in a z-pinch plasma. The Tin particles of size about 100 μm in a z-pinch plasma was exposed selectively by x-ray source. A radiant x-ray from z-pinch plasma below the 3 keV was shield by aluminum filter of thickness 15 μm in between a z-pinch plasma and x-ray detector.

X-ray detector were used with Bio-Max MS film detector (made by Kodak company) and intensifying screen (made by FUJIFILM company). The Bio-Max MS film is having sensitivity detector film in EUV or soft x-ray. Consequently, the intensifying screen was used for detect of over 3 keV x-rays. The x-ray film color changes black from translucent when was detected x-ray. Accordingly, x-ray shadowgraph image was observed image of translucent on black film. This x-ray sensitivity of film was showed numerical by photographic density of 0 to 250 in this study. The spatial distribution of Sn fine particles with size of about 100 μm were examined by change gas density at the discharge starting time. The gas density was changed by delay-time of between gas puff timing and discharge start timing. This change of gasdensity means change of characteristic times in plasma pinch, therefore, change of plasma temperature. This plasma temperature control is biga dvantage for discharge produced plasma (DPP) light source by gas-puff z-pinch.[5]

3. Results

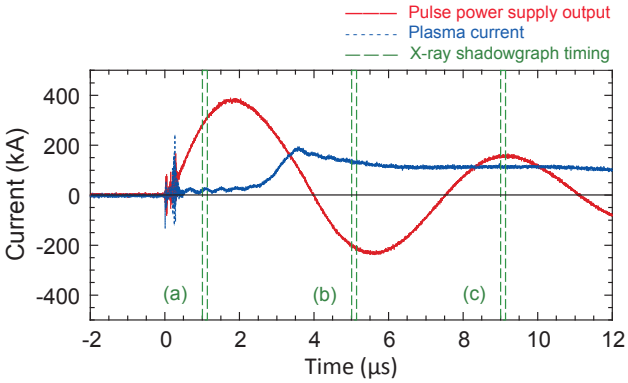

3. 1. Discharge current

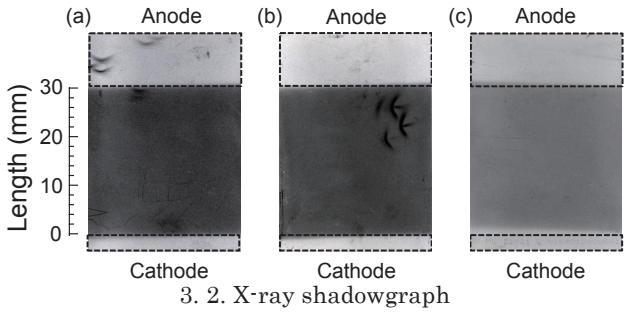

3. 2. X-ray shadowgraph

Fig.3. The gas-puff z-pinch discharge plasma current and pulse power supply current at delay timeof 0.75 ms and x-ray shadowgraph of Sn fine particles atthe three timings of (a) +1 μs, (b) +5 μs, (c) +9 μs.

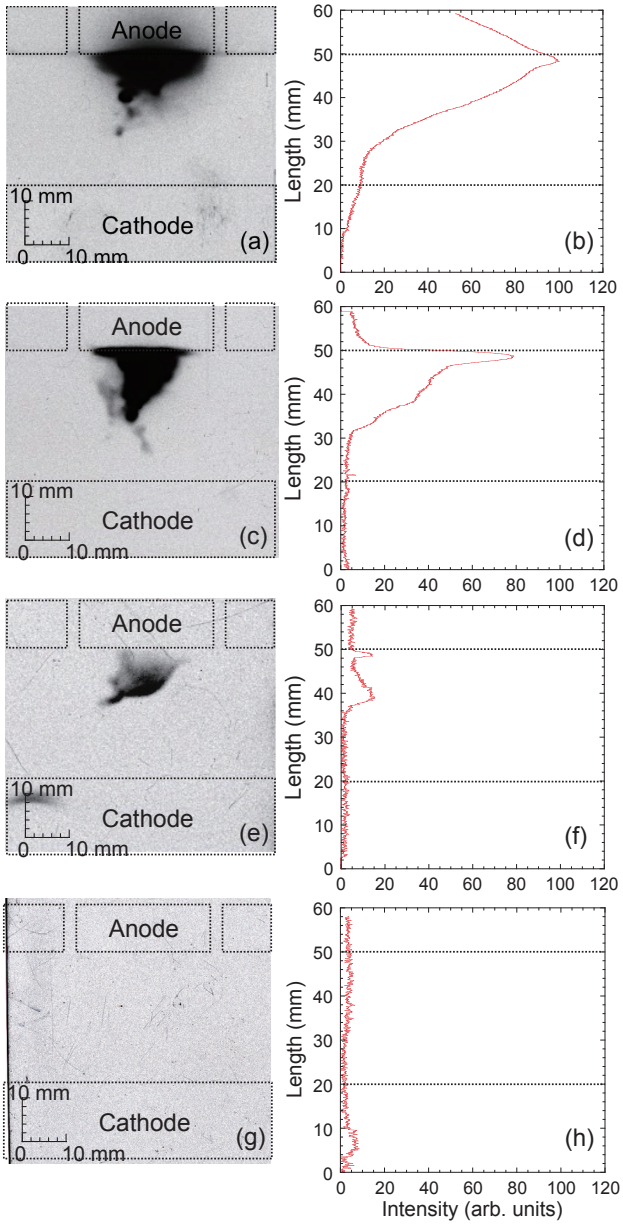

Fig. 4. The spatial distributions of x-ray from Sn neutral atom on between anode and cathode on gas-puff electrodes, and x-ray intensity graph. The x-ray pictures (a), (c), (e) and (g) were examined by x-ray pinhole camera. The (b), (d), (f) and (h) shows the length between gas-puff electrodes vs x-ray intensity.

The spatial distribution between anode and cathode on gas-puff electrodes was examined by x-ray shadowgraph. The x-ray shadowgraph image was measured three different kinds of timing for research of fine particles generate time in discharge.

As a result with the experiment of x-ray shadowgraph, shadow of only gas-puff electrodes was observed on x-ray film, and spatial distribution of Sn particles was not observed in experiment condition as delay-time 0.75 ms. Figure 3 shows discharge current and x-ray shadowgraph at three different kinds of timing. The red line and blue line show on pulse power supply current and pinch plasma discharge current, and the green frame shows exposure timing by x-ray shadowgraph in Fig. 3. 1. The three photographs (a), (b), (c) in Fig. 3. 2 shows spatial distribution of Tin particles in three different kinds of exposure time on Fig. 3. 1, (a) , (b), (c).

However, x-ray pinhole camera was used for comb over to spatial distribution of fine particles at the maximum pinch time. As shown in Fig. 4, the spatial distributions image of x-ray from inner core excitation in Sn neutral atoms, and shows scatter range of Sn electrode material at the maximum pinch time. Figure 4 (a), (c), (e) and (g), were measured by x-ray pinhole camera, and the experiment condition as delay-time of 0.25, 0.35, 0.45, 0.75 ms to (a), (c), (e) and (g). Figure 4 (b), (d), (f) and (h), shows normalized x-ray intensity of (a), (c), (e) and (g) on between anode and cathode. The larger of an area of x-ray spatial distributions image, the more the scatter range of Sn electrode material was wide in Fig. 4. As a result with the experiment of x-ray pinhole camera, the generation area of Sn electrode material at the maximum pinch time was reduced as the delay-time gets longer.

4. Discussion

The reason why Sn fine particles with size of about 100 μm were not observed in delay-time 0.75 ms is discussed here.

One of the reasons was generation quantity of Sn electrode material include fine particles itself were maybe little in an experiment condition as delay-time 0.75 ms. To change a delay-time gets longer means to make a low temperature plasma in gas-puff z-pinch. Therefore, the scatter of Sn electrode material was not almost occur in low temperature of pinch plasma, and the contact temperature on Sn electrode of plasma maybe was less than temperature of Sn boiling point as 2.88×10^3 K and melting point as 5.05×10^2 K. Actually, the generation area of Sn at the maximum pinch time was reduced as the plasma temperature gets lowerin Fig. 4.

In addition, as another reason was generation quantity of fine particles were maybe extremely little, and of fine particles spatial distribution are concealed irregular development of x-ray film. In this case, measurement of fine particles were extremely difficult. Because, if a lot of measurement shot for integration exposure was conducted, the fine particles spatial distribution to be covered black back-ground of x-ray film by substitute exposure. In either case, x-ray shadowgraph measurement was needed to more confirm another delay-time in a gas-puff z-pinch.

5. Conclusion

The x-ray shadowgraph measurement was used for comb over to spatial distribution of fine particles at the besides maximum pinch time in a gas-puff z-pinch.

As per the results of this study, the Tin fine particles were not observed in an experiment condition as delay-time 0.75 ms by x-ray shadowgraph in Fig. 3. According to the maximum pinch time, the generation quantity of Sn electrode material include fine particles was reduced as the delay-time gets longer by x-ray pinhole camera image in Fig. 4.

Therefore, the spatial distribution of fine particles at the besides maximum pinch time was not revealed at this stage, and x-ray shadowgraph measurement needs more a lot of time at other delay-time.

On the other hand, it was revealed in this study that it was considered that the generation of electrode material include fine particles were extremely little on experiment condition of high density gas, and, the generation of electrode material at the maximum pinch time were reducedonthe experiment condition of the gas density gets higher.

This reduce technique of fine particles leads to development of the debris less extreme ultraviolet plasma sources based on a gas-puff z-pinch.

References

[1] Maeda, M. Nishio and K. Takasugi, NIFS-PROC., Vol. 87, 26. (2010).

[2] K. Takasugi, and A. Maeda, J. Plasma Fusion Rws., SERIES, Vol. 8, (2009).

[3] K. Takasugi, S. Narisawa and H. Akiyama, AIP Conf Proc.,Vol. 651, 131. (2002).

[4] T. Miyazaki, M. Nishio and K. Takasugi, NIFS-PROC., Vol. 93, 33. (2013).

[5] K. Takasugi, H. Suzuki, K. Moriyama and T. Miyamoto, Jpn. J. Appl. Phys. Vol. 35, 4051. (1996).

Inverse Analysis of Warm Dense Matter based on Sudden-freeze Approximation

Akihito Tezuka, Mitsuo Nakajima, Tohru Kawamura,
Jun Hasegawa, and Kazuhiko Horioka

Department of Energy Sciences, Tokyo Institute of Technology,
4259 Nagatsuta-cho, Midori-ku, Yokohama 226-8502, Japan

ABSTRACT

Thin wires were rapidly vaporized in a capillary by means of a pulsed power discharge. The vapor evolved to a plasma state through a warm dense matter region, in which the equation-of-state and transport coefficients are unclarified. The warm dense plasma expanded freely into a vacuum chamber. We proposed a method to analyze the flow based on sudden-freezing approximation which enables us to estimate the ionization degree of the dense plasma at warm dense state.

Keywords

Warm dense matter, Sudden freeze model, Ionization relaxation, High energy density science

1. Introduction

Every matter in an equilibrium state can be placed in a regime of a density-temperature diagram[1,2]. In the diagram, warm dense matter (WDM) is defined as a strongly coupled plasma having a temperature of 10^3 to 10^5 K and a number density of 10^{20} to 10^{24} cm^{-3}. When we increase the energy density of a solid, it changes to a plasma inevitably through WDM states. Thus, when we study the evolution of matter over a wide parameter space, it is important to know the physical properties of the WDM. Recently, the importance of the study on the WDM has been recognized, particularly in studies on interiors of giant planets such as Jupiter and the hydrodynamics of fuel pellet of inertial confinement fusion.

However, in the WDM regime, there has been established no appropriate equation of state (EOS) in spite of a large amount of experimental and theoretical efforts in this field[3,4,5]. This is due primary to difficulties in accurately measuring the state variables. In laboratory experiments it is impossible to confine the warm dense plasma for a long time because the WDM state is inevitably accompanied with a high pressure of the order of GPa.

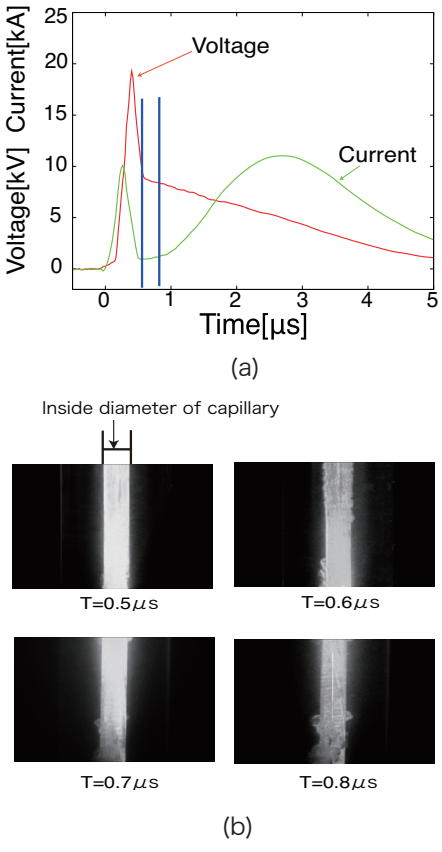

Fig. 1 Voltage and current waveforms (a) and framing images of exploding wire / plasma evolution in Pyrex-capillary (b) [2].

As a result, experimental data in this parameter region have not yet been obtained so much.

In our laboratory, several experimental attempts have been performed on the WDM study. In the previous studies using wire explosion in water, we obtained an electrical conductivities under well-defined input energies evaluated from current-voltage properties as well as plasma densities evaluated from plasma radii[2]. Typical current and voltage waveforms and the time evolution of a plasma produced by a wire discharge in a semi-rigid grass capillary are shown in Fig. 1. Those results showed that well-defined states of warm dense matter can be produced with this experimental configuration.

In this paper, we propose a new scheme for the evaluation of ionization degree of WDM based on a semi-experimental approach.

2. Experimental Setup

Fig. 2 shows a schematic illustration of the experimental apparatus, with which a WDM is produced by the capillary-confined wire explosion technique based on pulsed power discharge. A discharge current of several tens of kiloamperes is driven by coaxially connected low-inductance capacitors which are switched by a pressurized spark gap. An aluminum wire mounted in a Pyrex glass capillary is rapidly heated by the discharge current during sub-microsecond time scales. The diameter of the wire (typically 50-100 μm) is chosen so that the skin effect can be negligible. Therefore the input energy is expected to be uniformly distributed in the wire. The voltage across the both ends of the wire and the current following through the wire are measured with a high voltage probe and a Rogowski coil, respectively. Assuming a uniform plasma, we evaluate the input energy and resistivity of the WDM.

In our new scheme, the upper electrode has a small hole (throat) of 0.5 mm in diameter, from which the wire plasma expands freely into vacuum. A Faraday cup is placed ~10 cm downstream from the capillary, which obtains a current signal of the charged particle flow ejected from the capillary.

3. Proposed Scheme and Discussion

3.1 Scheme of measurement

There were discussions for a long time on the intermediate state of freely expanding flow in vacuum, in which the transition from continuum-like collisional flow to collisionless expansion takes place[6,7]. When such a transition of flow occurs gradually, it is difficult to estimate the flow property. However, by applying a 'Sudden freeze' model[8], we can avoid this difficulty. The sudden freeze model assumes that, when the number density of freely expanding atoms/molecules in vacuum decreases rapidly, the transition from collisional flow to collisionless expansion happens abruptly in a infinitely thin layer, in which the physical parameters are frozen without any transition region. The sudden freeze model was used to study a chemically non-equilibrium transitional flow in a wind tunnel[8]. The model was extended to estimate the surface temperature of a laser irradiated target from the ablation plasma flux[9].

Let us consider the applicability of this model to the analysis of the charged particle flow ejected from a WDM. In our experimental configuration, the flow state is characterized by a relationship between the

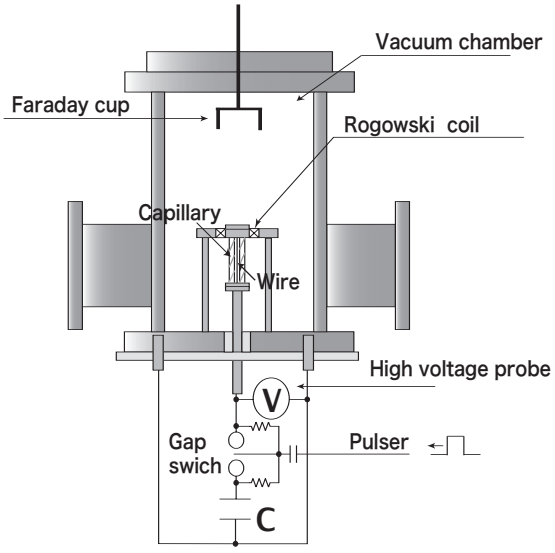

Fig. 2 Schematic diagram of experimental set up.

throat diameter and the mean free path of particles. The mean free path estimated from the number density of atoms/ions is typically ~10^{-8} m at the throat in our experimental condition. On the other hand, the throat diameter is ~10^{-4} m. Hence, the system behaves as a fluid at the throat. The Knudsen number K_n (*i.e.* a dimensionless number defined by a mean free path λ devided by a characteristic length L) is the criterion of the transition from collisional flow to collisionless expansion. We know empirically that when $0.1 < K_n < 10$, the transition takes place. That is, when $K_n > 10$, physical quantities are expected to 'freeze' at a constant values. In other words, when the number density of atoms/molecules in the flow decreases by the expansion from WDM down to less than 10^{16} cm^{-3}, the ionization degree is considered to be frozen at this moment and remains constant in the succeeding expansion process. Therefore, when we consider an ionization relaxation equal to the transition of the molecular flow, the number density at the freezing point can be expressed as follows

$$n \sim n_0 \times 10^{-5},$$

where n_0 is the number density (~10^{21} cm^{-3}).

We can regard the expansion starts from a point source. Then, the time evolution of the plume number density can be written by

$$n(t) \propto n_0 \tilde{r}^{-3}, \qquad (1)$$

where $\tilde{r}$ is the distance normalized by the throat diameter. Hence the distance between the freezing point r_f and the throat is estimated to be ~0.01 m. In contrast, the Faraday cup is placed ~0.1 m downstream from the throat. Based on these considerations, the ionization degree should be frozen before the flow reaches the Faraday cup.

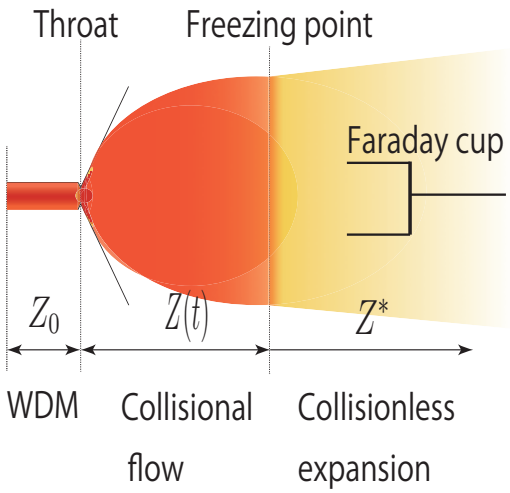

Fig. 3 Schematic diagram of a free-expanding and sudden-freezing flow.

3.2 Method of inverse analysis

Figure 3 shows a schematic diagram of the free expanding flow. The WDM generated by the wire explosion blows out into vacuum as a collisional flow. The collisional flow changes to a collisionless flow, at a freezing point. Downstream from the freezing point, there is a few change of physical quantity.

The first problem is to make clear the relationship between the flux profile and the ionization degree at the freezing point. The charge flux $I(t)$ measured by the Faraday cup is written by

$$I(t) = eZ^* n'(t) v'(t), \qquad (2)$$

where e is the elementary charge, Z^* is the degree of ionization at the freezing point, n' is the number density, and v' is the particle velocity at the Faraday cup.

An analytical expression for the number density of a freely expanding flow is given by

$$n \propto n_0 \left(1 - \tilde{x}/\tilde{t}\right)^{3+j}, \qquad (3)$$

where $\tilde{x}$ is the distance from the throat normalized by the characteristic length of the system, $\tilde{t}$ is the normalized time and j is the internal degrees of freedom[7]. In turn, if we consider that the hydrodynamic acceleration in the vacuum chamber is such ineffective, we can consider that v' is

approximately equal to the speed of sound at the throat ~ 10^4 m/s. Hence, if we determine *n'* and *v'*, we can obtain *Z** from the following equation,

$$Z^* = \frac{I(t)}{en'(t)v'(t)}. \qquad (4)$$

The second problem is to make clear the relationship between *Z** and the ionization degree of the WDM Z_0. For finding the answer to this problem, we measure the charge flux as a function of the throat diameter because, as discussed in the previous section, the location of freezing point changes depending on the throat diameter. Then, we can expect to obtain different current signals at the Faraday cup.

Finally we can expect the following relation for the ionization degrees at two different freezing points 1 and 2,

$$Z_2^* - Z_1^* = \frac{I_2(t) - I_1(t)}{en'(t)v'(t)}, \qquad (5)$$

where subscript 1 and 2 denote flow variables obtained with different throat diameters. The rate of change of the ionization degree is given by

$$\frac{\Delta Z}{\Delta t} \equiv \frac{Z_2^* - Z_1^*}{t_{\mathrm{f}2} - t_{\mathrm{f}1}}, \qquad (6)$$

where t_f means the interval of the freezing time. By performing the parametric measurements, we obtain the approximate differential coefficient of the evolution of the ionization degree in the collisional state *Z* with the following equation,

$$\frac{dZ}{dt} \sim \frac{1}{\Delta t}\left(\frac{I_2(t) - I_1(t)}{en'(t)v'(t)}\right), \qquad (7)$$

and we can derive the ionization degree of the WDM Z_0 inversely from the Faraday cup signals. Namely, the ionization degree Z_0 is able to be estimated by,

$$Z_0 = Z^* - \frac{dZ}{dt}t_\mathrm{f}, \qquad (8)$$

where t_f is a fitting parameter of this scheme.

The freezing point may depend on the ionization degree of the flow, which affects the hydrodynamic acceleration limit in the collisional regime. If these effects are within an allowable level, we can estimate the degree of ionization of WDM using well-established diagnostics based on the discussion mentioned above.

4. Conclusions

We proposed an evaluation of ionization degree method for the warm dense matter. The WDM is made by wire explosion and expanded rapidly into a vacuum chamber though a small throat. The free-expanding flow is characterized using a 'sudden freeze' approximation for the ionization degree, which enables us to make a parametric analysis of the free expanding flow. We discussed the criterion of the frozen flow and the procedure for the flow analysis.

References

[1] Kazuhiko Horioka, "High-Energy-Density Science with Pulse-Power Energy Drivers", *JPSJ*, 67, pp.252-257 (2012).

[2] Hiroki Sakai, Kotaro Iwasaki, Mitsuo Nakajima, Tohru Kawamura, Kazuhiko Horioka, "Electrical Conductivity Measurements of Warm Dense Matter with Semi-rigid Vessel", *NIFS-Proceedings*, 90, pp.36-39 (2012).

[3] SESAME: The Los Alamos National Laboratory Equation of State Database, Report No. LA-UR-92-3407, edited by S. P. Lyon and J. Johnson, Group T-1

[4] P. Renaudin, C. Blancard, G. Faussurier, P. Noiret, "Combined Pressure and Electrical-Resistivity Measurements of Warm Dense Matter Aluminum and Titanium Plasmas", *Phys. Rev. Lett.* 88, 215001 (2002).

[5] Alan W. DeSilva, H.-J. Kunze, "Experimental Study of the Electrical Conductivity of Strongly Coupled Copper Plasmas", *phys. Rev. E*, 49, 4448 (1994).

[6] G. A. Bird, "*Molecular Gas Dynamics and the Direct Simulation of Gas Flows*", Clarendon Press Oxford, p.189 (1994).
[7] K. P. Stanyukovich, "*Unsteady Motion of Continuous Media*", Elsevier, pp.498-506 (1960).
[8] K. N. C. Brey, "Atomic recombination in a hypersonic wind-tunnel nozzle", *Journal of Fluid Mechanics*, 6, pp1-32 (1959).
[9] Alexey A. Morozov, Anton B. Evtushenko, Alexander V. Bulgakov, "An analytical continuum-based model of time-of-flight distributions for pulsed laser ablation", *Appl Phys A*, 110, pp691-696 (2013).

Measurement of energy distribution in a pulse-compressed pure electron plasma

Y. Park, Y. Soga, Y. Mihara, T. Uesaka, T. Kikuchi*

Graduate School of Natural Science and Technology, Kanazawa University

**Mechanical Engineering, Nagaoka University of Technology*

ABSTRACT

Experimental study on dynamics during the pulse compression of a charged particle beam by a pure electron plasma confined in a cylindrical Malmberg-Penning trap has been started. Because non-neutral plasmas in the trap are physically almost equivalent to beams seen from the rest frame of reference, we can observe beam emittance by measurements of the axial temperature and radial density profile on the plasma. An axially extended electron plasma is compressed in the axial direction by applying negative voltage to ring electrodes placed at a region in which the plasma exist. Preliminary experiment shows that application of negative bias to five electrodes successively from one end is more suitable for beam compression than simultaneous application to the electrodes.

Keywords

Non-neutral plasma, Space-charge-dominated beams

1. Introduction

In the heavy ion fusion devices, longitudinal pulse compression section is constructed in front of the implosion section on any type of accelerator systems [1]. Since the effective implosion of a target is disturbed by an increase in emittance of compressed ion beam, a clear understanding is necessary about transient phenomena of space charge dominated beam during the pulse compression. But the production of an intense heavy ion beam requires a large particle accelerator, so ion beam is not suitable for the experimental study.

A pure electron plasma has been expected to use for the investigation of the fundamental properties of space charge dominated beam. The purpose of this study is to investigate dynamics during the pulse compression of a charged particle beam by using a pure electron plasma. This idea is based on the simple fact that beams seen form the rest frame are physically almost equivalent to a pure electron plasma in confinement cylindrical trap [2].

In this paper, we examine energy distribution of the electron plasma after compression by two different methods of compression.

2. Experimental method

The schematic configuration of the compression experiment device is shown in Fig. 1. The device is composed of an electron source and a cylindrical vacuum vessel, ring electrodes 60 mm in a diameter, magnetic field coils, a phosphor screen and CCD camera. The basic scheme of the electron confinement consists of the homogeneous magnetic field B = 0.1 T along the z-axis and the saddle shaped axisymmetric potential with negative barriers at both ends.

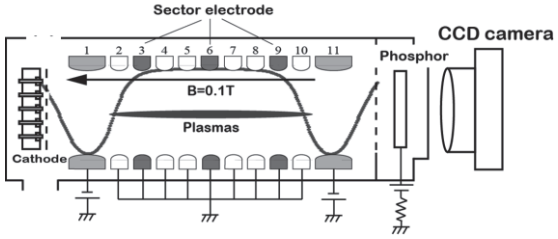

Fig. 1: Schematic configuration of electron trap.

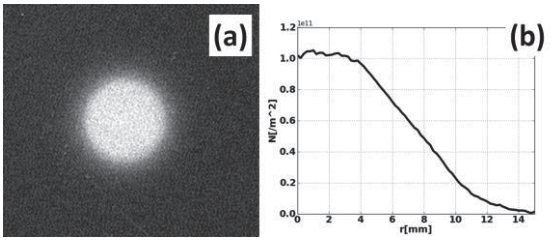

Fig. 2: (a) CCD image describing the density profile of the pure electron plasma in the initial state. (b) Radial distribution of the density profile in the initial state.

Electrons are provided from an array of small electron emitters placed in the weaker field zone through the left barrier, while the confining potential at the plug cylinder is raised to ground in a variable short time. Electrons are disconnected from the sources on the recovery of the potential barrier. After arbitrary time, the barrier potential is grounded, and electrons exit the trap region along the magnetic field. The measurements of the density profile are made by dumping the whole electrons through the end cylinder on the other side of the cathodes onto a phosphor screen that is biased up to 5 kV from the machine ground. The luminosity distribution on the screen is detected with a CCD camera with 512 times 512 pixels and recorded on a computer for numerical analyses. A linear relationship has been confirmed between the total electron number and the luminosity integrated over the screen.

We use an electron plasma, cylindrical in shape with an equilibrium state, as the initial profile for the experiment as shown in Fig. 2. This distribution is produced by mixing and relaxation of about 500 strings of electrons which accumulate in the trap through multiple injection-hold-mixing cycles.

A longitudinal kinetic energy distribution of plasmas is measured by the energy selection method using variable potential at end electrodes. The electrons are dumped by a lowered, but non-zero, confinement potential. Electrons with sufficient energy can escape from the potential barrier. By repeating the procedure with various barrier potentials, we measured a number of electrons Q_{esc} as a function of the energy E (Eq.(1)).

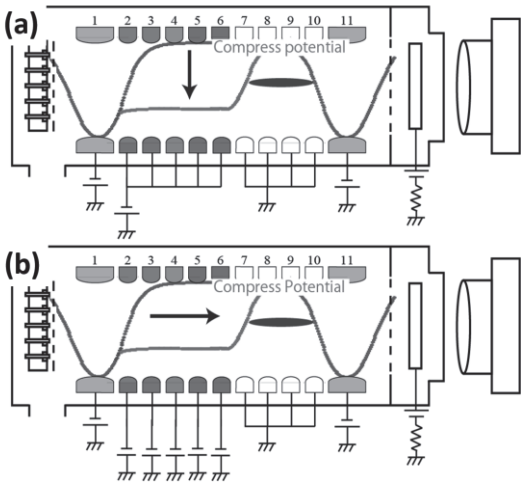

Fig. 3: Electrons are compressed by changing trap potential with simultaneous (a) and successive (b) application of negative voltage to ring electrodes.

By differentiating the data, we obtained the longitudinal energy distribution of the electrons

$$\boldsymbol{Q_{esc}(E) = Q_{all}\int_E^{\infty} dE\,\frac{F(E)}{\sqrt{E}}} \qquad \cdots(1)$$

$$\boldsymbol{F(E) = -\sqrt{E}\,\frac{d}{dE}\,\frac{Q_{esc}(E)}{Q_{all}}} \qquad \cdots(2)$$

Here Q_{all} is the total number of electrons.

Methods of plasma compression are schematically shown in Fig. 3. The axial compression is achieved by applying negative voltage to five ring electrodes placed at a region in which the plasma exists. We adopt two compression method: applying a voltage to all electrodes at the same time (method 1 shown in Fig. 3(a)) or applying a voltage to electrodes successively from left end (method 2 shown in Fig. 3(b)).

3. Result

A space potential created by the ring electrode after the compression is shown in Fig. 4. The initial potential is produced by applying -100 V to both end electrodes (solid line). The compression potential is produced by applying -60 V to the electrodes (dotted line). The compression potential is almost the same in the both compression methods, because the region in which the plasma exists is same. The trap region is changed from 120 mm to 30 mm during the compression.

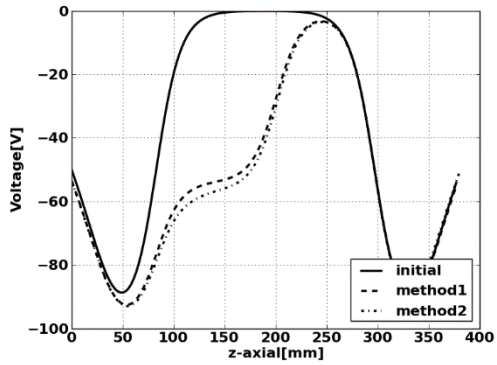

Fig. 4: Space potential distribution on the z-axis created by the ring electrodes. Solid line shows an initial potential, and dot lien shows a compression potential.

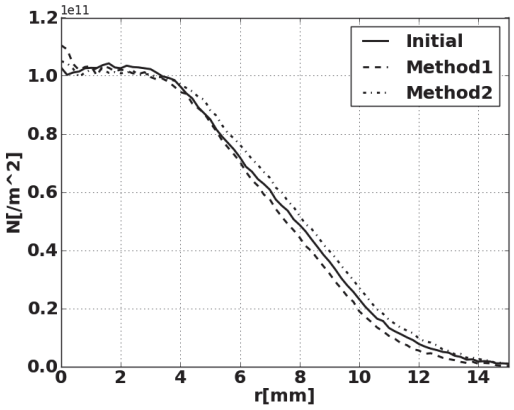

Fig. 5: Radial distribution of the density profile. Lines labeled with Methods 1, 2 are profiles after compression by each method.

Figure 5 shows density profile in the initial state and after the compression. Since the vertical axis indicates the area density of electrons, the increase of volume density due to an axial compression is not represented in the figure, i.e. it shows 2D distribution of the electron plasma. The density distribution after compression in both methods doesn't change from the initial distribution.

Longitudinal kinetic energy distributions before and after compression are shown in Fig. 6. Average longitudinal kinetic energy is 1.06 eV in the initial state. After compression the energy increases at 2.68 eV in the method 1 and at 2.62 eV in the method 2.

4. Discussion and Conclusion

The 2D distribution of density profile doesn't change while the volume density increases about 4 times due to the compression. Theoretical and simulation work indicate that an increase of a flat top area in the density profile occurs during the compression when a space charge effect on beams dominates [3]. To study a space charge effect on electron beam, it is pointed out that a plasma with the density at a half of Brillouin limit density has to be prepared [2]. The Brillouin limit is expressed as

$$n_{lim} = \epsilon_0 m\Omega_c^2/2q^2 = \epsilon_0 B^2/2m.$$

In this experiment, $n_{lim} = 4.8 \times 10^{16}[m^{-3}]$. On the other hand, maximum plasma density we produced in the experiment is $n_{max} = 3.3 \times 10^{12}\ [m^{-3}]$. The condition of space charge effect during the compression is not achieved because the space charge

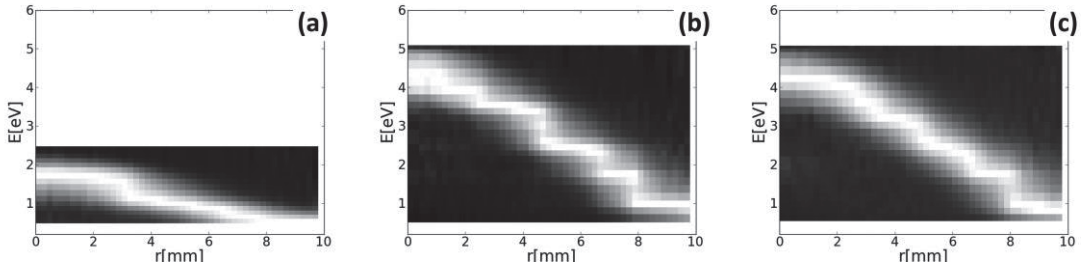

Fig. 6: Longitudinal kinetic energy distribution at initial state (a) and after compression by method I (b) and method II (c). The luminosity increases with number of particles normalized by maximum value of each radius.

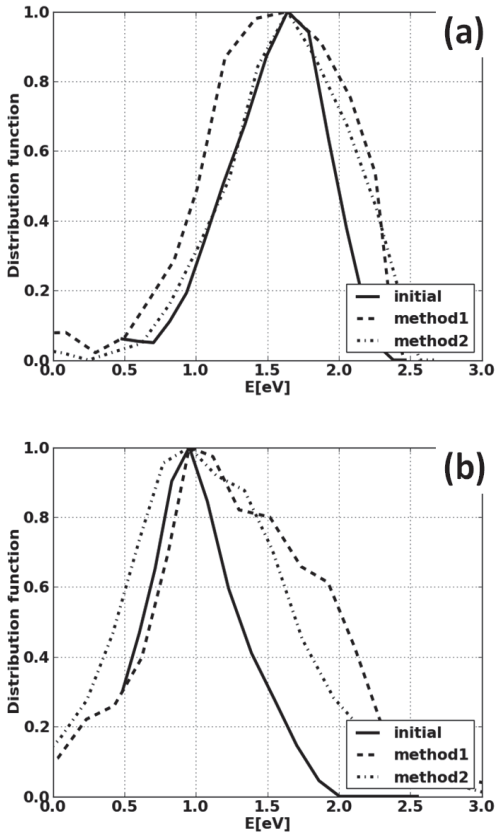

Fig. 7: Energy distribution at initial state and after compression on axis (a) and at r = 5 mm (b). Abscissa of the profiles after compression is shifted to coincide with a peak energy at the initial state.

effect is 4 orders of magnitude smaller than the estimation from Brillouin density limit. We should prepare more dense plasma in a future work.

Figure 7 shows axial energy distributions at initial state and right after the compression. The temperature of the electron plasma is determined from a spread of the energy distribution. The full width at half maximum of the energy distribution on the axis is estimated at 0.75 eV in the initial state, 1.07 eV after compression by method 1, and 0.86 eV by method 2 shown in Fig, 7(a). The suppression of the increase in a temperature during compression by method 2 suggests that the method 2 is more suitable way for a beam compression to produce low emittance beam. On the other hand at r = 5 mm the increase of the temperature after the compression is almost the same in both methods. However the increase of temperature in the periphery of density profiles could be attributed to a gradient of the density in which the azimuthal velocity shear exists.

In conclusion we examined energy distribution of the electron plasma after a compression by two different methods of compression. Preliminary experiment shows that application of negative bias to five electrodes successively from one end is more suitable for beam compression than simultaneous application to the electrodes in order to produce low emittance beam.

6. References

[1] JJ Barnard et al, Nucl. Instrum. Methods Phys. Res. A415 (1998) 218-228

[2] H. Okamoto, H. Tanaka, Physics, Res. A437 (1999) 178-187 (1999).

[3] R.C.Davidson, 2001.12, "Physics of Nonneutral Plasmas", Singapore, World Scientific Publishing Company

Precise Control of Stacked Induction Modulator

Yasuo Sakai, Mitsuo Nakajima, Jun Hasegawa, Takashi Kikuchi*and Kazuhiko Horioka

Department of Energy Sciences, Tokyo Institute of Technology,
4259 Nagatsuta, Midori-ku, Yokohama 226-8502, Japan

**Department of Nuclear System Safety Engineering, Nagaoka University of Technology,*
1603-1 Kamitomioka, Niigata 940-2188, Japan

ABSTRACT

Controllability of the induction voltage adder of our beam simulator was improved by using solid-state voltage drivers. Through the improvement, we could upgrade the reproducibility and the longitudinal controllability of particle beams. Preliminary beam compression experiment indicated that we can expect to advance the study on beam physics during the longitudinal beam modulation, based on the upgraded induction adder.

Keywords

Induction accelerator, Pulse power, Particle beam, Beam physics

1. Introduction

For application to beam driven high-energy-density sciences such as heavy ion fusion, high power particle beams up to TW levels are required [1, 2]. To create such an extremely high power beam which is not produced by conventional accelerators, longitudinal compression is one of the most essential technics [3]. Principle of the longitudinal compression is schematically shown in Fig. 1, in which an axially velocity-modulated beam is spatially and temporally focused by time-of-flight (see Fig. 1). On this manipulation, beam compression ratios, pulse durations, and the resulting beam powers are, basically, sensitive to the initial longitudinal beam temperature (longitudinal velocity spread) and accuracy of the applied longitudinal focusing force. In addition, the space-charge effect is considered to dominate the beam behavior in the high current beam compression process. Especially, through beam collective motions and/or instabilities induced by strong and dynamic self-electric field, redistribution of beam kinetic energy into longitudinal and/or transverse thermal energies, that is, energy dissipation, may occur. The energy dissipation induces emittance growth substantially and disturbs the beam compression.

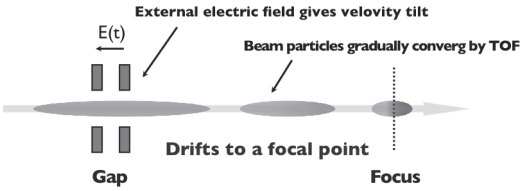

Fig. 1 Schematic diagram for longitudinal compression of charged particle beams.

To investigate the compression dynamics without or with the dissipation process, we proposed and constructed a scaled experiment with compact and flexible device based on electron beams (e-beams) and an induction voltage adder. Up to now, we upgraded the simulator device, and have succeeded in pulse compression to nano seconds order in a low perveance regime [4]. However, along with the experimental progress, it becomes clear that improvements of controllability and reproducibility of the modulation voltage are inevitable to certainly evaluate the phenomena.

In this paper, firstly, we introduce the concept of our beam compression experiment and recent

Table. 1 Typical beam parameters for HIB and e-beam. Here we assumed beam bunches with pulse duration of 100 ns and the geometrical factor of 5.7. V_{ex}, I_b, and K_L indicates the beam extracting voltage, current, longitudinal perveance respectively.

Beam species	q/m [C/kg]	V_{ex} [V]	I_b [A]	β	K_L [mm]
Pb	4.67×10^5	$1\text{-}10 \times 10^9$	$0.1\text{-}10 \times 10^3$	0.1-0.3	0.038-38
Electron	1.75×10^{11}	$2.7\text{-}27 \times 10^3$	$0.3\text{-}30 \times 10^{-3}$	0.1-0.3	0.038-38

progress. Then, our an approach to improve controllability and reproducibility of induction adder by using solid-state voltage drivers will be described. Finally, a preliminary beam compression experiment with upgraded simulator device will be shown.

2. Compact Beam Device for Scaled Experiments

2.1 Scaled-down experiments based on electron beams

Practically, high current heavy ion beams (HIBs) such as Pb and U with current of kA levels and particle energy of a several GeV are applied for experiments on high-energy-density sciences. To provide these high current HIBs, it's essential to take various beam manipulations such as multi-beam transport and beam combining [3]. As a result, the accelerator systems inevitably become huge and complex. However, when we focus on pure beam physics, full-scale experiments are not necessarily required. If beam parameters were properly scaled and controlled, an evaluation of similar physics can be realized by using compact simulator device based on e-beams.

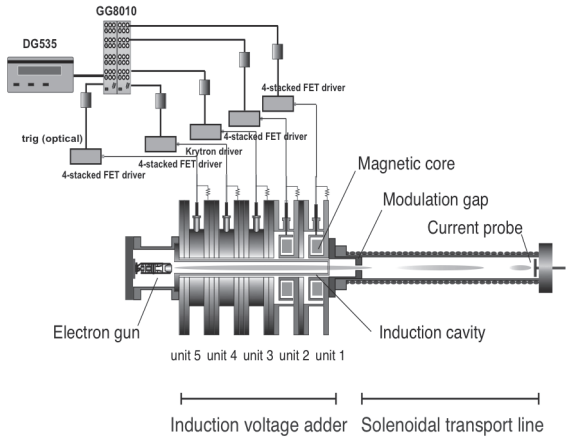

Fig. 2 Schematic diagram for compact beam device with induction voltage adder.

Table 1 shows typical beam parameters and required accelerating voltage for HIB and e-beams. As shown in Tab.1, we can provide similar beam dynamics to HIBs by using e-beam; equivalent β value and longitudinal perveance K_L can be available with several kV-mA e-beams.

2.2 Experimental apparatus and method for longitudinal compression

Figure 2 shows a schematic diagram for the compression experiment. The device consists of a thermionic-cathode electron gun, an induction voltage adder, a solenoidal transport line and a current probe. In the experiment, first, a continuous e-beam with 2.8 keV energy is injected into the induction cavity. Next, a time varying voltage, here we define a modulation voltage, is generated at the modulation gap by the induction voltage adder. Then, a portion of the injected beam is applied a velocity gradient from beam head to tail. After that, this velocity modulated beam is transported downstream into the solenoidal transport line. In this stage, the beam bunch is gradually focused. Finally, the beam bunch is compressed at geometrical focus L_f and measured by the Faraday cup with a 1 GHz bandwidth oscilloscope, Tektronix- TDS684B.

The modulation voltage has approximately pulse duration of 100 ns and -2.5 kV peak voltage, and the solenoidal transport line produces longitudinal magnetic field of several tenth of mT. With this configuration, the beam is confined in transvers direction, and is quasi-one-dimensionally focused in the longitudinal direction.

Table 2 Relevant parameters for longitudinal beam dynamics in this experiment.

I_0 [mA]	g	$\varepsilon_{zz'0}$	K_L [mm]	$K_L Z_m/\varepsilon^2_{zz'0}$	$(K_L Z_m/\varepsilon^2_{zz'0})$
0.1-1	5.7	2.4×10^{-2}	0.11-1.1	0.49-4.9	9.8-98

2.3 Beam parameters

The longitudinal beam envelope equation [5] provides a general description for the longitudinal behavior of the beam, and can be adopted for a simplified scaling parameters on the compression dynamics [6]. For this study, the beam was extracted from the 2.8 keV thermionic- cathode electron gun with currents from 100 μA to 1 mA. Supposing the beam could be quasi-one dimensionally compressed to 20 times of initial and the beam longitudinal temperature, T_L, was equivalent to the cathode temperature, the relevant major beam parameters are estimated as listed in Table 2. We can find from Tab. 2, the compressed beam in our simulator device cover a wide parameter space from emittance dominated to space-charge dominated; $K_L Z_m / \varepsilon_{zz0'} >> 1$ regions, where $\varepsilon_{zz0'}$ is the initial emittance [6, 4].

2.4 Experimental results and a technical problem of voltage controllability

Figure 3 shows typical output voltage of the induction adder and compressed beam current waveforms [4]. In this experiment, a portion of continuously extracted electron beam with average initial beam current I_0 = 84 μA was applied a modulation voltage shown in Fig. 3(a) as "synthesis" waveform. The longitudinal magnetic field of the solenoidal transport line was 13 mT. As shown in Fig. 3(b), we can confirm the longitudinally velocity modulated beam was pulse compressed from 100 ns to 3.2 ns with full width at half maximum (FWHM).

As mentioned in Sec. 1, there are two principal factors for beam dynamics and the resultant beam pulse shapes during longitudinal compression; beam space-charge effects including the energy dissipation due to interactions between beam particles, and the shape of modulation voltage waveform to induce a velocity modulation (longitudinal focusing force).

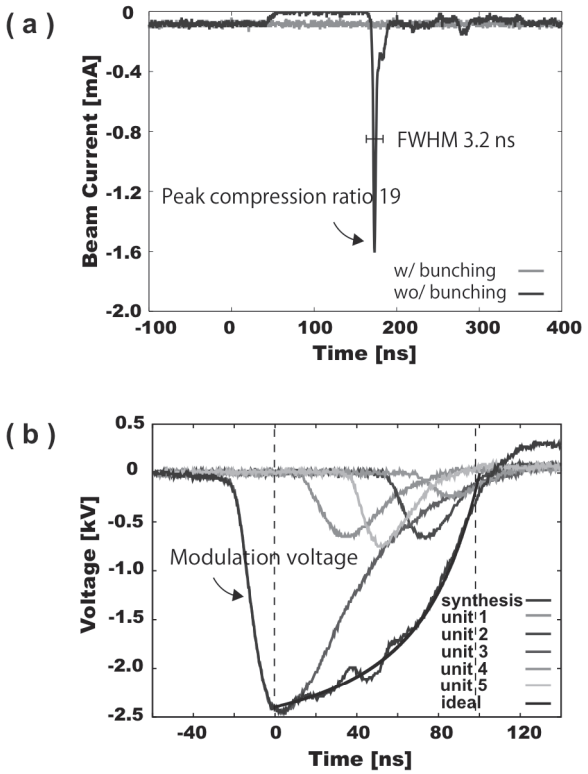

Fig. 3 Typical waveforms of compressed beam current (a) and modulation voltage (b).

This means, it's essential to ensure high reproducibility and accuracy of the modulation voltage for precise investigation of the beam dynamics, and improvement of controllability of induction adder became desirable for better experimental condition.

In the following section, a brief explanation of operating principle of stacked-induction-voltage adder and detailed designing of power drivers aimed to improve controllability will be described.

3. Induction Voltage Adder

3.1 Principle of basic induction accelerators and induction voltage adder

Induction modulator is a device which accelerates or decelerates charged particles by induction voltage induced by a pulse current around its ferromagnet. The operation principal is well explained by 1:1 transformer model [7].

A great characteristic of the induction modulator is that superposing and forming of arbitrary voltage

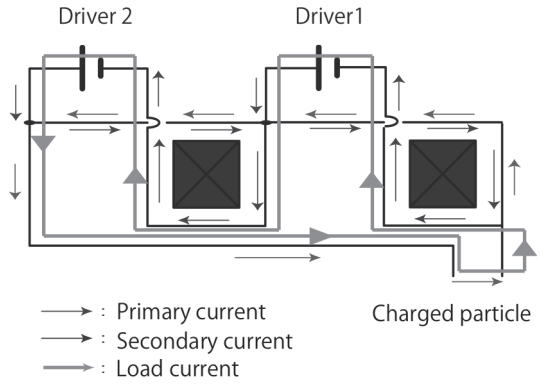

Fig. 4 Equivalent circuit of induction adder.

waveforms are possible by connecting multiple units in series. For understanding on the operation principle of stacked induction modulator (induction adder), here we assumed two units stacked case, and consider its operation principle by using an equivalent circuit shown in Fig. 4. When pulsed voltages are applied to each unit, leak currents are induced around each magnetic core (outer conductive wall of each unit). However, since these leak currents cannot flow into high voltage side of power supplies (the drivers) and the modulation gap, these currents flow as "primary current" indicated in Fig. 4. On the other hand, counter electro motive forces are generated around magnetism cores. However, these flows also cannot take a current path across the cores. Then, the net current path (in Fig. 4, indicated as "Load current") is closed through charged particles flow at the modulation gap. As a result, superposition of the inputted pulsed voltages is generated and applied to the beam at the modulation gap.

Considering operating principle mentioned above, we can find that the synthesized voltage waveforms depends on voltage waveforms and triggering delays of each drivers. This means, improvement of reproducibility and reduction of jitters of each driving power source are quit important for better controllability of voltage forming.

3.2 Configuration of induction voltage adder in beam simulator device

The compact beam device has an induction voltage adder composed of five units as shown in Fig.2. Each unit includes magnetic core in its stainless steel cavity. The magnetic cores are made by wound and overlapped 15-20 μm Finemet thin film with SiO_2 insulation, and has a whole size of 155 mm outer 60 mm and inner diameters with a thickness of 26 mm. Each unit is driven by an independent pulse power supply, and each driver is triggered by digital delay pulse generator, Stanford Research System- DG535, and delay pulser, EG&G ORTECH-GG8010, as schematically shown in Fig. 2. With this configuration, we can generate arbitrarily pulse voltage waveforms by controlling output voltages and trigger timings of the drivers.

In this research, previously, we have been adopted 4-stacked MOSFET pulser as power drivers for four units, and for one unit, we used a krytron switching pulser as shown in Fig. 2. In the following section, details of these two drivers are described. After that, we introduce a new type driver aimed to improve the wave forming controllability.

3.3 Configuration of induction drivers and design of low jitter driver

(1) 4-stacked MOSFET driver

Figure 5 (a) shows a circuit diagram of the 4-stacked MOSFET driver. To form an ideal modulation voltage for beam compression experiment, basically, it's desirable to generate semi sinusoidal voltage of pulse duration of several tenth of nanosecond with peak voltage of around 1kV. Considering an inductance of the induction unit, we designed this driver with simple RC discharge circuit with power MOSFETs, DE475-102N20A, which has high speed switching ability. Rated drain-source withstand voltage of DE475-102N20A is 1 kV. On the other hand, to produce up to 1 kV terminal voltage through the modulator unit, increase of charging voltage is unavoidable to overcome voltage drops in both driver-circuit and induction unit. So, this driver was designed as four stages switched configuration. Each MOSFET is simultaneously switched-on by incoming TTL signals through optical fibers for isolation.

(2) Krytron driver

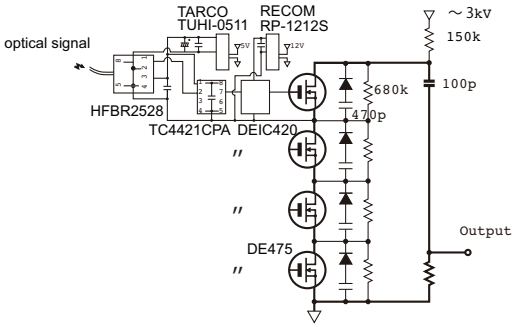

(a) 4-stacked MOSFET driver

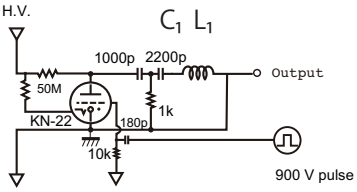

(b) Krytron driver

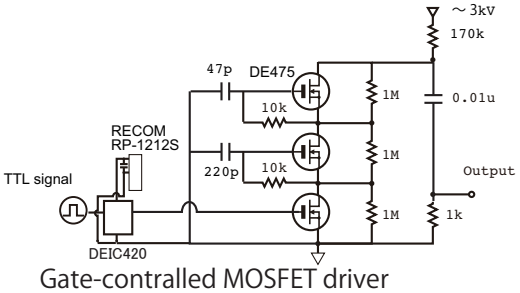

(c) Gate-contralled MOSFET driver

Fig. 5 Circuit diagrams for induction drivers.

Typical output voltage of the induction unit of the FET driver was about 1 kV at maximum. However, to form the ideal modulation voltage, another power supply was needed which can produce higher peak voltage and long pulse width. Increasing the number of FET stages provides better characteristics to withstand the higher voltage, but it increases the jitter of operation. Then, we constructed another driver with a krytron, KN-22, as a switching device. KN-22 has a characteristics of high withstand voltage and relatively fast switching. The circuit diagram is shown in Fig. 5 (b). This driver includes a waveform-forming circuit (in Fig.5 (b), indicated as "C_1, L_1"). With this configuration, we are able to change discharge rising and/or falling property over a wide range of parameters.

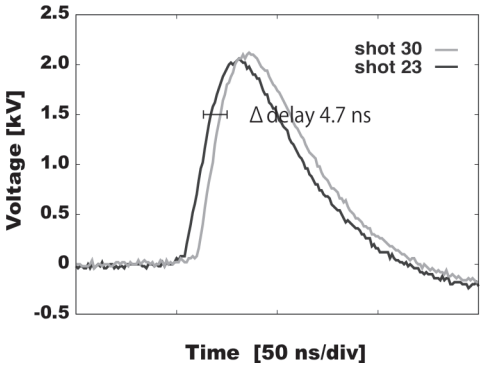

Fig. 6 Typical output voltage of a modulator unit with krytron driver.

On the beam experiment, we have been driving the induction adder by the use of these two types of drivers, and the beam device have been improved to a level which can compress the beam bunch up to a few nano seconds as presented in Sec. 2.4. However, along with this improvement, degradation of the reproducibility of the pulsed current waveform became often to be confirmed. Cause investigations indicated that the main cause was jitter of the krytron driver. Typical voltages waveforms of krytron pulser are shown in Fig. 6, from which we can confirm approximately 5 ns time difference. As we presented in Sec. 3.1, the jitter of each unit driver directly influences the reproducibility of output waveform. On the other hand, krytron driver unit can generate pulsed voltage with peak voltage of 2.5 kV and time duration of 100 ns, and covers the major part of the modulation voltage as shown by "unit 3 output" in Fig.3 (b). Therefore, these fluctuations of trigger timing induce non-negligible effects not only on the rise time but also on the pulse global shape.

(3) Designing of low jitter driver

To fulfill the low jitter requirements to improve reproducibility of the modulation voltage, a prototype driver was developed. Figure 3(c) shows the circuit diagram. As shown in Fig. 3 (c) the driver is designed as a pulse supply with sequentially self-triggered MOSFETs.

This prototype driver is designed as gate controlled type pulse power supply. When the first stage MOSFET is triggerd by TTL signal through the gate driver DEIC420, higher stages are sequentially

self-triggered due to voltage droops between the gate and the source terminals. With this configuration, output jitter can be suppressed since the output delay is only dominated by the rise time of the gate driver. Square-wave pulses with minimum width of 30 ns and maximum 3 kV can be available with this module. When we include the droop of induction unit, minimum time duration of 40 ns and maximum 2.5 kV square like output voltage could be available.

3.4 Operation tests and results

Jitter characteristic is evaluated for the three different types of drivers. On the operation test, we evaluated the jitter by a measured difference of delay from the averaged value over 30 shots, where we defined the delay as a rise time to a constant voltage from the trigger time (see Fig.7 (a)). Figure 7 (b) is typical

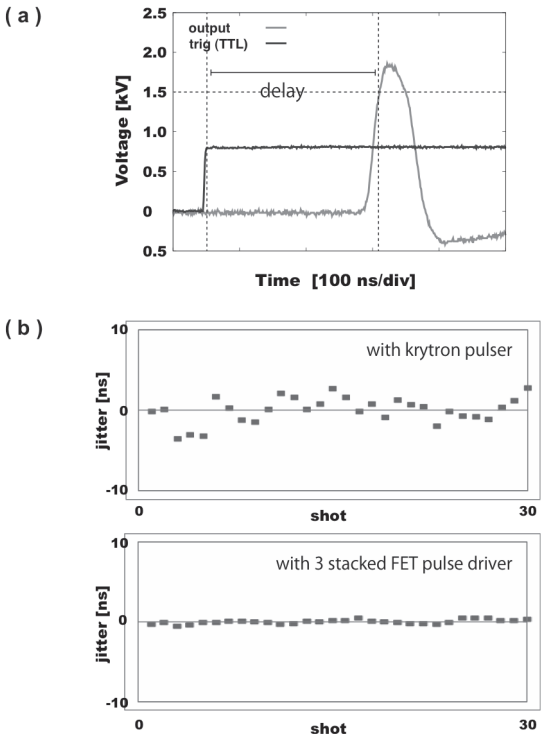

Fig. 7 Typical results of jitter evaluation test.

Tab. 3 Jitter characteristics.

Driver type	Maximum jitter [ns]	STDEV [ns]
4-MOSFET	1.8	0.3
Krytron	6.3	1.6
Gate controlled MOSFET	1.0	0.3

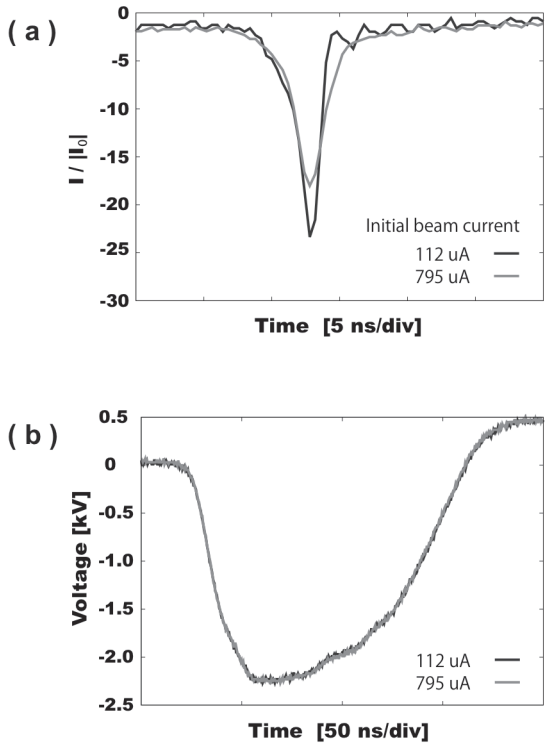

Fig. 8 Typical waveforms of compressed beam current and modulation voltage.

results of the measured jitter through 30 shot measurements, and resultant maximum jitters and standard deviations (STDEV) for each device are summarized in table 3. As shown in Tab. 3, the STDEV jitter was evaluated to be 0.3 ns for the prototype device, and we could suppress the value by 82 percent compared to the krytron driver. In addition, we observed the maximum jitter can be suppressed 1.0 ns through the consecutive 30 shots operation test. From the results of this operation test, we concluded the device has enough ability for the beam experiment.

4. Preliminary experiment on beam compression experiment

A beam compression experiment was conducted with a upgraded simulator device. In the experiment, the induction adder was re-constructed by three 4-MOSFET drivers and two gate-controlled MOSFET drivers. Longitudinal magnetic field was fixed 13 mT. Typical experimental results are shown in Fig. 8. Here, in Fig. 8(a), the compressed beam

current is normalized by the initial current.

As shown in Fig. 8 (a), the peak compression ratio was decreased from 23.6 for I_0 = 112 μA to 18.1 for I_0 = 795 μA. In addition, FWHM was also increased from 1.9 to 2.7 ns. On the other hand, the fluctuation of the modulation voltage was suppressed to low enough and the reproducibility of the modulation voltage is greatly improved that dose not affect the discussion of the space-charge effect on the beam compression experiments. Indeed, we can confirm that the scatters of its waveforms are suppressed less than the line width in Fig. 8 (b). To summarize theses results, we can conclude the changes in beam current waveforms are due to beam self-electric field.

5. Conclusion

Controllability and reproducibility of the induction adder were improved by using solid states drivers to upgrade the compact simulator device for beam longitudinal compression study. We constructed a gate-controlled-3-staged MOSFET diver with sequential self-triggered configuration. The driver could generate approximately square-wave pulse voltage with pulse duration of 30 ns at minimum and 3 kV maximum voltage. Also, the we show that driver jitter is less than 0.3 ns in standard deviation which is enough level for the beam experiment at 100 μA level. In addition, the beam compression experiment was also conducted with the up-graded simulator device based on the MOSFET drivers. In the experiment, we confirmed the normalized pulsed beam current waveforms clearly depends on initial beam current. The result means the increased beam self-electric field affects the beam dynamics during the compression process. The result also indicates that a strong self-fields induce the energy dissipation of beam kinetic energy, and strongly disturbs the longitudinal compression. We can expect to advance the scaled experiments on the beam physics during the longitudinal compression based on the simulator device with upgraded induction voltage adder.

References

[1] K. Horioka et.al. Nucl. Instr. Meth, A-606 (2009) 1-5

[2] P.A.Seidel et.al.Nucl. Instr. Meth. A-606 (2009) 75-82

[3] Bangerter. R. O., Fusion Eng. Des. 44 (1998) 71

[4] Y. Sakai et.al., Nucl. Instr. Meth. Phys. Res. A-733 (2014) 70-74

[5] M. Reiser, “Theory and Design of Charged Particle Beams”, John Wiley and Sons. INC (1994)

[6] T. Kikuchi et.al., EPJ Web of Conference 59 , 099004 (2013)

[7] S. Humphries. Jr., “Principle of Charged Particle Acceleration”, Wiley Interscience Publication (1986)